The Dissertation Committee for Clayton John Dahlman Certifies that this is the approved version of the following dissertation:

Interaction Between Structural and Electronic Phase Changes of Metal Oxide Semiconductor Nanocrystals

Committee:

Delia Milliron, Supervisor

Brian Korgel

C. Buddie Mullins

C. Grant Willson

Graeme Henkelman

Interaction Between Structural and Electronic Phase Changes of Metal Oxide Semiconductor Nanocrystals

by

Clayton John Dahlman

Dissertation

Presented to the Faculty of the Graduate School of

The University of Texas at Austin

in Partial Fulfillment

of the Requirements

for the Degree of

Doctor of Philosophy

The University of Texas at Austin

August 2017

Acknowledgements

I would like to thank my advisor Delia for her guidance and support during my Ph.D. You have placed a great deal of faith in me, including some crazy ideas that may not have always warranted such enthusiasm, and I appreciate the space you created to foster my growth as a scientist. Thank you for the supportive mentorship, and for always helping me keep the big picture in context.

Most of my successes in lab, and beyond, over the past five years can be attributed in some part to my close friends and colleagues in the Milliron group. Evan, Rob and Gary – your support during some tumultuous times truly kept my head up and eyes forward, and I can't thank you enough. Amy and Ben – your friendship has been a valuable addition to my life and I am grateful that you joined the migration to Texas three years ago. The Milliron group has been welcoming, warm and inspiring throughout my PhD, and I want to thank Ankit, Corey, Camila, Sungyeon, Shin, Lauren, Stephen, Manny, Sandeep, Omid, Memo, Sebastien, Anna, Raffa, Natacha, Evie, April, Jessy, Renjia, Yizheng, Gabriel, Yang, Jongwook, Ajay, Amita, Byung Hyo, Anthony, Elise, Susanne, Franziska, Ilka and Beth for contributing an invaluable, positive impact to my life and scientific career. I also want to thank Jacob, Daniel and Allison for dedicating your time during busy undergraduate careers to drive some remarkable scientific progress. I extend my thanks to Prof. Brian Korgel, Prof. Grant Willson, Prof. Buddie Mullins and Prof. Graeme Henkelman, for serving on my dissertation committee and engaging in my scientific progress. To the rest of my friends and collegues in Austin, thank you for the warm welcome. To my friends and colleagues in Berkeley, including Jeff Reimer and the rest of the Reimer group, my friends and classmates in CBE and colleagues at the Molecular

Foundry, thank you for the exciting and friendly community during the early years of my PhD, and I look forward to our continued friendship in the years to come. I would like to acknowledge the help I received from the students and scientists at the Advanced Light Source, particularly Matt Marcus at BL10.3.2 and Jinghua Guo and his group at BL8.0.1, for their expert assistance and helpful discussions during my work. I also want to thank Mike Toney and his group at SSRL for assistance with X-ray diffraction, and Brett Helms and his group at the Foundry for their help with some tricky experiments.

Mom, Dad, Todd, Wendy, Paige and Luc – you have put up with years of my griping about grad school, confusing lectures on odd science fascinations and inconsistent visits. I couldn't have done any of it without your love and support, so thank you for everything.

Finally, to Ellen and Donnie – thank you for keeping me balanced through all of this.

Abstract

Interaction Between Structural and Electronic Phase Changes of Metal Oxide Semiconductor Nanocrystals

Clayton John Dahlman, Ph.D.

The University of Texas at Austin, 2017

Supervisor: Delia Milliron

Semiconducting metal oxides have emerged as a core class of materials in functional electronic devices because of their versatile compositions and tunable electronic and optical properties. Applying a charge to metal oxides can modulate carrier properties and induce structural changes from charge-compensating defects. However, charge-mediated transformations are contingent upon efficient transport of carriers, compensating species, or field biases into the bulk. Nanostructured materials, including colloidal metal oxide nanocrystals, can accommodate efficient charge transport across the semiconductor interface, and exhibit sensitive optical and electronic properties that arise from their nanoscale geometry. This dissertation studies the relationship between charge-mediated electronic and structural phase changes in metal oxide nanocrystals, and correlates these transformations with their nanoscale geometry and interfacial environment. The first investigation studies anatase TiO_2 nanocrystals during electrochemical charging. TiO_2 nanocrystal films can undergo two independent charging processes within a Li-ion electrolyte: surface capacitance, which raises the Fermi level upon reduction and induces

Drude-like infrared localized surface plasmon resonance without affecting structure, and intercalative charging caused by the insertion of Li^+ into the nanocrystal lattice. These two charging processes create independent dual-spectrum visible (Li-ion intercalation) and infrared (plasmon resonance) optical responses to applied bias, with applications for versatile electrochromic smart windows. The optical and electrochemical properties of both charging mechanisms are isolated and studied independently to examine the role of structure and interfacial environments on these transformations. The second part of this dissertation explores charge-mediated transformations in nanocrystalline VO_2, which has a highly non-ideal, charge-correlated electronic structure. A charge-mediated electrochemical insulator to metal transformation in VO_2 is found to be highly sensitive to nanoscale grain size, leading to a secondary metal-insulator transformation for sufficiently confined particles. The results of these studies establish general principles to control the interplay between defect-mediated structural transformations, ideal semiconductor gating behavior and interfacial environments in metal oxide nanocrystals.

Table of Contents

List of Tables

List of Figures

Chapter 1: Introduction

MOTIVATION

The electronic control of material properties has been the driving force behind many of the technological and societal growth of the past century. Ever since the discoveries of early 17th century scientists about the nature of electronic charge, humanity has been fascinated by the role electrical charge can play in manipulating objects and processes around them. By the early 19th century, scientists following Faraday's pioneering work began noticing that some materials responded in a peculiar manner to electrical currents and potentials, with changes in resistance, color and other properties[1]. Coined as semiconductors, this class of materials with variable electronic properties has been provided the backbone of the modern digital world. To this day, the pursuit of materials that change properties upon charging is an essential avenue of research for scientists, promising new applications in dynamic transistors, memory devices, sensors, coatings, batteries, catalysts and more.

However, this line of investigation is limited by the inherent barriers that impede the transfer of an electronic impetus (as current or potential) into the bulk of a semiconductor. No matter what exotic, innovative functionalities one can imagine for an electronic device, one must find a way to deliver an electronic input to the material for it to function. Furthermore, even for materials that have sufficient conductivity to transport charge through the bulk, or support deep field penetration depths, the behavior of these materials at the interface can be quite distinct from the bulk. To this end, the electronics industry of the modern era relies on the development of interfacial structures, and microstructured material geometries, to maximize this transfer of electronic charge and potential into functional materials. One off-shoot of this effort has been the development

of colloidal semiconductor nanocrystals – tiny, nanometer-sized crystallites of semiconductor materials that can be dispersed in solution or processed into nanoscale solid features. At sizes approaching 10 nm and less, the properties of these materials can be almost entirely dictated by the behavior of their interfaces. For instance, in a 10 nm spherical nanocrystal, nearly 10% of the nanocrystal volume lies within 3Å of the particle surface, which is roughly the distance between neighboring octahedral metal atoms in a semiconductor like anatase TiO_2[2]. The distinct interfacial behaviors of nanocrystal semiconductors can be processed into functional bulk devices by forming coatings or mesostructures from ensembles of nanocrystals. These films can retain many of the bulk properties of the inherent semiconductor moieties, but with dramatically higher internal interfacial density to facilitate charge transport and field modulation and unique changes in behavior from the nanoscale geometry.

Constraining the dimensions of a semiconductor can generate material properties that diverge from the bulk, or even new properties that wouldn't exist in a larger geometry. For instance, the confinement of excitons and free carriers to particle sizes approaching the carrier's Bohr radius can induce a localization energy that changes the optical absorption and photoluminescence of colloidal particles such as CdS, CdSe, ZnO, in a size-dependent manner[3]. Optical and electronic conductivity can also show unique properties at the nanoscale, leading to size-dependent attenuation of light near the Drude resonant plasmon frequency[4], or metal-insulator transitions in composites of conducting inclusions as composite morphology is varied[5]. The interface between a semiconductor nanocrystal and host medium (solvent or composite matrix) defines boundary conditions for charged carrier transport and field propagation, which can approach the discrete length scales of a variety of properties that separate bulk and molecular behaviors.

The novel functionalities of nanoscale semiconductor materials have spurred the development of functional materials that use these unique properties. However, the same interfacial constraints that alter the properties of these materials can also have a drastic effect on their synthesis and structural stability. The interfacial surface energy can change the total free energy of a semiconductor particle and alter the equilibrium between different crystal phases as a function of particle size, as is the case in TiO_2 nanocrystals[6]. The surface energy in crystalline solids is typically unique for each exposed crystal facet on the particle, leading to a diverse array of particle sizes and shapes as processing conditions alter the balance of kinetic particle formation rates and structural stability[7]. The interfacial region in crystalline solids can also accommodate significant lattice strain near the under-coordinated surface atoms, allowing for size-dependent variations in lattice dimensions and transport properties, even for a consistent lattice structure[8]. Integrating nanoscale semiconductor crystals into functional electronic devices must also account for the effects of electronic charging, applied fields and ion intercalation on structural and electronic stability of as-synthesized materials. The fundamental question posed in this dissertation is thus – what is the interaction between confined, interfacial structure and charging-mediated transformations in semiconductor nanomaterials? The pursuit of this goal has led to discoveries and new electronic and optical functionalities directly related to the structural confinement and interfacial effects in these materials.

COLLOIDAL SEMICONDUCTOR NANOCRYSTALS

One avenue to create semiconductor materials with high interfacial density is to grow colloidal nanocrystals from precursor reagents in solution. Colloidal nanocrystals – single grain microscopic solid particulates dispersed in solution – have the unique

capability to combine the solid-state properties of bulk semiconductors with the solution processibility of dissolved molecules. The dispersibility of nanocrystalline semiconductors have allowed them to be applied in biomedical applications as fluorescent labels[9], inks for spray-coated photovoltaic[10] and electrochromic film coatings[11]. Colloidal nanocrystals also demonstrate unique electronic and optical properties, due to the geometric constraints of charge, strain and polarization as discussed previously. Colloidal nanocrystals are free from the geometric limitations of lithographically defined nanostructures, so diverse 3-dimensional sizes, shapes and composite structures can be synthesized to exploit these unique properties of nanoscale materials[7,12].

The synthesis of colloidal nanocrystals relies on balancing the energetic costs of forming materials with high interfacial density with the rapid kinetics of nucleation and growth of small particulates. At equilibrium, the growth of colloidal nanocrystals from a solution of precursor molecules can be described by changes in an arbitrary particle's surface and bulk free energy. A particle with a given surface area (A) and volume (V) will have a formation energy defined by:

$$\Delta G = A\gamma + V\Delta G_v$$

Here, γ is the surface energy per area and ΔG_v is the change in free energy between dissolved solution precursor molecules and these same species in a bulk crystal, per volume.

For a spherical particle, $A = 4\pi r^2$ and $V = \frac{4}{3}\pi r^3$, yielding an equilibrium that shows two regimes of stability for a nanocrystal of size r: vanishingly small, and infinitely large (**Figure 1.1a**). ΔG_v can further be defined by the supersaturation of reagents (S) and molar volume (V_m) of the bulk crystal: $\Delta G_v = -RT \ln S / V_m$. If the supersaturation is increased to a critical value, S_c , the total free energy of the nucleation barrier (ΔG_c) can be overcome by thermal kinetic energy and particles will nucleate in solution. Any particles

that grow beyond the critical radius, r_c, can continue to grow at any degree of supersaturation (**Figure 1.1b**). These kinetics produce the classic LaMer plot of colloidal growth shown in **(Figure 1.1c)**[13]. Initially, the supersaturation must be increased to reach the critical nucleation threshold by adding reagents (Regime A). Once this critical supersaturation is achieved, particles will nucleate and grow, consuming reagents until the supersaturation drops below S_c again (Regime B). Once the supersaturation is below the critical value, nucleation will cease and the existing nuclei will continue to grow until a stable solution is reached at S=1 (Regime C)[14].

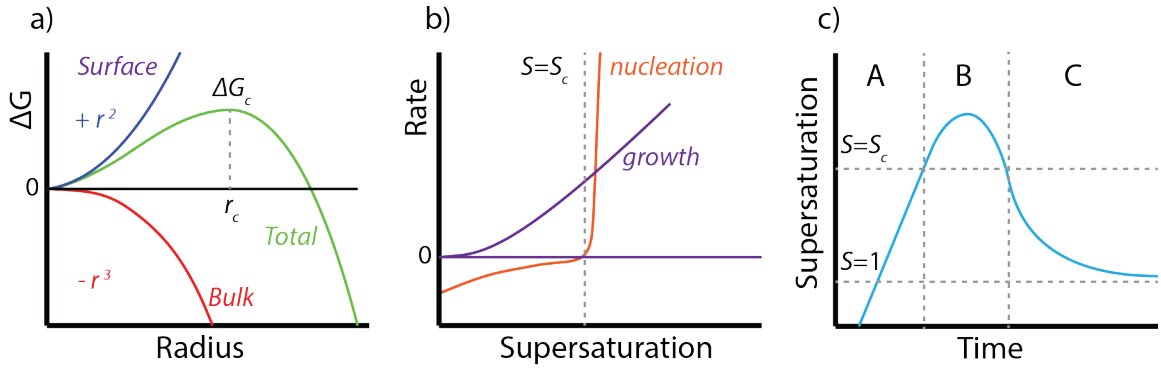

Figure 1.1: LaMer model of nucleation and growth.

a) Radial dependence of surface and bulk free energies in a spherical particle, showing the critical radius of particle stability. b) Kinetic diagram of the rate of nucleation and growth as a function of supersaturation of reagents in a solution. c) LaMer plot of the time dependence of supersaturation in a colloidal nucleation and growth mechanism.

The size and number concentration of colloidal nanocrystals during a synthesis reaction can theoretically be controlled by precisely tuning the concentration (supersaturation) of precursor reagent in the reaction solution over time. Practically

speaking, one would also tune the energetics of this reaction by changing the surface energy contribution with different molecular surface-binding ligand species, by changing the temperature of the reaction to adjust kinetic rates, and by tuning the energetics of the reagents with different precursor molecules and environmental conditions.

TiO_2: a versatile metal oxide semiconductor

Titanium dioxide (TiO_2) is a versatile semiconductor that is notable for its diverse technological applications, ranging from uses in common products such as white paint pigments and UV-blocking particles in sunscreen, to energy conversion as a photovoltaic charge transport and photocatalytic water splitting material, and including environmental and biological applications such as biosensing, water purification and catalytic pollutant degradation. The wide bandgap and band-like charge transport of free electrons in TiO_2, coupled with its responsive surface chemistry and flexibility as a synthetic product and framework, have inspired a rich body of literature[15]. TiO_2 has been particularly successful as a scaffold or light-sensitizing material for electronic devices that transport charge from optical excitons for photovoltaic and photocatalytic devices. Several polymorphs of TiO_2 have a bandgap in the UV, efficient charge transfer kinetics and tunable surface chemistry that can be interfaced with other electronic and optical materials[16,17]. The material is also well-known as an insertion electrode for small-ion (Li^+, Na^+) battery applications because of its durable structure with open interstitial voids that can accommodate cation insertion with minimal strain[18]. These properties make TiO_2 a rich platform to study the effects of nanoscale interfacial confinement on charge mediated electronic and structural tranisitions.

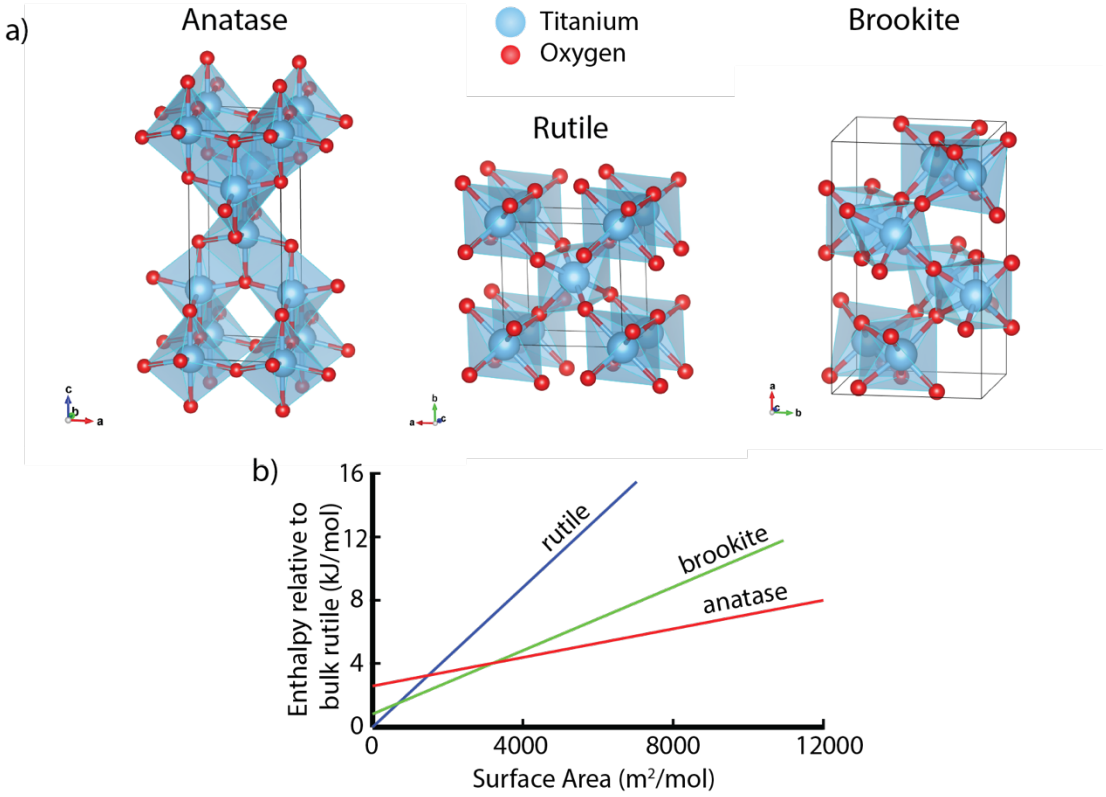

Figure 1.2: Unit cells and surface energies of anatase, rutile and brookite TiO_2

a) Unit cells of the three most common TiO_2 polymorphs, anatase (ICSD 9852), rutile (ICSD 62677) and brookite (ICSD 36408). b) Formation enthalpy relative to bulk rutile as a function or molar surface area, adapted from Ranade *et al* [6].

Stoichiometric TiO_2 has been synthesized and studied in several crystal phases, and as an amorphous glass[19], each with its own optical, structural and electronic properties. All polymorphs are composed of Ti-O_6 octahedra arranged in various configurations. At the thermodynamic limit, bulk TiO_2 is stable in the rutile structure. However, surface energies can change the stability of different phases at a nanoscale size regime. Brookite and anatase have lower surface energies than rutile and become stable at small sizes (**Figure 1.2**) [6,19,20]. The kinetics of nucleation and facet growth rates also play an important role in determining

the final crystal structure in bottom-up synthesis techniques. Wet chemical methods to synthesize colloidal TiO_2 nanocrystals afford precise control on facet-directed growth to give well-controlled dispersions of different sizes, shapes and phases of TiO_2 nanoparticles. Anatase is the most stable polymorph around the 10nm length scale of particles, and has been produced in the greatest diversity of particle morphologies, although kinetic routes have been well-documented to create different phases as well[21]. The stability of anatase, and its particularly large bandgap and free electron mobility in the conduction band, render it well suited for studies of functional charge-mediated transformations, as will be described in the remainder of this dissertation.

The electronic properties of TiO_2 are consistent with a d2 MO_6 octahedral metal-oxide semiconductor. The molecular orbital bonding scheme in TiO_2 places the Fermi level at the top of the valence band, which has mostly O 2p character. An unoccupied Ti 3d band lies above a bandgap of about 3.2 eV in anatase[22,23]. The tetragonal unit cell of anatase TiO_2 splits the 3d orbital into azimuthal and axial states, with remarkable implications on the effective mass and transport properties of carriers and excitons along the different crystal planes of the material[24,25]. Nonetheless, the density of states at the bottom of the conduction band in TiO_2 is quite high and thin films of donor-doped TiO_2 can have electron conductivities approaching industry standard ITO, the industry standard TCO material for optoelectronic devices [26].

The band-like conduction band of TiO_2 can be exploited by degenerately doping the bulk lattice to raise the Fermi level. One successful approach is to substitutionally dope anatase TiO_2 with niobium. Nb dopants ionize to Nb^{5+} within the anatase lattice, compensating an increase in free carrier concentration:

$$Ti_{Ti}^{x} + Nb(g) \rightarrow Nb_{Ti}^{\cdot} + e' + Ti(g)$$

The activation of Nb in thin films of anatase can be very efficient, approaching 100% dopant activation within the measurement error of Hall measurement studies[26]. Nb-doped TiO_2 retains the high electron mobility of the undoped anatase conduction band, and this doping strategy has been proposed to create low-cost transparent conductive oxide coatings for optoelectronic applictions[26]. The conduction band of anatase TiO_2 can also be accessed by tuning the oxygen vacancy defect equilibrium, through low oxygen partial pressure annealing or other synthetic strategies[27]:

$$O_O^x \rightarrow V_O^{\cdot\cdot} + 2e' + \frac{1}{2}O_2(g)$$

Both of these synthetic doping strategies are complementary to traditional gating methods to tune the Fermi level in TiO_2 nanocrystals. Spectroelectrochemical charging experiments have observed classical semiconductor gating behavior in TiO_2 nanocrystal films when they are charged as a working electrode in an electrochemical cell. Optical measurements of light attenuation from free electrons have been used to estimate a depletion layer in stoichiometric 15 nm TiO_2 nanocrystals that extends to a theoretical value of 1 μm in oxidized particles and an accumulation layer of roughly 1 nm in reduced particles[28]. TiO_2 thus presents a rich opportunity to study classical semiconductor gating behavior in a nanocrystal geometry.

The polar lattice in TiO_2 can cause electron correlation and electron-lattice coupling in highly doped systems, leading to polaronic transport and optical behavior. Degenerately doped TiO_2 demonstrates an effective mass that increases with free carrier concentration[24], consistent with self-trapping effects. ARPES measurements have been used to estimate a Frohlich coupling parameter of about 2 in photoexcited anatase TiO_2, leading to moderate large polaron transport at low carrier concentrations and lightly correlated metallic behavior at higher carrier concentrations [29]. Electron-lattice coupling

becomes much more apparent when small cations, such as Li^+, are intercalated in the lattice, leading to localized electron trapping near interstial Li ions:

$$Ti_{Ti}^{x} + Li^{+} + e' \rightarrow Ti_{Ti}' + Li_{Li}^{\circ}$$

The localized trap-state generates a mid-gap optical absorption feature in the visible range[30,31]. This effect has been used to create electrochromic devices from TiO_2, by modulating the visible polaron absorption with an electrochemical potential to lithiate and delithiate the anatase electrode[32].

VO_2 : a correlated oxide that undergoes dramatic transformations

The initial material platform studied in this dissertation, anatase TiO_2, shows nearly free electron behavior and classical semiconductor responses to charging, with interesting exceptions when small ions are intercalated into the lattice. A contrasting material system is VO_2, which displays electron and spin correlations and structural instabilities that dominate optical and electronic behavior. At the local level, VO_2 has a similar physical structure as TiO_2. The rutile phase of VO_2, bulk stable at high temperatures, is a tetragonal unit cell composed of adjacent MO_6 octahedra. It is a d3 semiconductor, and the additional electron occupies the V 3d orbital of the conduction band, leading to metallic electronic behavior and infrared reflectivity. However, at lower temperatures a dimerized monoclinic structure is stable, with insulating electronic behavior and optical transparency. This transformation is reversible, occurs around 68°C, and can happen in as little as 2 ns with a rapid current pulse [33]. VO_2 has thus been proposed as a material for thermochromic window coatings that can change from infrared transparent to reflective as the temperature increases above the threshold temperature, thereby modulating solar heating in buildings [34]. VO_2 has

also gained attention as a possible optoelectronic switching element, due to its robust metal-insulator transition upon heating with high-intensity light or short current pulses[35].

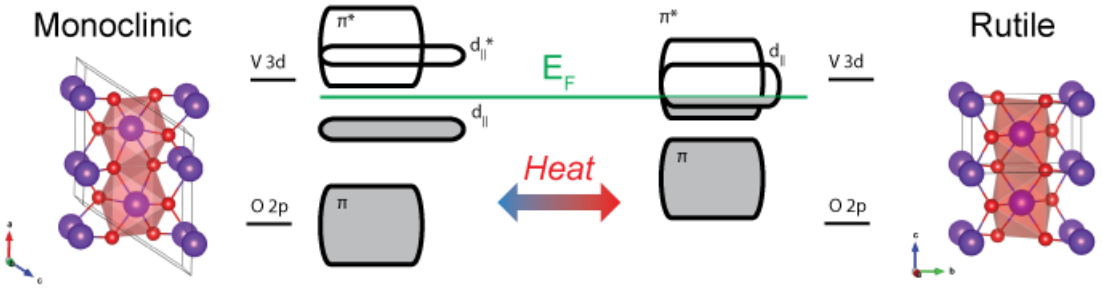

Figure 1.3: Unit cell structure and conduction band molecular orbital diagram for rutile and monoclinic VO_2

The thermochromic transition of VO_2 has been extensively studied since the transformation was first observed by Morin in 1959 [36,37]. The monoclinic and rutile phases show distinct structural, electronic and magnetic properties. The classical theories of the MIT in VO_2 are attributed to Goodenough [38] and Zylberstejn and Mott [39]. Rutile is a simple tetragonal unit cell with a half-filled V 3-d band and paramagnetic, metallic behavior. This half-filled band leads to an instability in the rutile structure, due to a combination of a Peierl's structural instability and Mott-Hubbard spin-correlations. Structural dimerization of V-V bonding along the rutile *c*-axis allows for spin correlation and Peierl's stabilization that renders the monoclinic phase stable below the transition temperature of about 68°C (**Figure 1.3**). This dimerization splits the lowest energy V 3d states into two bands, inducing a bandgap at the Fermi level. The kinetic pathway of this transition, and the dominant driving force behind the phase change (be it structural or electro-magnetic in origin) is still the subject of intense research and debate [40-42].

The metal-insulator transition in VO_2 yields abrupt changes in properties that can eclipse the magnitude of traditional gate-controlled fermi level shifts in classical semiconductors. Thus, researchers have sought to use electronic stimuli to modulate the VO_2 MIT to integrate this transformation in electronic devices. At nanometer length scales, a metallic state can be induced even at low temperatures by applying an electrochemical gate voltage to accumulate charge in VO_2 [43]. The origin of this induced metallicity at low temperatures has been the subject of recent debate. One explanation is that intense electric fields at the VO_2-electrolyte interface induce high enough local carrier concentrations to trigger an avalanche-cascade effect to populate free carriers in the bulk electrode [43,44]. An alternative hypothesis is that the intense gating potentials in an electrochemical geometry allow oxygen to leave the VO_2 lattice, distorting the inherent monoclinic structure and relaxing the dimerization conditions that cause insulating behavior [45-47]. Regardless of the origin of this transformation, the behavior is observed to be highly dependent on film thickness, orientation and interfaces with the substrate and electrolyte[44,47]. These size and interfacial effects can be expected to influence the electrochemical response in colloidal VO_2 nanocrystals as well.

LIGHT-MATTER INTERACTIONS WITH FREE CARRIERS

The interaction of free carriers with light in semiconductors is highly dependent on size, interfacial boundaries and charge-mediated transformations. At the bulk limit of conductive metals, band electrons can be polarized by infrared light, leading to broad reflectivity with an intensity that scales with carrier concentration and mobility. If the same metal is microstructured into particles with a similar size to the wavelength of light, the material can now scatter light with a different dispersion than the bulk material, according

to Rayleigh scattering theory. Even smaller particles of this same metal (<100 nm) instead will absorb light, and with greater attenuation cross-section and higher energies than observed in the bulk reflectivity. The dispersion and efficiency of bulk reflection, microparticle scattering and nanoscale absorption are all closely tied to the properties of free carriers in the solid, as well as the geometry and chemical character of interfaces with adjacent materials. The same principles apply to the optical response of semiconductors, albeit compounded by the effects of band gaps, defect states and phonon dispersion across the UV-Infrared spectrum. Furthermore, these properties can change quite drastically upon charging in semiconductors, because of the low intrinsic conductivity of unbiased semiconductors and the influence of charging on optically active polaronic and defect states (**Figure 1.4**). Engineers have exploited charge-induced changes in the optical response of semiconductors to modulate the transmission of UV-infrared light through transparent optical coatings for electrochromic smart windows (**Figure 1.4**)[48]. The size, interface and charge dependence of light-matter interactions in semiconductors can also be an analytical probe of the electronic and structural behavior of functional materials, including classical semiconductors like ZnO and TiO_2 [28,49,50] and correlated materials like VO_2 and perovskite oxides [51,52].

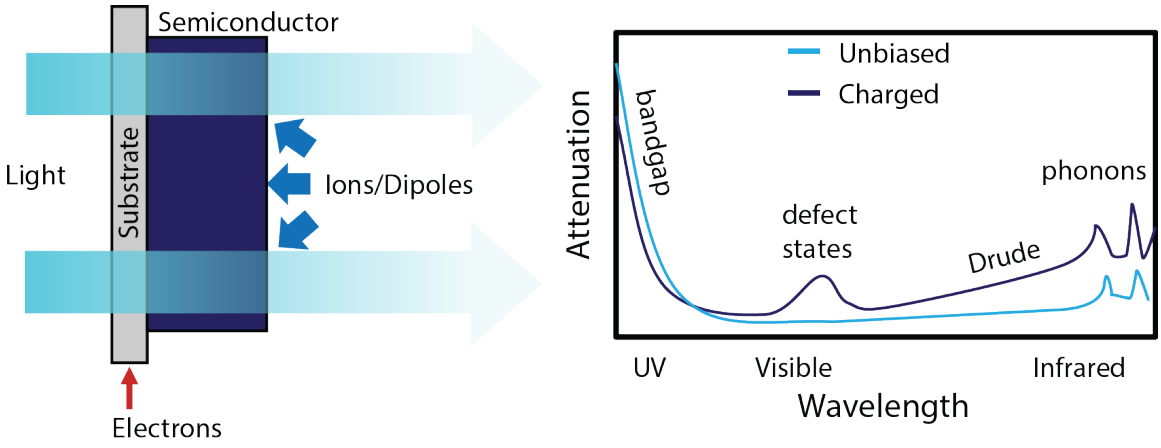

Figure 1.4: Electrochromic optical responses in charged semiconductors.

A schematic showing the qualitative changes in optical attenuation of transmitted light as a semiconductor coating is charged. Upon electrochemical reduction, the attenuation profile of a reduced semiconductor shows changes in optical bandgap, defect state absorption and the infrared Drude response.

The response of a material to incident light can be analyzed by the complex refractive index, which relates the propagation momentum (wavevector) of light through a medium to frequency. Treating light as a traveling plane wave with a wavevector ($\vec{K}$), and frequency (ω) at location ($\vec{r}$) and time (t),

$$\vec{E}(\vec{r},t) = \vec{E}_0 e^{i(\vec{K}\cdot\vec{r}-\omega t)}$$

The wavevector $\vec{K}$ can be expressed as a function of the frequency-dependent complex refractive index of light in a medium, $\tilde{n}$:

$$\vec{K} = \frac{\omega}{c}\tilde{n}(\omega)$$

$$\tilde{n} = n(\omega) + ik(\omega)$$

The real part of the complex refractive index, n, indicates phase velocity in a material, while the complex component, k, is called the extinction coefficient. The meaning of these labels can be seen by plugging in this definition to the wave propagation of light:

$$\vec{E}(\vec{r},t) = \vec{E}_0 e^{i\left(\frac{\omega}{c}\tilde{n}\cdot\vec{r}-\omega t\right)} = \vec{E}_0 e^{i\left(\frac{\omega}{c}n\cdot\vec{r}-\omega t\right)} e^{-\frac{\omega}{c}k\cdot\vec{r}}$$

At non-zero values of the extinction coefficient, k, the wave will decay as it propagates in space through the material. The extinction coefficient is thus a measure of the absorptive loss of light in the material. To enable more straightforward comparison between optical and electronic properties of a material, the complex refractive index can be expressed in terms of the (frequency-dependent) complex dielectric function $\tilde{\varepsilon}$,

$$\tilde{\varepsilon} = \varepsilon' + i\varepsilon'' = (n + ik)^2$$

$$\varepsilon' = n^2 - k^2$$

$$\varepsilon'' = 2nk$$

The practical implications of this relationship are that materials with a nonzero imaginary dielectric response, ε'', will be lossy and absorb light, while materials with a negative real component of the dielectric will reflect incident light. Transparent insulating materials will typically show positive real dielectric response and extinction approaching zero, allowing light to propagate more freely through the material.

The dielectric dispersion of conducting materials can be approximated by the Drude model[53,54], treating carriers as uncorrelated free charges that scatter at a damping frequency Γ:

$$\varepsilon_D = 1 - \frac{\omega_p^2}{\omega^2 - i\omega\Gamma}$$

The model is parameterized by the plasma frequency, ω_p, which is related to the carrier concentration, n_e, (assumed to be electrons in this case) and effective mass, m^*, with the vacuum permittivity ε_0 and electron charge e:

$$\omega_p = \sqrt{\frac{n_e e^2}{\varepsilon_0 m^*}}$$

The imaginary and real components of this response are plotted in **Figure 1.5a**, showing a rising imaginary dielectric for lower energies corresponding to conductivity losses, and a negative real dielectric that suggests high reflectivity. These trends are consistent with the observed reflectivity and opacity in conductive metals like silver. This model explains how the reflectivity of a material scales with carrier concentration, as more conductive materials will have a higher plasma frequency.

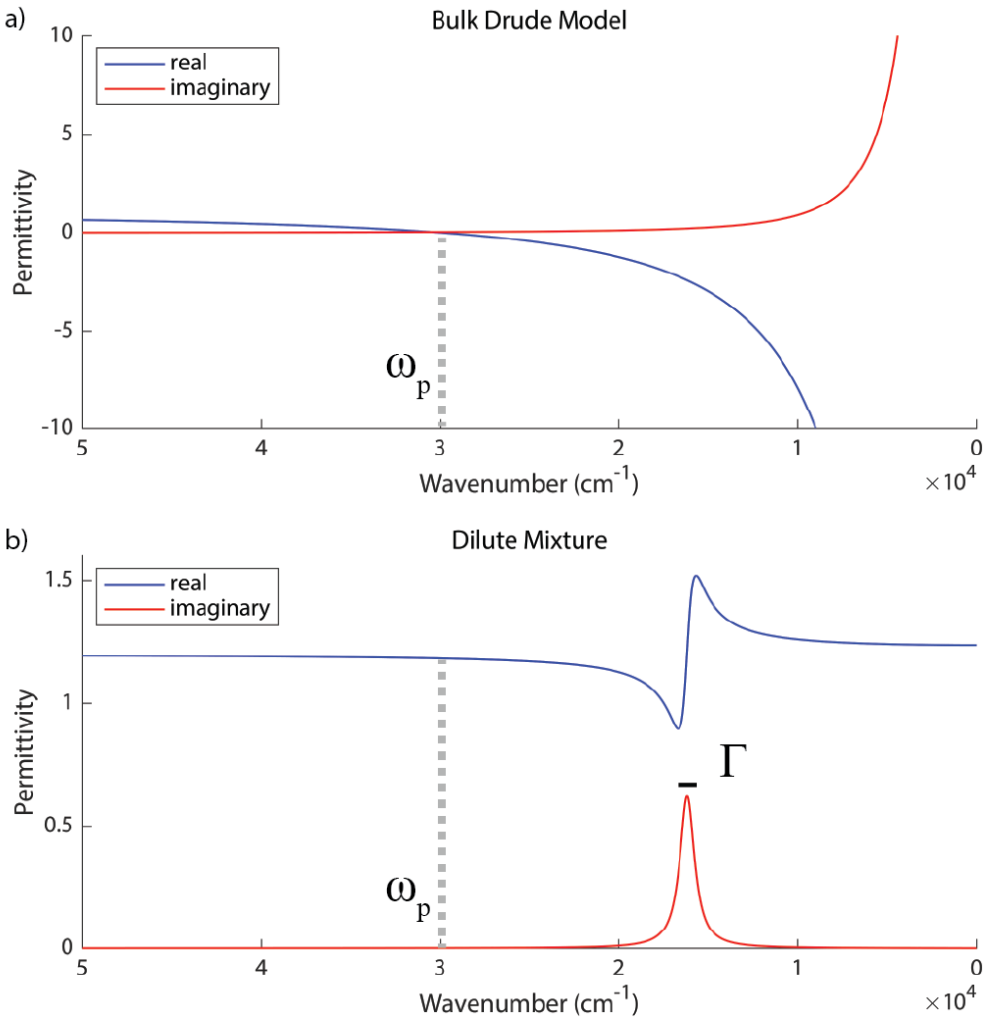

Figure 1.5: The complex diectric response of a Drude metal

Imaginary and real parts of the complex dielectric response of a) a bulk Drude metal and b) a dilute dispersion of the same Drude metal according to the Mie approximation for spherical inclusions. The plasma frequency, ω_p, and damping constant, Γ, are included and scaled to the plot axes for reference.

The optical response of free carriers is dramatically different when the material is confined to small sizes in an insulating matrix. The theory of localized plasmons was developed by Mie, who solved Maxwell's equations analytically for a small spherical

Drude metal particle immersed in an insulating, non-dispersive medium[54,55]. The scattering and absorption cross-sections for a particle of radius R is calculated as:

$$\sigma_{sca}(\omega) = 4\pi R^2 \left(\frac{2\pi\omega}{c}\varepsilon_H^{1/2}R\right)^4 \left|\frac{\varepsilon_P(\omega)-\varepsilon_H}{\varepsilon_P(\omega)+2\varepsilon_H}\right|^2$$

$$\sigma_{abs}(\omega) = 4\pi R^2 \left(\frac{2\pi\omega}{c}\varepsilon_H^{1/2}R\right) \mathrm{Im}\left\{\frac{\varepsilon_P(\omega)-\varepsilon_H}{\varepsilon_P(\omega)+2\varepsilon_H}\right\}$$

Here, $\varepsilon_P(\omega)$ is the frequency dependent dielectric function of the particle, determined by the Drude model, and ε_H is the non-dispersive dielectric constant of the insulating matrix around the particle. The additional R^3 size dependence in scattering creates a large size dependence for the relative strengths of scattering and absorption in the particle. Particles that are significantly smaller than the wavelength of incident light are overwhelmingly dominated by optical absorption, rather than scatter[56]. Thus, colloidal nanocrystals with length scales below 100 nm absorb light at frequencies defined by the Drude model and geometry constraints of the particle-matrix interface. **Figure 1.5b** compares the complex dielectric response of a metal colloid to the same material in the bulk. The colloidal dispersion shows a resonant absorption peak to the red of the plasma frequency parameter, and a defined by the host medium. This resonant absorption feature is called localized surface plasmon resonance (LSPR), and has inspired a rich diversity of research on colloidal metals and semiconductors [56,57]. At particle concentrations much larger than the dilute limit assumed in the Mie approximation, plasmon coupling and effective medium properties must be considered in the macroscopic optical response of an ensemble of particles [58].

The optical response of a Drude-like conductor can be manipulated by changing the carrier properties of the material. The plasma frequency ω_p (and resonant absorption peak energy) scale with the square root of carrier density and inverse effective mass.

Carrier damping, which is related to electronic mobility in a conductor, also affects the absorption intensity and energy. The optical response of a conducting nanomaterial can thus be manipulated by changing these properties, either through synthetic or electronic charging. Gating a plasmonic colloid can increase the free carrier concentration in a particle, leading to a blue shift and absorption increase at the resonant LSPR frequency. The simulated response of 20 nm particles of a metal (similar to gold) and semiconductor (similar to In_2O_3) upon charge accumulation of 10^{21} electrons/cm^3 reveals the different LSPR responses of metals and semiconductors to electronic modulation (**Figure 1.6**). The metal particles absorb much more strongly and at higher energy than the semiconductor, but the modulation in peak intensity and energy is much greater in the semiconductor due to a larger relative change in carrier concentration. The larger damping coefficient in the semiconductor also contributes to a wider peak profile compared to the metal. The LSPR response of a semiconductor is thus a sensitive probe of the carrier properties in nanoconfined semiconductor during charge-mediated transformations.

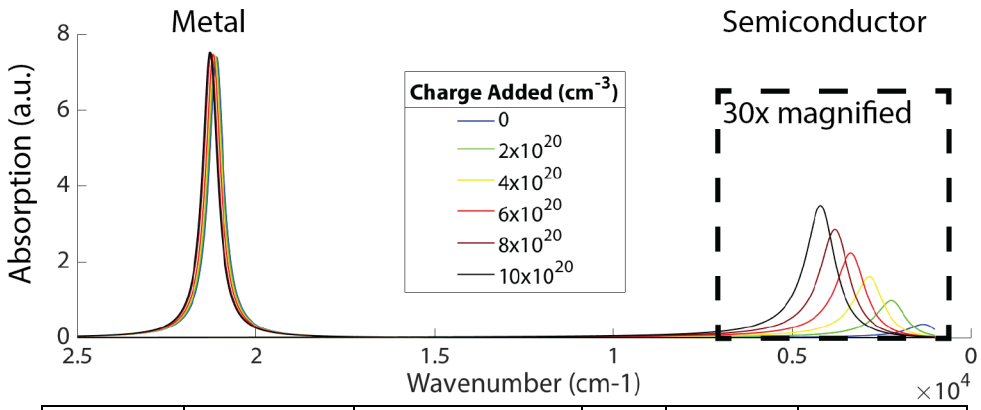

	ω_p (cm^{-1})	Γ (cm^{-1})	m^*	ε_∞	$\varepsilon_{Solvent}$
Metal	70000	500	1.1	1	5
S.C.	5000	1000	0.4	4	5

Figure 1.6: Simulated absorption of metal and semiconductor nanocrystals

Simulated absorption cross section (optical density) of a metallic nanocrystal similar to gold, and semiconductor nanocrystal similar to In_2O_3. The absorption scales linearly with particle concentration, and the absolute magnitude of absorption is plotted on an arbitrary scale for comparison.

THEORY OF PHASE TRANSFORMATIONS

Semiconductors can undergo structural transformations when a charge or other impetus is applied. The polar lattice in metal oxide semiconductors can tolerate a rich diversity of long-range crystal structures and defect equilibria that can have dramatic effects on functional properties. The transitions between these different structural phases create new functionalities for integrated semiconductor applications beyond classical Fermi level control across interfaces, as observed in the dramatic metal-insulator transition in electrochromic VO_2 thin films [43]. The nanoscale geometry of colloidal metal oxide

nanocrystals introduces additional surface energy that can perturb phase equilibria and transformation kinetics relative to bulk materials. The response of semiconductor nanocrystals to charging can extend to structural phase transformations and other major phase transitions that may depend significantly on interface geometry, nanoscale confinement and charge transport pathways. Thus, a thorough understanding of the charging responses of semiconductors nanomaterials should acknowledge the fundamental principles of phase equilibria and transformation kinetics.

At thermal equilibrium, a system will tend towards its free energy minimum. A phase transformation can occur when some input on the system shifts the relative energetics between two states. The same principles apply to a system undergoing a charge-mediated transformation. When an electronic charge is applied, the phase state of the material can be defined by the degree of charging in the system. For instance, if the system compensates accumulated charge by intercalating Li^+ in the electrode, causing a change in the semiconductor structure, the particular 'phase' of the material can be defined by the relative concentration of Li in the solid. This phase state can thus be labeled by the degree of charging, ranging from 0 for a completely unbiased system, to 1 for a fully reduced system. A continuous transformation can occur if the energetics of the system permit only a single local minimum across the entire degree of charging, as shown in **Figure 1.7a**. As a charge (current or field) is applied, the free energy minimum increases to larger degrees of charging. The continuous relationship between the charging degree and applied potential indicates that the material undergoes a continuous transformation. An intercalating electrode material that undergoes a continuous transformation upon charge would have a wide solid solution miscibility of the intercalating cation in the solid. Different behavior can be observed if the free energy landscape yields multiple local minima, as shown in **Figure 1.7b**. Changing the applied potential does not shift the degree of charge until a

threshold potential (E_c) is reached. At this threshold, there may be coexistence between the two equal-energy minima in the degree of charge, yielding a heterogeneous mixture of phases defined by the two minima. At potentials beyond this threshold value, the higher degree of charge minima becomes globally stable, and the material rests at a stable charging degree for larger potentials. This behavior is called a 1st order transition per the Ehrenfest classification, because of the discontinuity in the first derivative of the Gibbs free energy[59,60], and characterizes the abrupt transformations often seen in Li-ion battery electrodes, and familiar in common processes such as solidification.

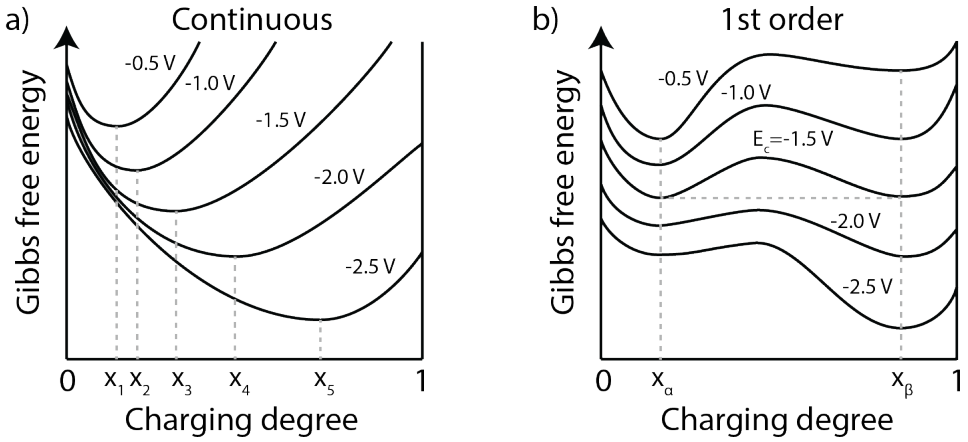

Figure 1.7: Free energy schematics of a phase transforming material

a) Continuous phase transformations and b) 1st order phase transformations under different applied potentials. The equilibrium degree of charging changes linearly with potential in the continuous transformation, but switches discretely from the x_α to x_β once the threshold potential E_c is exceeded in the 1st order transformation.

The energetics of the system depend on composition and morphology. During charge-mediated transformations of solid semiconductors, the shape of the energy

equilibria depends on the interaction between charges and the charged solid. If charges can be treated as free carriers, a continuous phase transformation is likely, as in the case of semiconductor gating inducing a continuous change in free carrier concentration with charging potential. However, if the charging species interact with the semiconductor, there may be local minima at different charging degrees that favor certain structures. The sensitivity of the compositional minimum to the applied potential depends on the interaction between the insertion material and the innate crystal structure of the electrode. Methods such as DFT, or more coarse-grained generalizations of particular lattice types, bond character and polarity may be used to model this dependence. A further complicating factor in 1st order charge-mediated transitions in semiconductors is the surface energy of nanoconfined materials. A particle with the same size and shape may have unique total surface energies for each stable phase across a 1st order transition. Thus, the local minima in total energy will be perturbed asymmetrically, leading to a distortion in the effective potential (or charge) at which the phase transition occurs. Size and composition heterogeneity within an ensemble of phase-changing particles can blur the threshold of the 1st order phase transition, leading to non-intuitive macroscopic behavior [61-63].

In practice, the macroscopic behavior of semiconductor nanomaterials during charge-mediated transformations may depend on transformation kinetics as much as phase equilibria. During charging, electrons flow into the semiconductor along an electrically conductive interface, and charge is compensated by changes in material properties or the diffusion of compensating charged species at an electrolyte interface. Both heterogeneous reactions can be limited by the rates of diffusion, nucleation and phase propagation within each component of the electrochemical cell, and the relative dominance of these processes can vary with applied potential, current density and other factors. A full accounting of the behavior of semiconductor materials in response to electrochemical charge must take

careful note of the kinetics of these different charging processes. In typical charging schemes, the conductivity and diffusivity of the semiconductor solid is much lower than the other components of the electronic or electrochemical cell, and the behavior of the semiconductor can be isolated. Several approaches have been developed to model the kinetics of charge mediated 1st order phase transformations in nanoparticles. At the macroscopic scale, the JMA theory can be used to compare kinetic charging rates to homogeneous nucleation and growth kinetics in a homogenized semiconductor model[64,65]. Spatially-refined transport models at the single particle level, called phase field models, have also been used to study the observed transformation behavior of charged particles [66]. 1st principles DFT and Monte Carlo approaches can also be used to study these phase transformations on an atomistic scale[67]. Charging dynamics in semiconductor materials are an active area of investigation in the battery community, and have far-reaching consequences in the fields of electrochromics, catalysis, ion exchange membranes and photovoltaics.

DISSERTATION OVERVIEW

This dissertation explores the manipulation of two classes of materials – anatase TiO_2 nanocrystals and VO_2 nanocrystalline films – upon electrochemical charging. The goal of this dissertation is to investigate the role of nanoscale geometry in mediating functional charge transfer processes and electrochemical phase transformations in semiconductors, and to develop new functionalities that result from these materials preparations.

The first study, in Chapter 2, explores the electrochromic response of Nb-doped anatase TiO_2 nanocrystals to electrochemical reduction through two independent avenues

of charging. The material demonstrates distinct optical responses due to surficial compensated charging and intercalative charging pathways. Surface-compensated charging modulates the electronic carrier concentration in the nanocrystal bulk, yielding dramatic changes in infrared optical absorption due to the Drude free-carrier dielectric response. At lower reducing potentials, a first-order lithium intercalation reaction occurs, leading to a visible spectrum coloration due to polaronic absorption from interstitial Li^+ cation defects. These two coloration pathways can be independently controlled by tuning the applied electrochemical potential with technological applications for dual spectrum electrochromic window coatings.

The surficial charging pathway in electrochemically reduced anatase TiO_2 nanocrystals is studied in more detail in Chapter 3. TiO_2 nanocrystals with different concentrations of substitutional Nb-doping are analyzed for changes in infrared optical density with doping or electrochemical charging. In principle, either of these compensation mechanisms will yield similar changes in free carrier concentration, and a localized surface plasmon resonant response in the infrared. The differences between these two charge compensation mechanisms are studied by examining FTIR transmission spectra of films of Nb-doped TiO_2 nanocrystals during *ex situ* electrochemical reduction. The impacts of Nb doping and electrochemical charging are quantified by Drude theory fits to FTIR spectra, and reveal different carrier properties in the two modes of carrier compensation.

Lithium intercalation in anatase TiO_2 nanocrystals occurs through the transport of Li^+ cations across the nanocrystal surface and into the bulk of the particle. This diffusion process, along with the accompanying electronic charge compensation, progresses through a 1st order phase transformation with applied potential. Chapter 4 studies the role of nanocrystal size and shape on the thermodynamics and kinetics of this intercalative phase transformation. A set of substoichiometric TiO_{2-x} nanoplatelets of different dimensions are

synthesized and compared for their electrochemical response in a Li-ion cell. The state of charge of thin films of TiO_{2-x} nanoplatelets are quantified through *in situ* optical spectroscopy to precisely monitor the intercalation process following minor changes in potential and charge. The kinetics of the lithiation reaction are parameterized by an adapted nucleation and growth model, and nanocrystal ensembles are found to show macroscopic effects on charging dynamics due to heterogeneity between particles.

An applied electric field can also induce dramatic phase transformations without direct ion intercalation. Chapter 5 studies the electrochromic response of nanocrystalline VO_2 films upon electrochemical reduction. This material undergoes a dramatic progression of transformations during electrochemical reduction in a non-intercalating electrolyte. An applied electric field changes the carrier concentration in VO_2 through surface compensation from an ionic double layer and charged defects in the lattice. The reduced nanocrystalline film first undergoes a rapid transition to a persistant metallic, oxygen-deficient $VO_{2-\delta}$ monoclinic phase, followed by a slower transition to an insulating, $VO_{2-\delta-x}$ expanded rutile-like state after sufficient charging. This insulator-metal-insulator transition is found to be accompanied by electronic and structural transformations through X-ray spectroscopies. Furthermore, the secondary metal-insulator transition to $VO_{2-\delta-x}$ is observed to follow size-dependent kinetics, such that the transformation only occurs under feasible time scales for nanocrystalline grains that are smaller than 50 nm. The nanoscale geometry dependence of this transformation is discussed, with implications for controlling the metal-insulator transformation in other correlated semiconductor nanomaterials.

Chapter 2: Spectroelectrochemical Signatures of Capacitive Charging and Ion Insertion in Doped Anatase Titania Nanocrystals Chapter*

ABSTRACT

Solution-processed films of colloidal aliovalent niobium-doped anatase TiO_2 nanocrystals exhibit modulation of optical transmittance in two spectral regions – near-infrared (NIR) and visible light – as they undergo progressive and reversible charging in an electrochemical cell. The Nb-TiO_2 nanocrystal film supports a localized surface plasmon resonance in the NIR, which can be dynamically modulated via capacitive charging. When the nanocrystals are charged by insertion of lithium ions, inducing a well-known structural phase transition of the anatase lattice, strong modulation of visible transmittance is observed. Based on X-Ray Absorption Near-edge Spectroscopy, the conduction electrons localize only upon lithium ion insertion, thus rationalizing the two modes of optical switching observed in a single material. These multi-modal electrochromic properties show promise for application in dynamic optical filters or smart windows.

INTRODUCTION

Electrochromic materials, which change color, transparency, and reflectivity upon the application of an external potential, can have significant impact on energy consumption as films in architectural smart windows[69-77]. In particular, precise independent spectral control over material transmittance in the visible and near-infrared (NIR) regimes of the solar spectrum is necessary to develop next-generation electrochromic smart-windows for improved energy efficiency in buildings. Amorphous transition metal oxides, especially

* Content for this chapter was adapted from Dahlman *et al*[68]. C.J. Dahlman was the lead author on this study and developed the ideas, experiments and analysis presented in this chapter.

WO_3, have been the most studied materials for electrochromic windows; they exhibit optical modulation primarily in the visible range due to localized excitations of reduced metal cations[32,74]. Some metal oxide semiconductors, when synthesized instead as colloidal nanocrystals (NCs), are capable of supporting tunable localized surface plasmon resonance (LSPR) that interacts with NIR light, forming the basis for spectrally complementary electrochromic modulation[11,26,77-80].

We hypothesized that in doped transition metal oxide NCs, the visible-band optical modulation due to the traditional cation intercalation process could co-exist with the NIR LSPR extinction. This NIR effect has been previously shown to be tunable by synthetic doping[11,81] and can be modulated post-synthetically by electrochemical charging in the case of Sn-doped indium oxide (ITO)[82,83] and aluminum-doped zinc oxide (AZO) NCs[84,85]. Thus, NCs of synthetically doped transition metal oxides should be capable of independent modulation in two spectral bands (visible and NIR) within a single-component functional film. Here, we demonstrate such dual-mode modulation in anatase TiO_2 doped with niobium.

Anatase TiO_2 is a well-known lithium insertion material that has been studied as a battery electrode[69,71,72,86-88]. Attempts to improve the slow lithium diffusion kinetics and conductivity of bulk anatase have yielded nanostructured TiO_2 electrodes that demonstrate significant improvements in charge capacity and charging rates[30,69,71-77,89]. Surface charging has been hypothesized to account for nearly as much charge capacity as the lithium insertion reaction in TiO_2 once particle sizes approach 10 nm[32,74]. Along with nanostructuring, the electrochemical behavior of TiO_2 electrodes has been improved by aliovalent doping with niobium or tantalum to increase the inherently low conductivity of TiO_2[26,77-80,82]. At diameters around ten nanometers, degenerately doped NCs can support LSPR which can be tuned across the infrared and visible spectrum by varying the NC size,

shape, composition and Fermi level, as seen in ITO, AZO, and other semiconductor colloidal NCs[11,81,90]. Niobium-doped anatase TiO_2 (Nb-TiO_2) exhibits a broad mid-IR LSPR extinction peak when synthesized as 10 nm diameter colloidal NCs, which can be tuned in amplitude and energy by varying the amount of Nb doping[82]. Anatase TiO_2 is also known to be electrochromic; intercalation of Li^+ produces a visible extinction feature at about 730 nm[67,75,84,91-93]. This peak has been ascribed to localization of injected electrons on Ti cations[72-76,86], creating a polaronic lattice distortion[30,74,89], which is similar to the proposed mechanisms for electrochromism in amorphous transition metal oxides such as WO_3 and NbO_x[32,73,94].

EXPERIMENTAL SECTION

Nb-TiO_2 NCs were synthesized by a slightly modified literature procedure[82,92]. Nb doping content in this study is expressed as the percentage of Ti sites occupied by Nb in the anatase structure, as measured by Inductively Coupled Plasma-Optical Emission Spectroscopy. The Nb:Ti ratio in the feedstock was found to be roughly equal to the substitutionally doped NC cation ratio up to about 10% Nb substitutional content. Excess Nb precursor was required to dope beyond 10% and it was difficult to achieve doping concentrations above 20%.

Conductive mesoporous films of colloidal TiO_2 NCs were prepared by spin coating solutions of ligand-stripped NCs and annealing. The oleic acid ligands bound to the surface of the colloidal NCs upon synthesis were stripped in solution using nitrosonium tetrafluoroborate ($NOBF_4$), following literature procedures[90,92]. The ligand-stripped particles in a solution of acetonitrile and N,N-dimethylformamide (4:1 by volume) were spin-cast on either ITO-coated glass or silicon wafers. Uniform films of 100-200 nm were

confirmed by profilometry. The films were annealed under argon at 300°C for 30 min to remove residual organics.

For electrochemical testing, the NC coated substrate was used as the working electrode and a single strip of lithium metal was used as both the counter and reference electrode, under an argon atmosphere. Transmission spectra were recorded *in situ* during cycling using a fiber-coupled spectrometer. Strong absorption bands from the liquid electrolyte limited the spectral window to 400-2200 nm for these *in situ* experiments.

Ex situ X-ray diffraction (XRD) of electrochemically charged NC films was performed at the Stanford Synchrotron Radiation Laboratory (SSRL) at beamline 11-3. Diffraction patterns were obtained in transmission and, for some data in the Supporting Information, grazing-incidence. Substrates of p-type (boron doped) silicon wafers were used for transmission experiments. NC films were electrochemically charged as described above, then rinsed with dimethyl carbonate to prevent deposition of salts from the electrolyte. The charged films were sealed air-free in a Kapton pouch; single-crystal silicon peaks were subtracted out using baseline patterns from an uncoated portion of the sample substrate.

Ex situ X-ray absorption spectra were collected at the Advanced Light Source (ALS) at beamline 10.3.2 by detection of X-ray fluorescence. Films of electrochemically charged ligand-stripped NCs were prepared as described above for synchrotron XRD. The charged films were mounted on an aluminum sample holder and sealed with a thin Mylar film.

Ex situ mid-IR extinction measurements of the charged NC films were obtained using a Fourier Transform Infrared (FTIR) spectrometer. Undoped silicon substrates were coated with 3 nm of chromium followed by 10 nm of gold to provide a conductive but semi-transparent substrate. Ligand-stripped NC films around 500 nm thick were coated by

spin-coating, then charged and rinsed, as described above. The charged films were assembled air-free into an O-ring sealed cell with a CaF_2 window for measurement in transmission mode.

DISCUSSION

The synthesized NCs are 11 nm cuboids for doping levels up to about 10% Nb, above which they become slightly larger, more polydisperse and anisotropic, consistent with previously published results (**Figure 2.1a,b**)[30,82,84,95]. Spin coated films are optically clear and free of gross defects (**Figure 2.1c**).

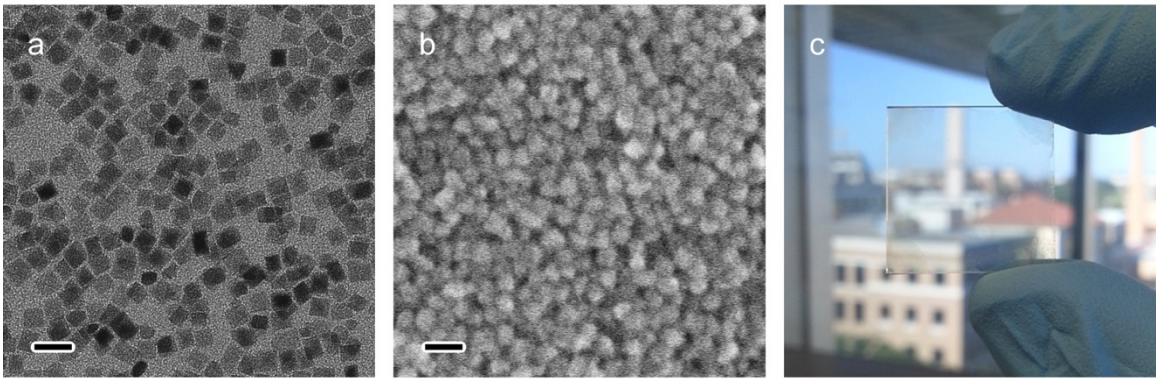

Figure 2.1: TEM, SEM and optical characterization Nb-TiO_2 NC film.
a) Low-resolution TEM image of 2% Nb-doped TiO_2 NCs. The scale bar is 20 nm. b) Top-down SEM of a spincoated film of 5% Nb-TiO_2 NCs. The scale bar is 20 nm. c) Photograph of a 2 cm square ITO-coated glass substrate coated by a 180 nm thick film of 5% Nb-TiO_2 NCs.

We charged and discharged films of ligand-stripped NCs in galvanostatic mode to test the impact of Nb doping on electrochemical behavior. A lithium-based liquid

electrolyte – 0.1M bis(trifluoromethane)sulfonimide lithium (LiTFSI) in tetraglyme – was used. The voltage profiles (**Figure 2.2**), normalized by empirical discharge capacity at a rate of 1C for each sample, demonstrate three distinct electrochemical regions. A charging plateau is centered near 1.8V vs Li/Li^+ with a 0.15V over-potential difference between the charge and discharge curves for the entire range of Nb doping (see **Figure A1** for expanded doping range). At potentials above and below the plateau, there is significant charging approaching both potential limits of the experiment. These observations are consistent with previous studies of anatase TiO_2 NCs, which attribute the charging plateau to a two-phase region where Li^+ intercalates into the anatase crystal lattice, leading to a distorted orthorhombic $Li_{0.5}TiO_2$ phase[22,23,67,75,91-93].

$$TiO_2 + xLi^+ + xe^- \rightleftharpoons Li_xTiO_2 \quad ; \quad x < 0.5$$

The behavior at potentials above and below the constant-voltage plateau is actively debated; capacitive charging is commonly described as a dominant process, especially for potentials below the plateau, and solid-solution intercalation of lithium in anatase is found to account for stoichiometries up to $Li_{0.2}TiO_2$ for potentials above 1.8V. The relative contributions of solid-solution intercalation and capacitive charging, particularly for potentials above 1.8V, is actively studied for nanocrystalline TiO_2[27,72-76,96,97]. The constant-voltage plateau for Nb-TiO_2 NCs accounts for about half of the charge capacity of our films, consistent with previous results for 10 nm (undoped) anatase TiO_2 NCs[74,89]. The consistency of the galvanostatic curves across doping levels reveals that Nb doping only has a minor effect on the electrochemical lithiation and delithiation of anatase TiO_2 NC thin films.

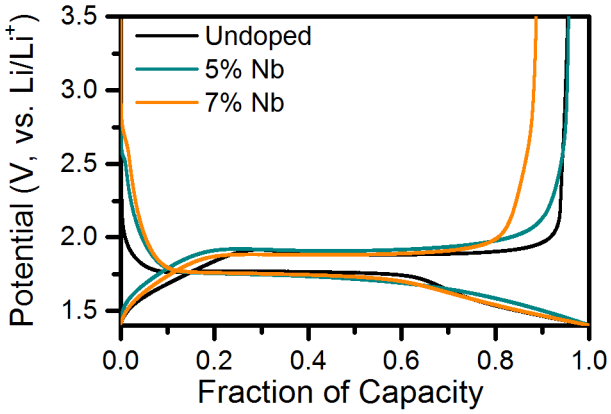

Figure 2.2: Galvanostatic charging profiles for films of Nb-TiO_2 NCs. Films were charged at an approximate rate of 1C. The electrolyte was 0.1M LiTFSI in tetraglyme.

The crystal structure of Nb-TiO_2 NCs was studied *ex situ* by XRD to assess the impact of Nb incorporation on the intercalation phase transition. The intercalation of lithium into bulk anatase TiO_2 induces a phase transition to orthorhombic $Li_{0.5}TiO_2$, observable by XRD[73,94,96,98]. Our NC films were evaluated at three points in the discharge curve: 4V (fully oxidized), 1.8V (reduced almost to the constant-voltage plateau) and 1.5V (fully reduced). Comparing our results to reference patterns for anatase TiO_2 and $Li_{0.5}TiO_2$[11,92,99], we see that the NCs transition from tetragonal anatase to orthorhombic $Li_{0.5}TiO_2$ upon crossing the constant-voltage plateau (**Figure 2.3**). The phase change reverses under oxidation, but there is some evidence for phase mixing (i.e. early, partial conversion to the anatase phase) at potentials below the 1.9V phase coexistence plateau (**Figure A3, A4**). The reversible phase behavior and general electrochemical characteristics of anatase TiO_2 NCs are maintained over a wide range of Nb doping levels (see additional XRD data, **Figure A4**). In all cases, two distinct electrochemical charging processes occur: a crystalline phase change accompanies faradaic lithium intercalation, and

a rapid charging process occurs within the anatase TiO_2 phase. These two electrochemical processes can be anticipated to yield distinct optical signatures.

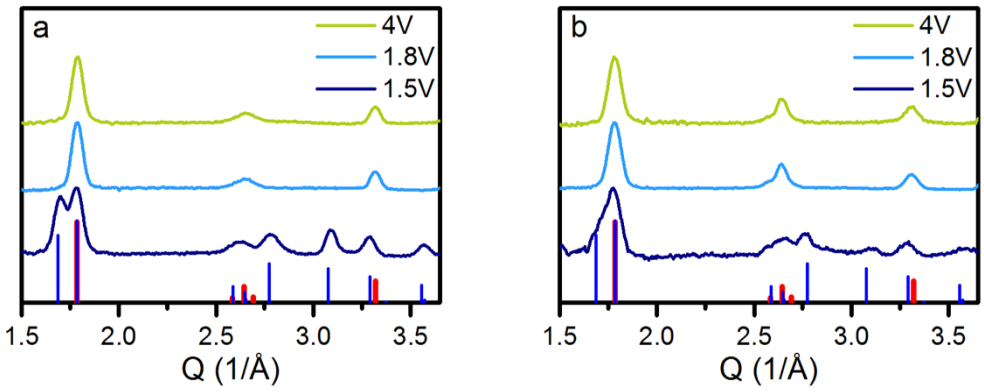

Figure 2.3: Transmission wide-angle X-ray diffraction of charged TiO_2.
a) undoped and b) 10% Nb-doped NC films. The as-deposited and partially-reduced 1.8V patterns match the anatase structure (I41/amd, ICSD Coll. Code 96946, red, and the fully reduced 1.5V pattern corresponds to the Li0.5TiO2 phase (Imma, ICSD Coll. Code 96948, blue), reported for microscale anatase TiO2[30,89,92].

Initially, Nb-TiO_2 NC films are highly transparent in the visible region and exhibit a rising extinction feature in the NIR; this NIR extinction is enhanced upon electrochemical reduction or increased Nb doping. Indeed, undoped TiO_2 NCs, initially transparent across the visible and NIR, begin to absorb in the NIR as they are charged. (**Figure 2.4**). The change in NIR optical density with applied voltage varies with Nb doping level, reaching a maximum modulation around 7% Nb (**Figure A7**). At reducing potentials beyond the phase-change threshold, a visible extinction peak arises around 730 nm, observable for all levels of Nb doping. Previous studies have reported similar visible-range electrochromism

of TiO_2 NCs reduced in Li^+ containing electrolytes[30,84,95,100-102]. However, the spectral range in those studies was limited and no significant IR modulation was observed.

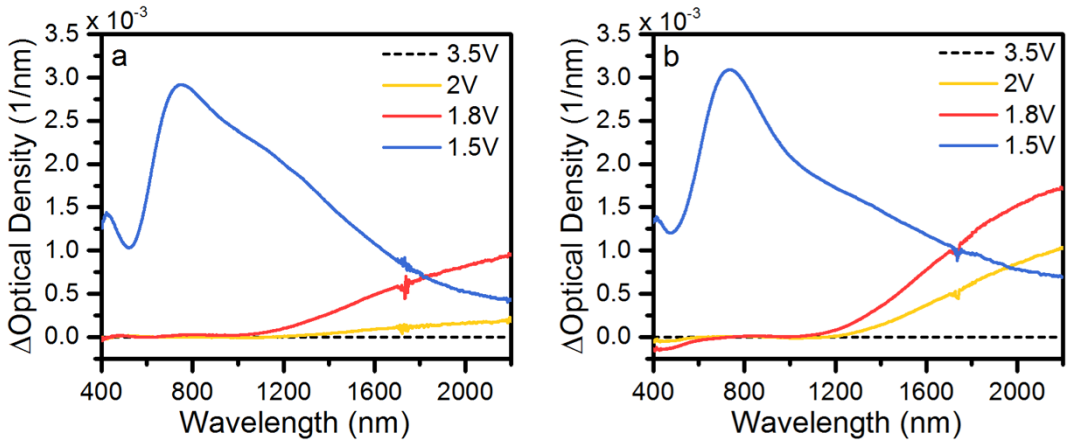

Figure 2.4: *In situ* spectroelectrochemistry of TiO_2 films.

a) undoped and b) 5% Nb-doped TiO_2 NC films. Spectra are reported as ΔOptical Density referenced to the as-deposited films, and normalized by film thickness to account for minor sample-to-sample differences. The electrolyte was 0.1M LiTFSI in tetraglyme.

The NIR transmittance modulation we observe in both undoped and Nb-TiO_2 NCs (**Figure 2.4**) suggests that electrons injected prior to the two-phase potential plateau populate delocalized conduction band states rather than self-trapping and localizing in polaronic states. The Fermi level of anatase lies within the bandgap, and the conduction band is derived primarily from Ti 3d orbitals[22,23,103]. Electron accumulation – by electrochemical charging, doping or other means - can either populate these conduction band states, generate polaronic states by self-trapping, or interact with Ti or O defects[27,82,96,97]. The literature is conflicted on which of these processes is dominant[27,89]. Recent computational studies have explained the metallic conductivity of Nb-TiO_2 with a

theory that describes substitutional Nb defects as shallow electron donors[96,98,104-106], but electrons accumulated by capacitive charging are still poorly understood. Our results suggest that capacitive electron accumulation, like Nb doping, enhances NIR LSPR extinction. Earlier studies have reported blue shifts of NIR extinction peaks and increased NIR extinction in doped metal oxide NCs under electrochemical or chemical charging and have successfully modeled these phenomena as changes to LSPR extinction upon increasing free electron concentration[11,99,107,108].

On the other hand, the visible electrochromic effect in orthorhombic $Li_{0.5}TiO_2$ is theorized to be due to polaronic reduced Ti^{3+} states[26,30,77,89], so we hypothesized that delocalized and localized excess electrons may be present at different stages of the charging process. *Ex situ* X-Ray Absorption Near-edge Spectroscopy (XANES) was used to assess the influence of Nb on polaronic charge trapping behavior of excess electrons in TiO_2 both before and as a result of electrochemical cycling. The pre-edge structure of the Ti K-edge is diagnostic of the effective oxidation state and was examined for evidence of changes in the oxidation state of Ti atoms upon doping or electrochemical charging (**Figures 2.5, 2.6**).

The effects of Nb doping on electron correlation in uncharged anatase TiO_2 are an active area of debate. Several studies have found evidence of electron correlation in Nb-TiO_2 from XPS[82,100-102] and EPR measurements[103,105,106], leading to observed Ti^{3+} sites, but de Trizio *et al*.'s recent studies of colloidal Nb-TiO_2 NCs found no evidence of electron correlation at room temperature using XPS or EPR[82,106]. The latter technique revealed localization only below about 100 K. We obtained XANES spectra of the Ti K-edge for a broad range of Nb doping (**Figure 2.5**). The Ti K-edge position, measured by the maxima of the absorption first derivative, shows no discernible shift upon any level of Nb doping (**Figure A5c**). Thus, we can confirm that Nb doping does not have a major impact on the

formal valence of Ti in these Nb-TiO_2 NCs. Oxygen stoichiometry may play a significant role in the conflict between these results and earlier studies, because the processing conditions for Nb-TiO_2 NCs used in this study – at atmospheric pressure and relatively low temperatures (below 300°C) – deviate from many earlier studies[27,105]. Although doped Nb doesn't change the formal valency of Ti, it does induce systematic changes in the pre-edge features at high doping concentrations. Using the lettering system common in the literature – A_1, A_2, A_3 for Ti 1s to 3d transitions and B for Ti 1s to 4d transitions[104-106] – we can see that beyond 20% Nb, the A_2 peak notably increases in relative intensity, along with shifts in the other peak energies and amplitudes (**Figure 2.5**). Similar effects have been attributed to symmetry breaking in the anatase lattice due to defects or strain, suggesting that high levels of doped Nb may affect the local structure of anatase TiO_2[107,108]. Nb doping has been shown to expand the anatase lattice[26,77], and Nb appears to surface segregate in Nb-TiO_2 NCs at high doping concentrations[82], so it is reasonable to expect strain associated with Nb defects to distort the symmetry of local TiO_6 octahedra.

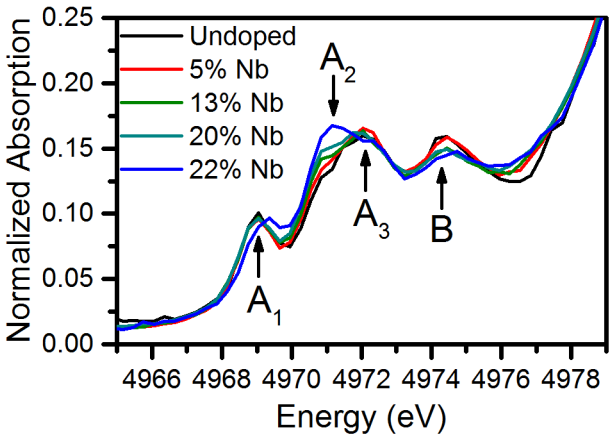

Figure 2.5: XANES Ti pre-K edge spectra for uncharged films of varying Nb doping.

The phase change from anatase to $Li_{0.5}TiO_2$ has been shown to correlate to a reduction in the average charge state of Ti cations in anatase[105,106]. Indeed, our XANES data mirrors the phase behavior we observed by XRD: for potentials above the intercalation threshold, the Ti K-edge remains at a higher energy, as expected for Ti^{4+} in anatase TiO_2[106] (**Figure 2.6**). After the orthorhombic phase change the Ti K-edge energy decreases by 2 ± 0.3 eV. Both Wagemaker *et al*.[105] and Lafont *et al*.[106] report an edge shift around 1.5 eV upon lithiation to $Ti^{3.5+}$ ($Li_{0.5}TiO_2$), for microscale and nanocrystalline anatase TiO_2 respectively. The edge shift we observe (**Figure 2.6**), suggests that Ti cations in Nb-TiO_2 NCs are reduced to an average valence of roughly $Ti^{3.5+}$ upon lithiation to the orthorhombic phase, consistent with one half Li^+ per formula unit. However, Ti valency does not change upon charging at potentials above or below the two-phase potential plateau, conflicting with previous reports of a solid solution of Li and anatase TiO_2 in these potential regions[70,72-74,106]. Likewise, we find no evidence from spectroelectrochemistry (**Figure 2.4**) to support the localization of electrons at titanium bulk or surface sites at potentials above the orthorhombic phase transition threshold. Rather, the results suggest that only $Li_{0.5}TiO_2$ demonstrates charge localization, and that capacitive charging dominates above and below the two-phase potential with the accumulated charge occupying delocalized states where it enhances NIR LSPR extinction. Lithium insertion – coupled to the orthorhombic phase transition – drives charge localization, causing the appearance of a polaronic, visible extinction peak. Considering all the XANES results (**Figures 2.5, 2.6**), we conclude that electrons in Nb-TiO_2 NCs are delocalized, as are electrons added during capacitive charging at potentials above and below the two-phase potential. Only upon lithiation do electrons localize at Ti cation sites.

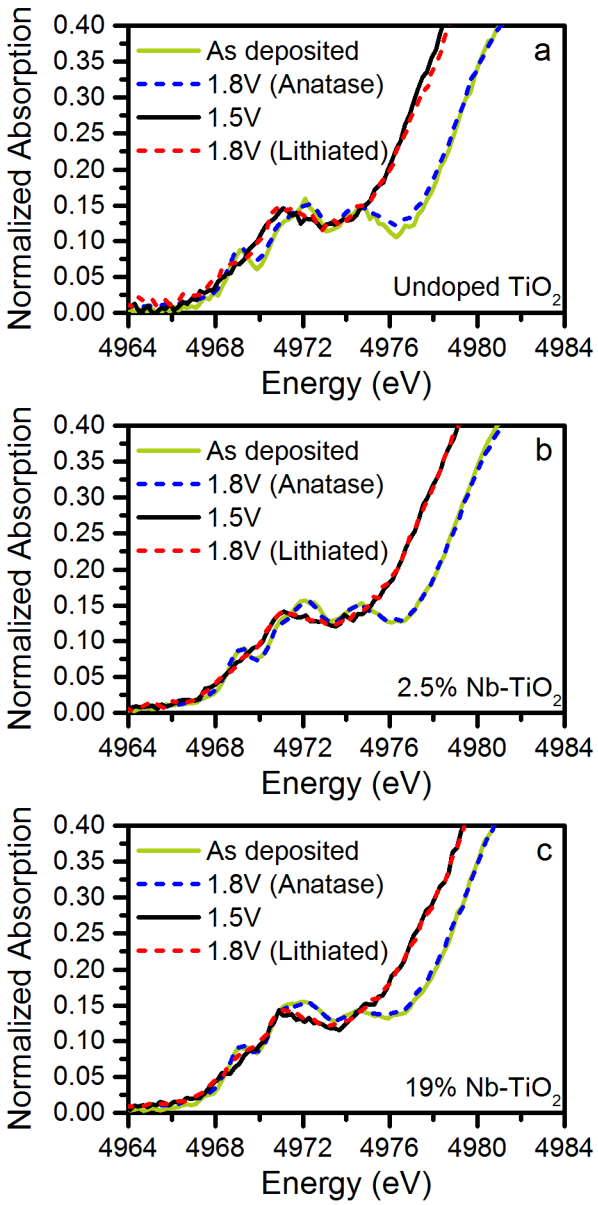

Figure 2.6: Titanium XANES pre-K edge spectra upon *ex situ* charging.

a) Undoped, b) 2.5% Nb-doped and c) 19% Nb-doped TiO_2 NCs.

Our XANES results indicate that capacitive charging populates delocalized conduction band states and that lithium insertion is required to induce localization. Thus, we predicted no visible electrochromism would occur in the absence of a small cation, such

as Li^+. Rather, we anticipate that only NIR LSPR modulation should be possible if a bulky, non-intercalating cation, such as tetrabutylammonium (TBA^+) is employed in the electrolyte. To test this hypothesis, the electrochromic response was measured by *in situ* spectroelectrochemistry using a non-intercalating 0.1M tetrabutylammonium-TFSI in tetraglyme electrolyte. The same film measured with Li-TFSI (**Figure 2.4**) was electrochemically cycled in the TBA^+ electrolyte, using a single silver wire as a counter and reference electrode. The potentials reported in **Figure 2.7** are referenced to Li/Li^+, based on a conversion from the Ag/Ag^+ reference used in the experiment. The film darkens in the NIR (**Figure 2.7**), however, charging in TBA^+ electrolyte does not induce a visible extinction at any potential, consistent with earlier results for undoped TiO_2[32,84], and reducing potentials beyond the lithiation threshold only increase the extent of NIR modulation. The TBA^+ ion is too large to intercalate into the anatase lattice, so we can confirm that capacitive electrochemical charging – whether in Li^+ or TBA^+ electrolyte – populates delocalized conduction band states, giving rise to increased NIR extinction.

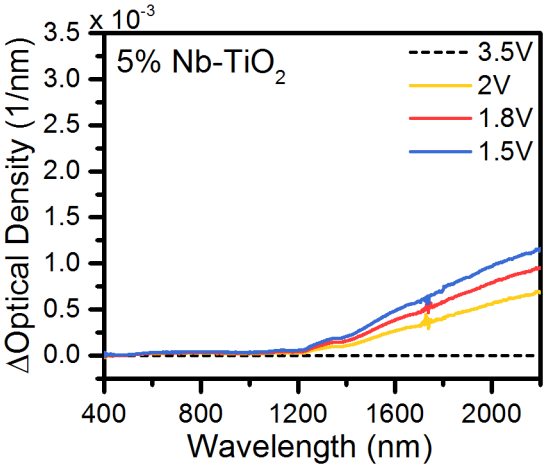

Figure 2.7: *In situ* spectroelectrochemistry of 5% Nb-doped TiO_2 NC film. The spectrum is reported as ΔOptical Density referenced to the as-deposited film extinction, and normalized by film thickness. The electrolyte was 0.1M TBA-TFSI in tetraglyme.

Furthermore, the continuous increase of a NIR extinction with applied bias is qualitatively consistent with the electrochromic behavior previously observed in plasmonic metal oxide NCs (ITO and AZO)[11,83,99]. The mid-IR electrochromic response of Nb-TiO_2 NCs was measured *ex situ* to observe the full optical response of the LSPR peak profile to capacitive charging (**Figure 2.8**). The films were charged in a Li-ion containing electrolyte but the potential was restricted to remain in the capacitive charging regime, avoiding the orthorhombic phase transition. Nb doping clearly increases MIR extinction of uncharged TiO_2 NC films, leading to well-defined peaks that are consistent with results ascribed to LSPR extinction in the previous study of Nb-TiO_2 NCs[11,82] (**Figure 2.8a**). Upon capacitive reduction, MIR extinction increases for all Nb doping levels (**Figures 2.8a and A8b**) and the peak wavelength decreases with increasing doping (**Figure 2.8b**).

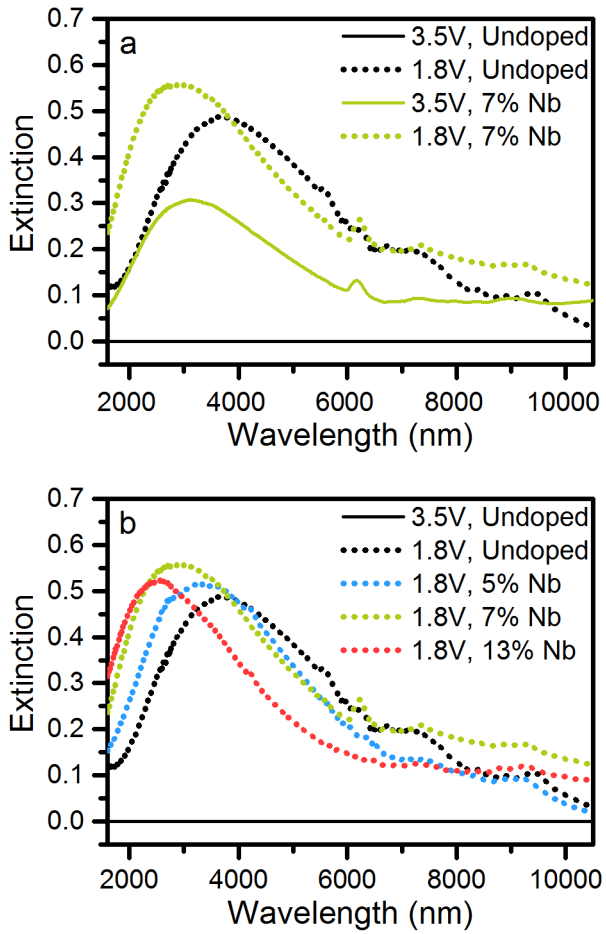

Figure 2.8: Transmission FTIR spectra of *ex situ* charged NC films. Spectra were referenced to the oxidized (3.5V) undoped TiO_2 film, and normalized by thickness. a) Comparison of oxidized (3.5V) and capacitively charged (1.8 V) films for a range of Nb doping content. b) Comparison of the capacitively charged (1.8 V) films for various doping levels.

Electrochromic effects in the visible and NIR bands occur by independent electrochemical charging processes: lithium intercalation leads to electron localization at Ti sites for the former, while population of conduction band states during capacitive charging leads to LSPR modulation for the latter. The independence of these two

electrochromic modes can be exploited further by modulating electrochemical capacitive charge of the lithium intercalated phase (~$Li_{0.5}TiO_2$) . At reducing potentials negative of the intercalation threshold, lithiated TiO_2 NCs accumulate charge by capacitance as demonstrated in the XANES and XRD results, leading to a modulation in the near-IR extinction of the $Li_{0.5}TiO_2$ phase as shown in **Figure 2.9**. The fully reduced film at 1.5V shows a maximum visible extinction and moderate NIR extinction, but upon re-oxidation to 1.8V the visible peak is retained while NIR extinction decreases significantly. This effect is consistent with free electron depletion upon capacitive oxidation, leading to a decrease in extinction of an LSPR peak. The independent switching of visible and NIR electrochromic modes in a single component inorganic material is unprecedented and holds the tantalizing promise that rich, multi-functional optical control devices can be achieved using simple processing strategies for a single-component NC film.

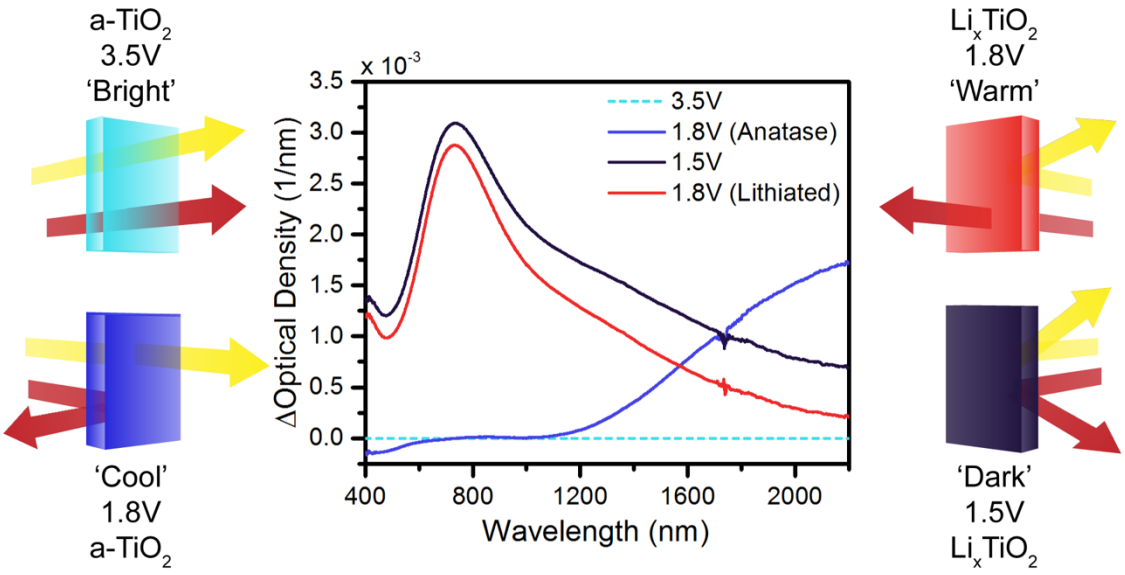

Figure 2.9: *In situ* spectroelectrochemistry of 5% Nb-doped TiO_2 NC films. Four distinct electrochromic states are shown with different transmittance of visible (yellow arrow) and infrared (red arrow) light. Spectra are reported as ΔOptical Density referenced to the as-deposited film extinction, and normalized by film thickness. The electrolyte was 0.1M LiTFSI in tetraglyme. The "cool" mode is accessed by reducing from the "bright" mode, while the "warm" mode is accessed by oxidizing from the "dark" mode.

CONCLUSIONS

Two modes of electrochromism – plasmonic and polaronic – co-exist in one material, Nb-TiO_2 NCs. Capacitive charging of TiO_2 NCs induces infrared extinction, which is tunable by doping. In this state, the charge carriers remain delocalized. This 'cool' infrared-blocking mode is well established for previous studies of plasmonic metal oxide NCs[11,83], but has not been well explored in TiO_2. In fact, even the delocalization of electrons in doped TiO_2 (e.g. Nb-TiO_2) is actively debated, but that theory is strongly supported by

our Ti K-edge XANES spectra. The electrons persist in delocalized states throughout the capacitive charging process. Only upon insertion of Li^+ ions, and transition to the orthorhombic $Li_{0.5}TiO_2$ phase, do the electrons localize, forming Ti^{3+} polaronic color centers with a characteristic visible extinction. The lithiated phase ('dark' mode) blocks infrared and visible light, but infrared extinction can be diminished by capacitive oxidation (a 'warm' mode). This kind of dual band modulation has long been a goal of electrochromics research, and was only recently demonstrated by combining plasmonic metal oxide NCs with an amorphous transition metal oxide, forming a composite of two single band electrochromic materials[85,109]. Our study demonstrates how dual mode electrochromic behavior can be achieved with a single-component solution-processed inorganic film.

More broadly, our results shed light on the nature of charge carriers in anatase TiO_2. We have presented broad evidence that plasmonic and polaronic excitation processes occur by discrete charging pathways. The interaction between conductivity, charging behavior and structure has implications on the performance of TiO_2 as an electrode material. Likewise, photocatalytic and photovoltaic applications of TiO_2 are also impacted by charge transport efficacy and stability issues, which can be mitigated by a careful understanding of surface and bulk charge localization in TiO_2[16,17,110-112]. The intersection of independent light-matter interactions – LSPR extinction and localized color centers – in colloidal TiO_2 NCs provides a novel means to decouple different optoelectronic processes in this important material.

Chapter 3: Electrochemical Modulation of Mid-IR Localized Surface Plasmon Resonance in Nb Doped Anatase TiO_2 Nanocrystals

ABSTRACT

Colloidal nanocrystals of anatase TiO_2 exhibit a localized surface plasmon resonance in the mid-infrared if the Fermi level is raised into the conduction band through carrier accumulation, either through synthetic doping or electrochemical reduction. The infrared resonant plasmonic absorption of dilute dispersions of Nb-doped TiO_2 was characterized by the Drude model and Mie approximation, yielding tunable plasmon resonance with Nb doping and comparable carrier damping to plasmonic metal oxide nanocrystals such as Sn-doped In_2O_3. Thin films of Nb-TiO_2 nanocrystals on infrared-transparent conductive substrates were electrochemically charged in a non-intercalating electrolyte, and the optical density of these films was observed to increase with inserted charge near the infrared plasmon absorption peak of nanocrystal solutions. A layer stack optical model was used to extract reliable Drude parameters for TiO_2 nanocrystals from *ex situ* infrared transmittance measurements at different states of electrochemical charging. Electrochemical charging was observed to induce greater variations in free carrier concentration than synthetic doping, and demonstrated different carrier damping behavior than the unbiased nanocrystals.

INTRODUCTION

Degenerately doped metal oxide nanocrystals have emerged as tunable plasmonic materials that can be integrated into a variety of optoelectronic applications. Metal oxide composition, defect equilibrium, nanocrystal geometry and induced charge can shift the material's localized surface plasmon resonance (LSPR) across the visible and infrared (IR)

spectrum[56]. A recent addition to the library of functional plasmonic metal oxides is nanocrystalline anatase TiO_2, a wide bandgap semiconductor often used with other functional light-absorbing metals, semiconductors or organic materials as a scaffold, sensitizer or charge separating medium[15]. Through colloidal synthesis methods, degenerate Nb-doped TiO_2 nanocrystals have been found to show LSPR in the IR, with peak energies of about 2000 - 3000 cm^{-1}, which can be tuned by varying the free electron concentration with different substitutional Nb dopant concentrations[82]. A similar LSPR modulation is induced in a mesoporous film of colloidal Nb-doped TiO_2 nanocrystals upon charging in an electrochemical cell[68,113]. Depending on applied potential and doping level, a reversible IR electrochromic coloration can be modulated. This electrochromic plasmonic effect has been demonstrated for functional applications in other semiconductor nanocrystal films such as doped indium oxide and zinc oxide nanocrystals[11].

The materials that exhibit LSPR in the infrared have smaller resonant energies than traditional noble metal plasmonics such as gold or silver. The Drude model describes the complex dielectric response of free carriers as a function of the plasma frequency, ω_p, and the scattering rate, Γ:

$$\varepsilon_D = 1 - \frac{\omega_p^2}{\omega^2 - i\omega\Gamma}$$

The plasma frequency is dependent on the free electron concentration, n_e, and conduction band effective mass in n-type semiconductors:

$$\omega_p = \sqrt{\frac{n_e e^2}{\varepsilon_0 m^*}}$$

At the dilute limit of conductive nanoparticles in an insulating medium, the resonant energy of an LSPR response scales with the plasma frequency following the Mie approximation [54,55]. The Mie approximation predicts that the LSPR absorption peak energy and amplitude will scale with the plasma frequency in the Drude model.

To absorb in the infrared, plasmonic semiconductors must have a much lower free carrier concentrations or higher effective mass than noble metal nanocrystals, which absorb in the visible spectrum. These infrared semiconductor plasmonic oxides have more polar, anisotropic crystal structures than noble metals, and introduce unique electronic interactions and non-idealities. For instance, compensating defects such as oxygen vacancies and localized trap states can intrinsically alter the carrier concentration in metal oxides, altering the optical and electronic behavior expected for an ideal metal[56]. Recent studies have probed the implications of semiconductor properties on LSPR in metal oxide nanocrystals, revealing the importance of the spatial distribution of substitutional dopants in nanocrystal particles[114] and crystalline anisotropy of the conducting lattice[115]. Despite the complications that semiconductor physics can create in controlling LSPR behavior in metal oxide nanocrystals, the optical response in these materials can probe underlying electronic properties and elucidate complex behavior in functional nanomaterials. Optical conductivity can act as an analytical surrogate of film conductivity for mesoporous materials that have large conduction barriers between particles, and the amplitude, energy and peak profile of the LSPR response can be used to characterize free carrier properties without a contacting electrical connection[115]. Schimpf *et al* have demonstrated a method to measure the free carrier concentration in doped ZnO nanocrystals in solution through the LSPR response, by optically photoexciting a dispersion of particles and chemically titrating in oxidants to remove electrons from the particles [99]. Similarly, the infrared optical response of nanocrystalline TiO_2 electrodes upon electrochemical charging has been used to characterize band alignment for photovoltaic and photocatalytic applications, albeit without considering the wealth of information that the LSPR peak profile can provide[50]. To this end, this article seeks to characterize the infrared LSPR response of anatase TiO_2 nanocrystals, both in a dilute dispersion and upon charging in a thin film electrode, to

measure the dependence of free carrier properties on synthetic and electrochemical variations.

EXPERIMENTAL SECTION

Nb-doped TiO_2 NCs were synthesized following the procedures of Dahlman *et al*. [68]. The wet chemical, surfactant mediated synthesis yielded monodisperse 10nm cuboid nanocrystals with Nb content controlled by the ratio of $NbCl_5$:$Ti(EtO)_4$ in the precursor solution. Nb doping content was calculated as the percentage of Ti sites occupied by Nb, and measured by inductively coupled plasma-optical emission spectroscopy. At high Nb doping content (> 10% Nb), the particles became more oblong and polydisperse in shape, so the synthesis was restricted to doping levels below this threshold.

FTIR transmission measurements were taken of 1 mg/mL dispersion of TiO_2 nanocrystals in tetrachloroethylene (TCE), with 0.01 vol.% oleic acid added to stabilize the colloid. Solution FTIR spectra were taken with a 1mm pathlength solution cell capped by KBr windows, and backgrounded to a solution cell filled with neat TCE.

Films of colloidal TiO_2 NCs were prepared by spin-coating thin films of 50 mg/mL oleic-acid capped nanocrystal dispersions in 1:1 hexane:octane solvent. Nanocrystals were coated onto an undoped Si substrate covered in a thin (~ 10 nm) thermally deposited layer of gold. The thin layer of gold provided sufficient electronic conductivity to electrochemically charge coated TiO_2 films, but weak enough optical reflectance to transmit a measurable amount of infrared light during FTIR measurements. The deposited TiO_2 films, ranging from 190 to 433 nm in thickness as measured by profilometry, were inherently insulating due to the organic ligands separating the nanocrystal particles. The

deposited TiO_2-Au-Si films were annealed at 300°C in air for 30 min to remove organic ligands and increase electronic conductivity between the particles.

For electrochemical testing, the TiO_2-Au-Si substrate was used as the working electrode, and a platinum foil and a fritted Ag/Ag^+ cell were used as the counter and reference electrodes, respectively. The substrate was charged inside an Argon glovebox in 0.1M tetrabutylammonium bis-trifluoromethanesulfonimidate (TBA-TFSI) salt dissolved in propylene carbonate and current was measured with a potentiostat. Air-free FTIR transmission measurements were recorded of charged TiO_2-Au-Si films by rinsing electrolyte from the charged films with dimethyl carbonate and placing the dry film in an O-ring sealed air-free cell capped by the Si substrate on one end and a 2 mm ZnSe window on the other end, with a sealed pathlength of about 1 cm. FTIR transmission spectra were baselined to the transmittance of the ZnSe window and holder without a substrate.

The optical transmission of charged layer stacks was fitted using the Scout software package (www.wtheiss.com).

DISCUSSION

Despite the ubiquity of nanocrystalline anatase TiO_2 in diverse optical and electronic applications, the mid-IR LSPR response of degenerate TiO_2 nanocrystals has not been thoroughly characterized in the literature. De Trizio *et al* reported on the LSPR absorption of Nb-doped TiO_2 nanocrystals by FTIR spectroscopy of deposited films in an ATR geometry, while Dahlman *et al* recorded the mid-IR transmittance of thin films [68,82]. At the large particle concentrations of nanocrystal films, the optical absorption feature is convoluted by effective medium interactions, dipole-dipole coupling between plasmonic particles or damping due to film conductivity effects [58,116].

The LSPR response of independent TiO_2 nanocrystals at the dilute limit was measured by dispersing nanocrystals in a TCE solvent at concentrations below 1 mg/mL, and measuring FTIR transmittance through a solution cell. **Figure 3.1a** shows the absorption spectra of varying Nb doping contents for 1 mg/mL TiO_2 solutions. A clear Lorentzian peak is observed around 3000 cm^{-1} for highly Nb-doped nanocrystals corresponding to an LSPR absorption, as well as strong absorption due to the oleic acid C-H stretch (2900 cm cm^{-1}) and O-H stretch (3300 cm^{-1}). The LSPR peak was fitted to a Drude model of free carrier transport assuming constant damping, Γ and the Mie approximation of confinement in nanocrystals. The high energy dielectric constant of TiO_2 was set as 5.6 [117], the dielectric constant of TCE was set as 2.3 [118] and the path length of the solution cell was measured as 1 mm. The volume fraction, plasma frequency, damping and a correction term for the O-H stretch were fitted to the solution spectra in **Figure 3.1a**, yielding the Drude parameters presented in **Figure 3.1b**.

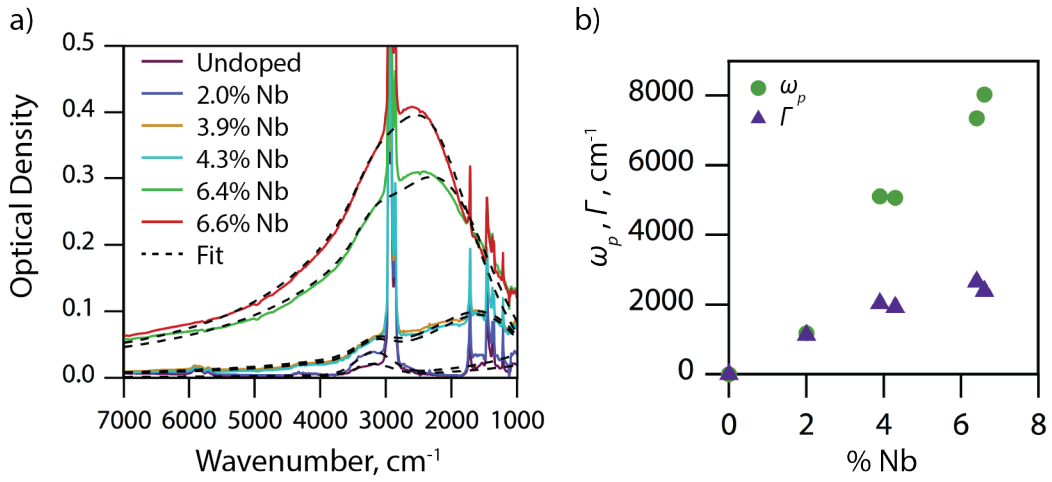

Figure 3.1: Solution FTIR spectra of TiO_2 dispersions.

a) Optical density measured by transmission-mode FTIR of 1 mg/mL solutions of oleic-acid capped TiO_2 nanocrystals dispersed in TCE. b) Drude parameters for TiO_2 extracted from fits of the FTIR spectra shown in a).

The plasma frequency varies monotonically from non-measurable values for undoped TiO_2 to about 8000 cm^{-1} for 6.6% Nb-doped TiO_2. These values can be compared to the Drude response of tin-doped indium oxide (ITO), which is frequently used as a benchmark for wide band-gap conductivity in degenerate anatase TiO_2 [119]. At similar substitional doping content, ITO nanocrystals show Drude plasma frequencies of 11000 to 16000 cm^{-1} and low frequency damping ranging from 1000 to 8000 cm^{-1} [114]. Nb-doped TiO_2 nanocrystals show significantly lower plasma frequencies, corresponding to a weaker red-shifted LSPR peak. The Drude damping constant matches the low limit of ITO, implying that optical mobility in the conduction band is consistent between these two materials. Considering the similar transport-limiting conduction band electron effective mass of 0.4 m_e for both materials [24,114], the difference in plasma frequency may indicate inefficient Nb

dopant activation, electron trapping behavior, heterogeneous ensemble effects or inefficient optical absorption due to the anisotropic transport properties in anatase TiO_2.

The carrier concentration in TiO_2 can be modulated by charging as well as substitutional doping[68,113]. Multiple approaches have been demonstrated to observe the modulation of LSPR in the infrared in charged colloidal metal oxide nanocrystals, including UV photodoping of dispersed nanocrystals in solution[99]. However, this method requires a stable colloidal dispersion that does not precipitate upon changes in nanocrystal surface charge during photocharging. Furthermore, the optical response of photodoped nanocrystals may not capture the same charging behavior observed in functional electrochromic thin film devices. Mendelsberg *et al* demonstrated a method to extract the Drude carrier properties from the transmittance of a mesoporous film of ITO nanocrystals using a multi-layer stack optical model and assuming a Maxwell-Garnet effective medium approximation[116]. A layer stack simulation can be used to extract the carrier properties within charged metal oxide nanocrystal films from optical transmission measurements. This approach allows for the correlation of optical properties with electrochemical measurements, and simulates the charging behavior shown in functional applications such as electrochromic smart windows. However, an *in situ* measurement of TiO_2 in a full electrochromic cell [113] is difficult to resolve in the mid-IR range of the LSPR peak because of losses due to electrolyte absorption, substrate reflectivity and phonon responses. Instead, an air-free *ex situ* measurement technique was developed to accurately probe the LSPR in charged TiO_2 NC films within a simpler, more IR-transparent layer stack.

A moderately IR-transparent, conductive substrate was created by thermally depositing 10 nm of Au onto an undoped, double-sided polished silicon substrate. At this gold thickness, the films are about 10% transmissive in the infrared, with decreasing transparency at lower energies. Infrared transparency and substrate conductivity for

electrochemical charging are competing goals, because a conductive substrate will reflect infrared light according to the Drude model. 10 nm was the thinnest coating that could be achieved without dramatic decreases in film durability and conductivity, due to islanding effects that fragment percolation across the substrate [120]. The gold film was observed to increase in IR transmittance after heating at the film annealing temperature, suggesting that film processing decreases substrate conductivity. Nonetheless, the 10 nm Au-Si substrate was sufficiently conductive to deliver an electrochemical charge to the TiO_2 layer.

Films of TiO_2 NCs on ITO-Si were electrochemically charged using a non-intercalating electrolyte (TBA-TFSI in propylene carbonate) to avoid phase transformation and electron trapping caused by cation insertion. TBA is a bulky, non-intercalating cation that can only compensate electrochemical charge by surface capacitance. Thus, the as-deposited TiO_2 anatase phase is retained across all charging potentials [68]. Other electrolyte solvents, such as tetraglyme, were found to delaminate the NC films from the substrates during charging. The films were charged at a negative bias of -2V vs Ag/Ag^+ for two minutes, and then allowed to relax under open circuit conditions for an additional two minutes to equilibrate polarization across the film. The films were then removed from the electrolyte and rinsed with dimethyl carbonate, before being assembled into an air-free cell to measure FTIR transmittance. During a charging experiment, the films were first oxidized completely, and then repeatedly charged through the charging cycle to access a range of charge states in the film. The total accumulated charge was measured by summing the total charge across all previous potentiostatic charging steps, while subtracting a constant background leakage current of about 100 nA / cm^2. In this geometry, the reducing charge is expected to be compensated by adsorbed counter-ions at the nanocrystal interface and across electrolyte polarizations in solution, along with any pseudo-capacitive surface reactions with the electrolyte[121]. FTIR transmission spectra three different TiO_2 nanocrystal

films of different Nb doping content are shown in **Figure 3.2** during step-wise *ex situ* charging at -2V.

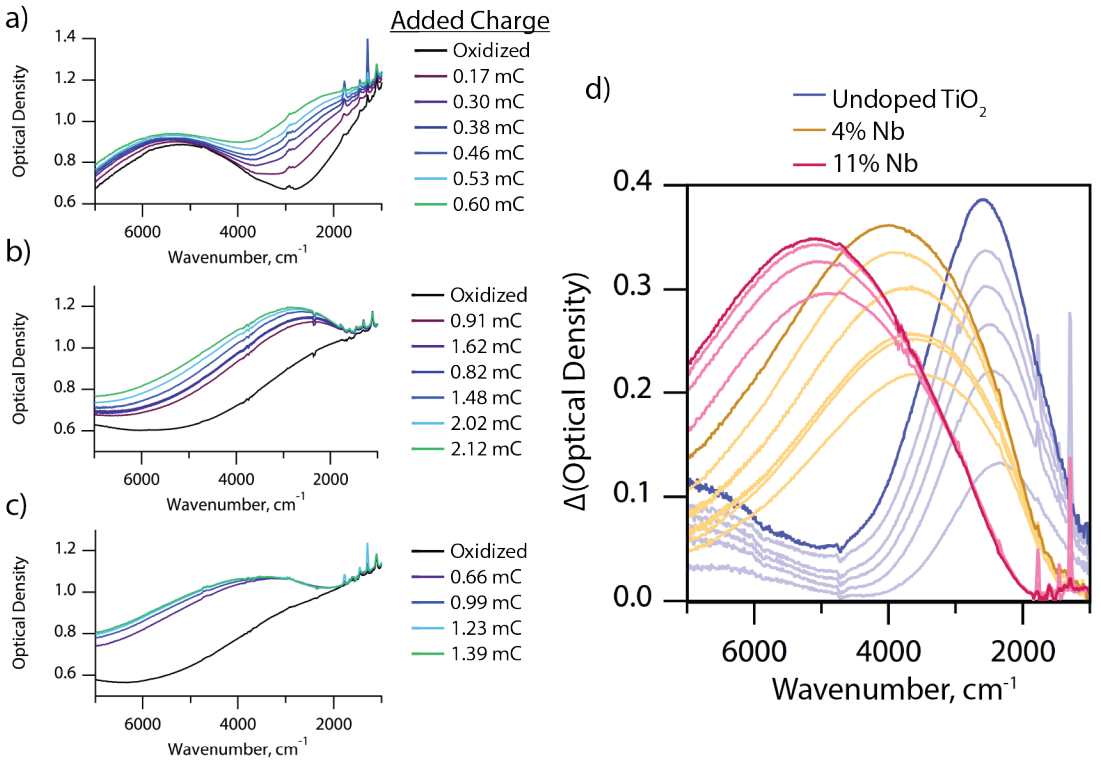

Figure 3.2: Transmission FTIR spectra of TiO_2 NC films.

NC films on Au-coated undoped Si substrates mounted in a ZnSe-sealed cell charged to -2V vs. Ag+, taken at sequential 2 min intervals of charging, for a) 433nm thick undoped TiO_2, b) 245 nm thick 4% Nb-doped TiO_2 and c) 190 nm thick 11% Nb-doped TiO_2 films. d) Differential optical density plots of each nanocrystal film baselined to the oxidized spectra of each film.

Each nanocrystal film clearly shows a monotonic increase in optical density with charging steps, indicating that charge can accumulate across sequential steps. The films shown in **Figure 3.2** represent a diversity of film thickness and Nb doping, spanning 190

– 433 nm thick and 0% - 11% Nb doping. These variations lead to clear qualitiative variations in the absolute transmission profile of the TiO_2 film as well as the differential change in optical density during charging (**Figure 3.2d**). To gain a more quantitative understanding of these optical responses, the Scout software package was used simulate the optical transmittance of a multi-layer stack from first-principles materials properties and layer geometries. Transmission spectra were simulated by an iterative method to deconvolute the response of the substrate, mesoporous film and intrinsic nanocrystal dispersion, as shown in **Figure 3.3**. The Drude carrier properties of the nanocrystal inclusions were guessed and constrained using the calculated solution-spectra Drude fits from **Figure 3.1**, but with larger maximums in damping and plasma frequency to account for charging and the large range of Nb content. The effective mass and high-frequency dielectric constant were taken from the literature as described previously. Next, an effective medium approximation was assembled from the TiO_2 inclusions and a fitted value for the host matrix dielectric constant, using a Maxwell Garnet approximation for spherical conducting inclusions in an encompassing insulating matrix. Mendelsberg *et al* demonstrated that the volume fraction and host dielectric constant are linearly correlated in fits of optical transmittance, so a volume fraction of 0.60 was assumed for these films and the host dielectric constant was fit to optical spectra. Mendelsberg *et al* observed a volume fraction of 0.60 for 5 nm ITO nanocrystal films annealed in air under similar conditions, so this value was used as a reasonable starting point [116]. In fact, the goodness of fit trended towards a minimum at values between about 0.65 and 0.5 for all nanocrystal films. However, a more accurate volume fraction could be measured directly through techniques such as ellipsometric porosimetry, analysis of electron microscopy images, or high energy scattering and absorption studies with X-rays or other radiation. The optical response of the substrate was modeled independently by fitting the transmittance of an

uncoated Au-Si substrate to extract thickness and Drude parameters for the metallic coating. A similar technique could be applied to refine the volume fraction, host dielectric, thickness and Drude properties of a TiO_2 film by measuring its transmittance on a bare undoped Si substrate and on a conductive Au-coated Si substrate. Thicknesses can be measured directly by profilometry (for the nanocrystal film) or atomic force microscopy (for the Au-coating). Combining these fitted, assumed and constrained parameters for the FTIR spectrum of a layer stack yields a full simulation of the optical transmittance of the film, as shown in **Figure 3.3**. The free variables in this fit include the Drude plasma frequency and damping constant for TiO_2, the host dielectric constant of the matrix, the Drude damping constant of the Au layer (independently modified during film processing for each sample), and a minor static loss term due to roughness, which scales the absorption linearly by a constant factor C_1. Otherwise, all variables were either constrained by other experiments or assumed from literature values.

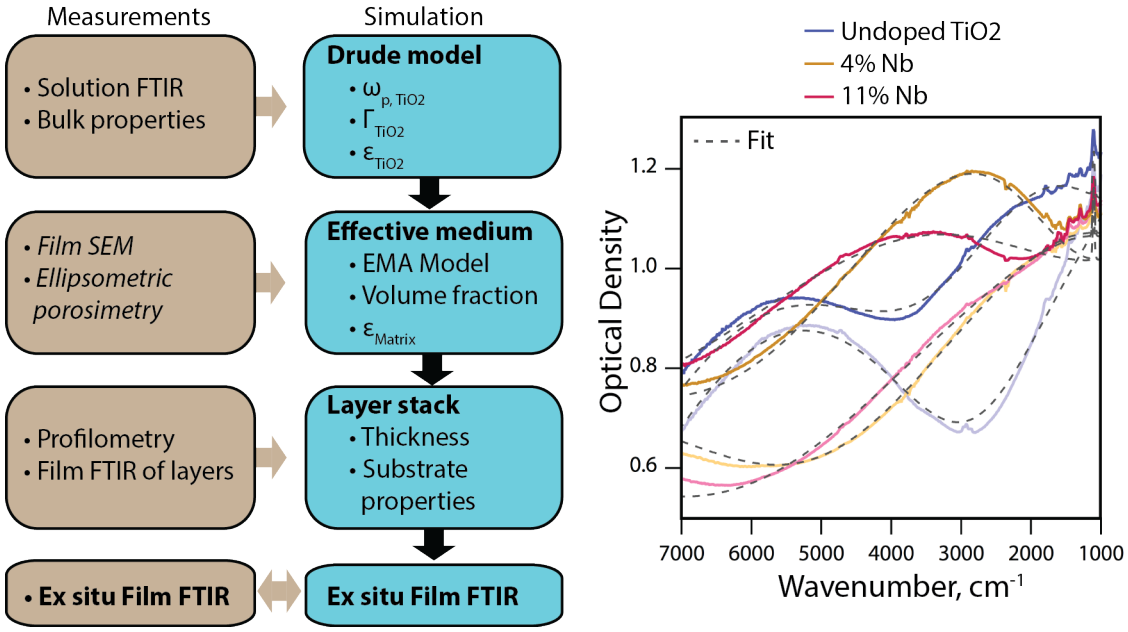

Figure 3.3 Layer stack optical transmittance fitting scheme of charged NC films. A schematic showing the iterative fitting procedure used to combine assumed, constrained and fitted parameters in a Scout simulation of optical transmission data, illustrating the relationship between measured and fitted parameters. The results of this procedure for a simultaneous fit of oxidized and charged films of undoped, 4% Nb-doped and 11% Nb-doped TiO_2 nanocrystals are shown, using data presented in **Figure 3.2**. Solid lines are experimental data and dashed lines are spectra simulated in SCOUT.

Parameters that should be similar among all samples (nanocrystal volume fraction, host dielectric constant, roughness loss) were simultaneously fit for charged and unbiased samples of three different nanocrystal films (**Figure 3.3**). All films show decent fits to the layer stack optical simulations across a wide infrared spectrum for both reduced and oxidized samples, with deviations at the low and high energy extremes of the spectra. The

results of these fits are shown in **Table 3.1**, with information on the sources of the obtained values.

Parameter	**Value**	**Source**
TiO_2 ω_p	2100 - 14000 cm^{-1}	Constrained fit
TiO_2 Γ	1000 - 6000 cm^{-1}	Constrained fit
TiO_2 bulk dielectric, ε_∞	5.6	Ref [117]
Nanocrystal volume fraction	0.6	Ass'd from Ref[116]
Host matrix dielectric, ε_{Matrix}	2.15	Constrained fit
TiO_2 layer thickness	190 – 433 nm	Profilometry
Surface roughness, C_1	0.92	Constrained fit
Si layer thickness	0.5 mm	Manufacturer specs.
Si layer dielectric constant	11.7	Ref [118]
Au layer thickness	13 nm	Constrained fit of Au-Si only
Au ω_p	60000 cm^{-1}	Constrained fit of Au-Si only
Au Γ	3000 - 5000 cm^{-1}	Constrained fit

Table 3.1: Fitting results of a Scout layer stack simulation.
Simultaneous fits of the infrared transmittance of unbiased and charged samples of undoped, 4% Nb doped and 11% Nb doped TiO_2 nanocrystal films on Au-coated Si substrates, using the Scout software package. Values that display a range of results were fit independently for each film.

The accuracy of the fitted parameters depends on the tolerance of these extracted parameters to the multiple free variables in the fitting routine. Mendelsberg *et al* found that

volume fraction and the host dielectric constant are linearly correlated[116], and fits of mesoporous ITO nanocrystal films also showed large deviations in thickness and nanocrystal ω_p , Γ ε_∞. The fits of the complete layer stack transmittance also show significant errors from the data as shown in **Figure 3.3**. However, a more robust analysis can be performed by studying the differential optical response (ΔOD) of each film (**Figure 3.2d**). The ΔOD differential upon charging should be dominated by changes in the Drude parameters in the TiO_2 nanocrystals, and should therefore be less sensitive to optical properties in the rest of the layer stack. To simulate the ΔOD of each film, absolute fits of the unbiased films were taken as a baseline reference (**Figure 3.3**). Simulated spectra were then produced with equivalent parameters as the unbiased baseline fit, but with controlled variations across a range of charge states measured by ω_p. The ΔOD peak was then characterized by its maximum height and energy, as shown in **Figure 3.2d**. Keeping all other variables constant, minor changes in either the TiO_2 or host matrix static dielectric constants, ε_∞ and ε_{Matrix} only shifted the ΔOD peak height and energy by a few percent, and were found to only contribute a minor error to the extracted parameters. A similar insensitivity was observed for the damping constant of the gold substrate. Other variables, particularly the volume fraction, introduced large distortions in the measurement of nanocrystal Drude parameters as a function of charge state (ω_p), and should be expected to distort the absolute values produced by these fits. Nonetheless, these simulated differential charging spectra can be used to confirm the sensitivity of this method to the two parameters of most concern in this study of the carrier properties in TiO_2 nanocrystals: TiO_2 ω_p and Γ.

The TiO_2 Drude parameters fitted by the Scout layer stack model describe fundamental properties of band-like carrier transport in the nanocrystals. The plasma frequency is directly related to the free carrier concentration, while the damping constant

relates to the electron mobility. Both factors are also dependent on the electron effective mass. It is important to distinguish the sensitivity and independence of each of these parameters to the layer stack fitting routine to assess the reliability of these extracted parameters. Simulated FTIR spectra were produced with identical parameters as each unbiased nanocrystal film sample, but with a range of ω_p and Γ values. The change in the optical spectrum from the fitted unbiased sample, ΔOD, was then recorded and the height and energy of the resulting LSPR-like peak was measured. **Figure 3.4** displays the simulated and fitted ΔOD peak heights and energies across the range of values accessed in these experiments. Measured ΔOD peak maxima and energies from the experimental data are also plotted for reference. Despite the Scout fitting routine's insensitivity to the ΔOD peak amplitude and location, the fitted results track the experimental ΔOD features quite closely. Furthermore, the peak amplitudes and energies obtained by the fits lie within the extreme bounds defined by the simulations at all charging levels. Most importantly, the plots of ΔOD peak maxima vs. plasma frequency in **Figure 3.4** reveal that the ΔOD peak amplitude limits the possible plasma frequency to a narrow window within the range of damping constants accessible to the system. Even without a complete fit of the absolute transmittance of the layer stack, the measured ΔOD peak amplitudes and energies alone could be used to make a reasonable guess of the plasma frequency and damping constant in a charged nanocrystal film. Ultimately the precision of this measurement depends on *a priori* knowledge of the invariant film parameters - volume fraction, thickness, host dielectric and substrate properties – to provide a reliable measurement of nanocrystal Drude parameters.

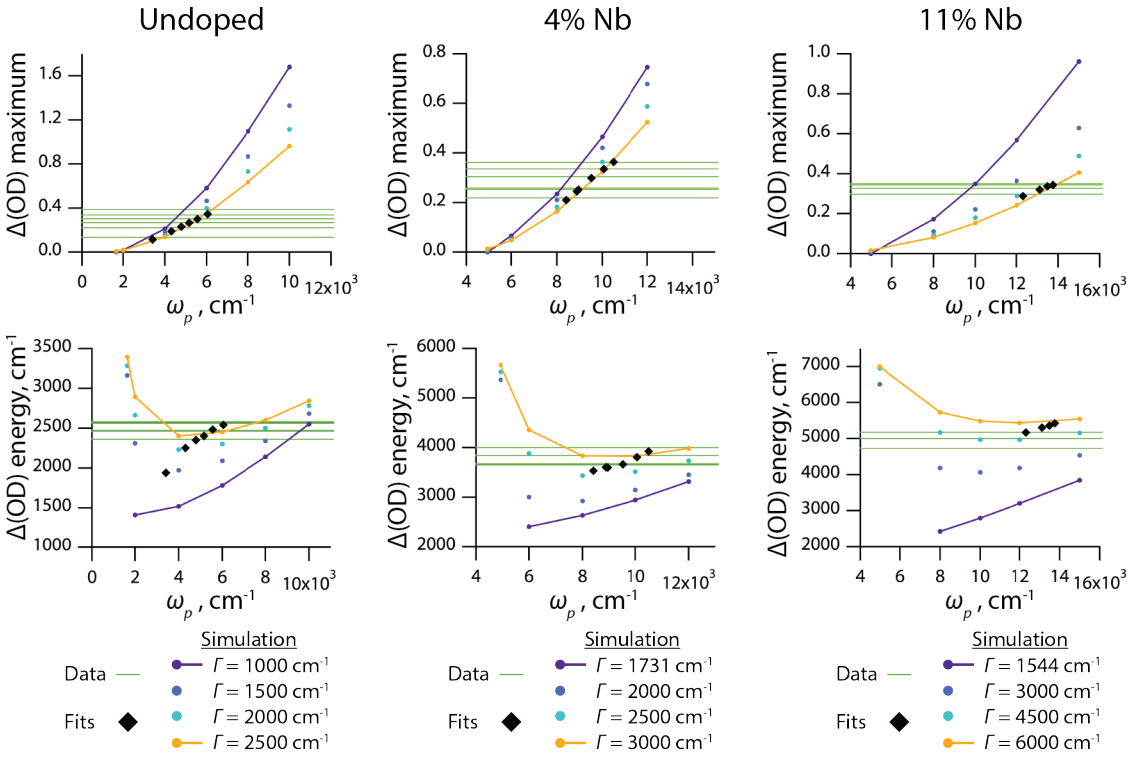

Figure 3.4: Measured, simulated and fitted ΔOD peak height and energy in TiO_2

Comparison of the ΔOD peak height and peak maximum energy between measured, fitted and simulated spectra across charging tests for undoped, 4% Nb-doped and 11% Nb-doped TiO_2 nanocrystal films. The horizontal green lines indicate measured ΔOD peak height and energy.

Drude parameters obtained from Scout fits of the absolute layer stack transmittance were compared to electrochemically inserted charge to test the efficiency of the electrochemical modulation. A 'total' carrier concentration was defined by adding the accumulated charge from electrochemical modulation to the carrier concentration extracted from a Drude fit of the unbiased nanocrystal film. The accumulated electrochemical charge was related to the carrier concentration by the constrained volume fraction and measured film volume. **Figure 3.5a** shows that the carrier concentration measured by the plasma

frequency increases almost linearly with the total accumulated charge, as would be expected from free electron accumulation. However, there are dramatic differences between the three different nanocrystal samples. Fitted results from the 11% Nb doped film imply that the Drude-fitted carrier concentration exceeds the amount of carriers inserted during charging, which is inconsistent with a band-like model of electron accumulation. This result suggests that either the plasma frequency is overestimated during the fitting routine or the electrochemical charge is underestimated. Regardless, the qualitative trends from this plot reveal that the Nb-doped nanocrystals can accumulate much more charge than the undoped films. Nb-doped films may have higher inherent electronic conductivity and may charge more efficiently than the undoped sample during the experiment.

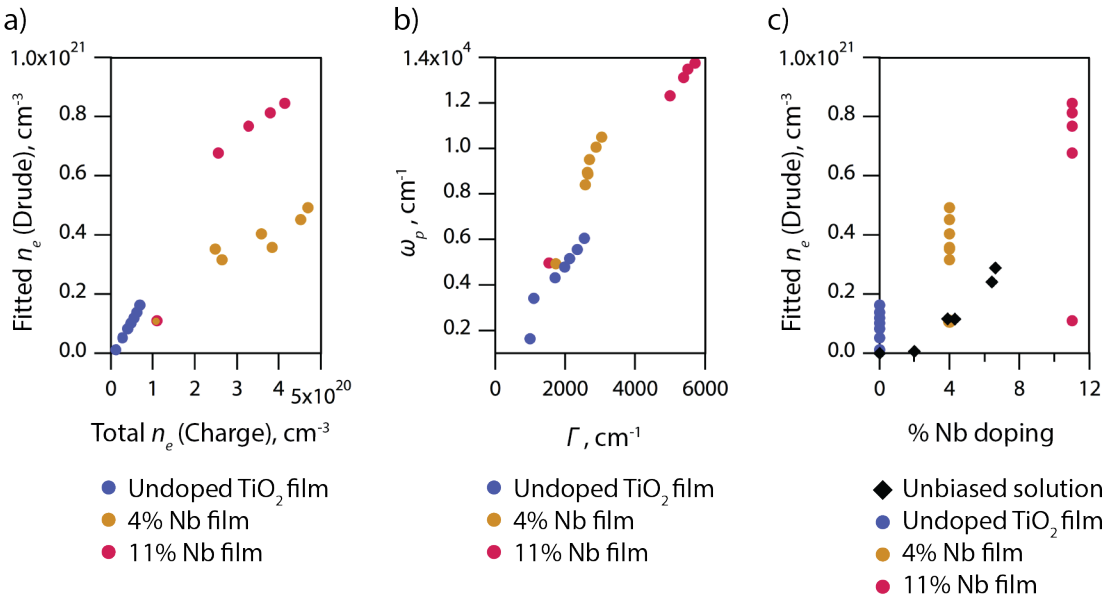

Figure 3.5 Carrier properties extracted from Drude Scout fits.

a) A comparison of the fitted Drude free carrier concentration and total accumulated charge in nanocrystal films during charging. b) A plot showing the correlation between the Drude fitted plasma frequency and damping constant during electrochemical charging. c) A comparison of the fitted Drude free carrier concentrations measured for *ex situ* charged TiO_2 films and dilute solution spectra of TiO_2 dispersions for a range of Nb doping.

A plot of the plasma frequency vs. the damping constant (**Figure 3.5b**) reveals a strong linear correlation between these extracted parameters. This result is different from the trends measured by solution spectra in **Figure 3.1b**, which showed divergence between the fitted plasma frequency and damping constant at higher Nb doping. The correlation between ω_p and Γ in the films may indicate the dominance of nanocrystal-nanocrystal coupling or interparticle electronic transport on the observed LSPR damping in dense nanocrystal films. **Figure 3.5c** compares the Drude fitted plasma frequency for

electrochemically charged films and colloidal solutions across a range of Nb doping. The overlap of the fitted plasma frequencies from the 4% Nb doped TiO_2 solution and unbiased 4% Nb doped TiO_2 film provides strong evidence of the reliability of these methods to extract intrinsic material-specific carrier properties. It is also evident that electrochemical charging can induce greater changes in carrier concentration than synthetic doping alone, although the magnitudes of these modulations are within the same order of magnitude across the doping and charging regimes of this study.

CONCLUSIONS

These results indicate the dynamic tunability of carrier properties in plasmonic TiO_2 nanocrystals by synthetic Nb doping and electrochemical reduction, and suggest the potential to increase the modulation range by exploring new synthesis and charging schemes. Solution spectra of Nb doped TiO_2 dispersions reveal that free carriers in these nanocrystals have similar carrier damping and mobility to highly conductive metal oxides such as ITO, but that they have anomalously low carrier concentrations considering the degree of Nb doping. This result raises further questions about the efficiency of Nb dopant activation during synthesis, or inefficiencies in the optical absorption of anatase TiO_2 particles due to effects such as particle heterogeneity or anisotropy in the crystal lattice. Synthetic doping is found to show a smaller, though similar order of magnitude, effect on carrier concentrations as electrochemical charging by extracting Drude parameters from fitted layer stack FTIR transmittance of *ex situ* charged TiO_2 films. This method provides a robust measurement of plasma frequency and damping in films of degenerate semiconductor nanocrystals by showing a high sensitivity in changes in film absorption during charging. The extracted carrier properties reveal a linear dependence between

damping and carrier concentration in charged films, unlike the behavior found in solutions of unbiased nanocrystals, implying that film effects dominate carrier damping in this experiment. Despite uncertainties in fitting parameters and a simplistic fitting routine, the analysis of LSPR optical behavior in doped and electrochemically charged TiO_2 films offers a rewarding probe of electronic properties in this material. Further refinement of the layer stack optical model, as well as experimental techniques to narrow the constraints on free parameters, can increase the precision of these measurements. Moreover, a more comprehensive measurement of accumulated charge can refine the estimates of total carrier concentration during the charging experiments, and yield more reliable conclusions about dopant activation, carrier distributions and optical polarization in these films.

Chapter 4: Lithium Intercalation Dynamics in Titanium Dioxide Nanocrystals Probed by *In Situ* Optical Spectroscopy

ABSTRACT

Nanocrystalline anatase TiO_2 electrodes are promising anode materials that show robust cyclability and high specific energy and power for Li-ion battery applications. A surfactant-mediated wet chemical synthesis yields monodisperse sub-stoichiometric TiO_2 nanocrystals that vary between 20 nm truncated bipyramids and different sized nanoplatets by varying co-surfactant ratios. The size and shape dependence of the Li intercalation reaction in thin film electrodes of size-controlled nanocrystal films is studied by potentiostatic titration measurements and *in situ* optical measurements across the lithium intercalation threshold. Nanocrystal shape is found to influence lithiation potentials, and a distribution of transformation potentials is observed for all nanocrystal ensemble films. Time-resolved kinetic measurements of charging across the lithiation threshold are fit to a JMA model of nucleation and growth, and reveal that the active population of transforming nanocrystals in an electrode film varies with overpotential near the intercalation threshold.

INTRODUCTION

The storage of electrical charge is a fundamental challenge for the viability of alternative energy technologies and infrastructure. Li-ion batteries have emerged in the last several decades as a reliable platform for mobile charge storage in electronics, vehicles and even grid-scale applications, although they are beset by design challenges of electrochemical stability, cycle life and the balance between energy and power density [122]. Insertion electrodes such as transition metal oxides and phosphates, are commonly used as optimal technologies for these engineering trade-offs, because the interstitial and planar

voids of these structures can accommodate large densities of lithium ions without significantly perturbing the host structure of the electrode. However, these insertion materials are typically poor electronic and ionic conductors, and clever composite structures must be relied upon to wire the bulk electrode with conductive binders and porous electrolyte diffusion pathways.

The competing targets of improving capacity and charging kinetics have spurred the development of highly interfacial electrodes with mesostructure at the micrometer and nanometer scales to increase microscopic surface area to improve electron and ion diffusion rates, and allow for crystalline strain relaxation without damaging the integrity of the bulk electrode.. Nanostructuring has been employed to improve specific energy and power in next-generation Li-ion insertion electrodes including TiO_2 and $Li_4Ti_5O_{12}$ anode materials and $LiFePO_4$ and $LiMn_2O_4$ cathode materials. Nanostructured electrodes promise to relax some of the design limitations for high energy and power density Li-ion batteries, but they can also present unique challenges, such as processing difficulties, film delamination during use and a larger area for surface reactions with the electrolyte.

TiO_2, including the polymorphs rutile, brookite and anatase, has been well-studied as a Li-ion insertion anode with competitive charge storage density, high structural and chemical stability, and versatile, low cost synthetic pathways. At sizes below about 100 nm, the anatase structure is typically observed due to the allotrope's minimum surface energy. Anatase is a promising electrode material because of the high electron mobility of its conduction band[26] and the open interstitial voids that can reversibly accommodate about 0.5 Li ions per Ti atom at moderate electrode potentials through a first order phase transition[92]. Further reduction can induce a secondary transition to Li_1TiO_2, but this transition occurs more slowly than the initial lithiation process and faces practical cyclability issues[66,123]. 0-dimensional anatase TiO_2 nanocrystals, which have the smallest

possible grain size and maximum intefacial density, have been synthesized into a wide range of sizes and shapes by various techniques, and these different nanoscale geometries have yielded dramatically different electrochemical properties[18]. Distributions in nanocrystal sizes[62] and shapes[67] are also predicted to influence bulk charging behavior in nanocrystal electrodes. Variations in the precise faceting of nanocrystal TiO_2 grains has recently been found to influence electrochemical charging in Na-ion electrolytes[124], suggesting the role of facet geometry on charging behavior as well.

Investigations of the Li-ion insertion reaction in anatase TiO_2 are complicated by multiple charge compensation mechanisms in mesoporous electrodes. The Li-ion insertion reaction contributes a faradaic charge capacity that scales with the volume of TiO_2 in the electrode, but at nanoscale grain sizes non-faradaic capacitive and pseudo-capacitive responses can account for as much as half of the total capacity[74]. Thus, electrochemical measurements alone may not be able to distinguish the Li insertion reaction. Instead, direct *in situ* observations of lithium insertion in anatase TiO_2 nanocrystal electrodes have been made using transmission electron microscopy[125], X-ray absorption spectroscopy[106], X-ray diffraction[126] and optical spectroscopy[95]. These techniques have revealed that nanocrystal size changes the phase transition behavior of anatase TiO_2 grains, such that particles smaller than about 40 nm cannot support a stable coexistence of the anatase and lithiated phase during charging[75,125]. However, these studies rely on approximations of nanocrystal size, shape and polydispersity in ensemble films to relate nanocrystal transformations with bulk electrode properties.

The present work seeks to bridge the gap between the theoretical understanding of phase transformations in individual TiO_2 grains and macroscopic charging behavior at the ensemble device level. Surfactant mediated colloidal synthetic methods have enabled precise control over anatase TiO_2 nanocrystal size, shape and polydispersity[20,21]. Synthetic

control over TiO_2 particle size, shape and faceting is used to isolate these variables during *in situ* charging experiments, to correlate macroscopic charging behavior with particle geometry. *In situ* spectroelectrochemical measurements are then used to monitor Li insertion in TiO_2 electrodes, providing an *in situ* size and shape controlled observation of lithium intercalation in a nanocrystalline electrode.

EXPERIMENTAL SECTION

The colloidal synthesis of anatase TiO_2 nanocrystals was adapted from the wet chemical procedure developed by Gordon *et al*[127]. A solvent growth solution was prepared with 1.5 mmol oleic acid in 10 mL of octadecene, along with 30 mmol of either oleylamine (OLAM) or oleyl alcohol (OLAL) cosurfactant. The OLAM:OLAL ratio was varied to tune the particle size and shape. The solvent solution was degassed under a nitrogen atmosphere at 120°C for an hour prior to precursor seed injection. A precursor solution was prepared in a nitrogen glovebox by mixing 2 mmol of finely-ground TiF_4 powder and 10 mmol of oleic acid in 6.5 mL of octadecene solvent, and stirring at 80°C for an hour prior to the reaction. After precursor heating and solvent solution degassing, 1.5mL of the precursor solution was injected into the solvent flask at 60°C under nitrogen. This seed solution was heated and held at 290°C for 10 min. 7 mL of the remaining precursor solution was then injected into the growth solution at a continuous rate of 0.3 mL/min with a syringe pump while the growth solution was held under nitrogen at 290°C. After injection, the reaction was cooled to room temperature, yielding a blue solution. The nanocrystal solution was washed with repeated precipitation by isopropanol and redispersion in 1% OLAM/Toluene, and final redispersion in 6 mL of 1% OAc/hexane. To ensure particle size homogeneity, the final solution was centrifuged and the supernatant was filtered through a

0.2μm PTFE syringe filter to remove agglomerates and over-sized particles from the stable dispersions.

Thin electrode films of TiO_2 nanocrystals were prepared by spin-coating 50 mg/mL solutions of TiO_2 nanocrystals in a 1% oleic acid, 1:1 hexane:octane solvent onto ITO-coated glass substrates. The insulating oleic acid ligands on the NC surface were exchanged with formate ions by mass action by immersing the films in 0.1M formic acid in acetonitrile solutions for 30 min. To avoid sintering between the nanocrystals, the films were never exposed to temperatures above 100°C after deposition. The resulting films were 200-300 nm thick, as measured by profilometry.

Electrochemical testing was carried out using two-electrode geometry, with the TiO_2-coated film as working electrode and a lithium foil as counter and reference electrode. A 0.1M LiTFSI in tetraglyme electrolyte was used for all tests. The electrolyte was regularly replaced to avoid variations due to electrolyte break-down during prolonged experiments. *In situ* transmission Vis-NIR spectra were recorded during electrochemical measurements though a quartz cuvette cell with a fiber-optic coupled spectrometer. Strong absorption from the electrolyte limited the transmission spectral range from 400-2200 nm.

DISCUSSION

The minimum energy configuration of anatase TiO_2 is a square bipyramidal structure with exposed {101} facets, as predicted by a Wulff construction of measured and predicted surface energies [128]. However, in a colloidal nucleation and growth synthesis, metastable particle shapes can form by tuning the kinetic growth rates at each facet[20,21,124,129]. Strong binding of fluoride produced during the decomposition of a TiF_4 precursor is found to stabilize the {001} facet and chane the shape of TiO_2 nanocrystals.

The presence of an amine such as OLAM can sequester the fluoride ions before it can stabilize the {001} facet, thus providing a mechanism to tune the size and shape of monodisperse anatase nanocrystals[127]. At extremes of OLAM concentration, this synthesis yields either truncated bipyramidal nanocrystals similar to the Wulff construction (only OLAM) or high aspect-ratio nanoplatelets with an exposed {001} facet (only OLAL).

Gordon *et al* only described nanocrystal shapes at the extreme limits of cosurfactant ratios within an oleic acid-mediated chemothermal synthesis[127]. However, finer variations in the OLAM:OLAL ratio during synthesis with a TiF_4 precursor under controlled conditions can yield particles of intermediate size between the 10nm bipyramids and 500nm x 500nm nanoplatelets, although precise size control is difficult to reproduce. Different ratios of OLAM:OLAL were added in a slow-injection synthesis to produce substoichiometric nanoplatelets of sizes ranging from 5*15*15nm to 10*25*25nm. Sizes larger than this limit were found to agglomerate during film preparation, leading to variations in film morphology during deposition. STEM images in **Figure 4.1** demonstrate the range of particle sizes and morphologies synthesized in this manner, along with histograms obtained from visual particle sizing presented for comparison. The distribution of particle sizes overlaps to some extent, but the polydispersity is narrow enough to define the average particle size and characterize the size distribution. Scherrer analysis by XRD supported the visual particle sizing results, but lacked the precision to distinguish between different sizes and shapes.

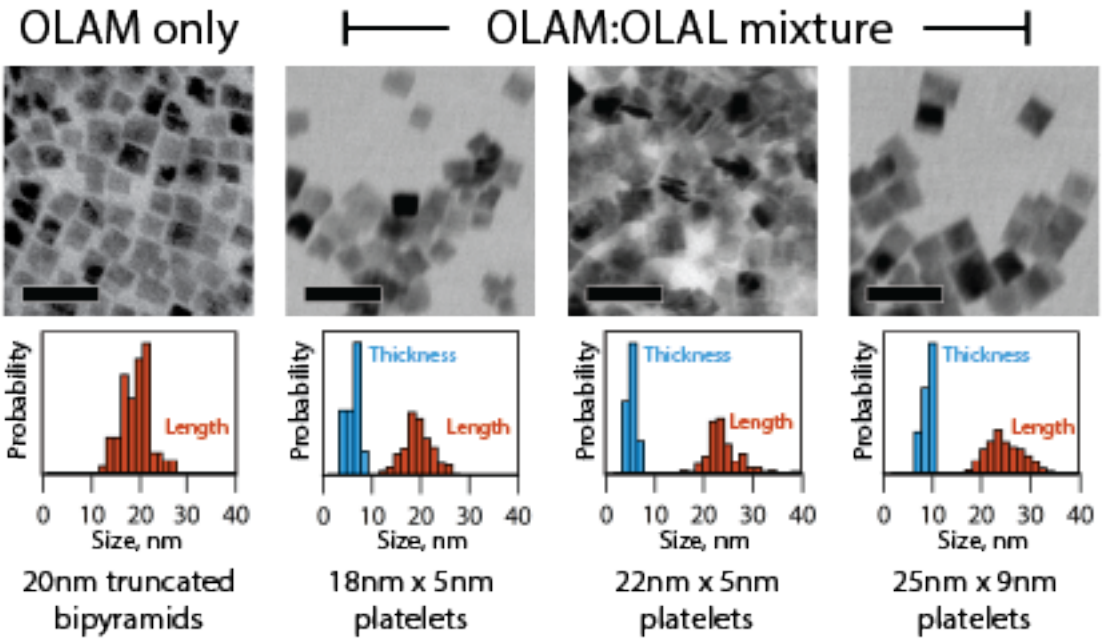

Figure 4.1: **S**TEM images of TiO_2 bipyramid and nanoplatelet syntheses. Histograms of particle sizes were measured by analysis of STEM images. Red histogram bars show measured particle length, and blue histogram bars show measured thickness for nanoplatelets. The scale bar is 50 nm. STEM bright-field images were recorded at 200k magnification with 30kV voltage and 20mA current.

The synthesis uses TiF_4 as a precursor, which has been observed to induce the creation of oxygen vacancies in anatase nanocrystals. Oxygen vacancies are compensated by free electrons in the lattice, increasing the Fermi level towards the conduction band. TiO_2 nanocrystals prepared from TiF_4 precursors were found to show characteristic resonant mid-infrared absorption characteristic of a localized surface plasmon, indicative of free carriers compensated by charged oxygen vacancies in the nanocrystal[127] . UV-Vis spectra of dispersions of each TiO_2 product in tetrachloroethylene were measured to

compare the optical bandgap between the different synthetic preparations (**Figure 4.2a**). The measured optical bandgap is consistent across the bipyramid and nanoplatelet samples, with a direct optical gap of 3.4 ± 0.1 eV (**Figure 4.2b**). The optical bandgap in undoped, stoichiometric TiO_2 nanocrystals prepared by a similar wet chemical synthesis is about 3.3 eV[82], much closer to the expected 3.2 eV electronic bandgap in anatase TiO_2[130]. The optical bandgap may be larger than the electronic bandgap if free carriers occupy the bottom of the conduction band, leading to a Burstein-Moss shift. In fact, the bandgap of 3.4 eV is similar to degenerate 10% Nb doped anatase TiO_2 nanocrystals[82], suggesting that these particles have high free carrier concentrations.

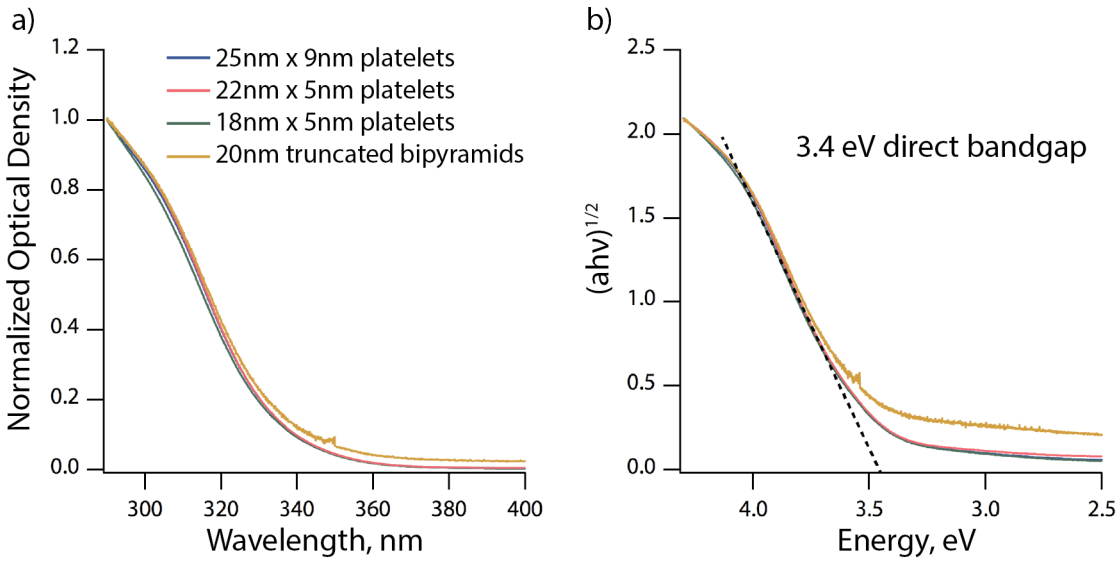

Figure 4.2 UV-Vis spectra of TiO_2 nanocrystals.

a) Normalized UV-Vis spectra of dispersions of TiO_2 nanocrystals in tetrachloroethylene. b) A Tauc plot of UV-Vis spectra showing the direct band-gap of the TiO_2 samples. The dashed line is included as a visual aid to estimate the direct optical bandgap.

Thin film electrodes were prepared from each nanocrystal sample to compare charging capacity and rate in a half-cell geometry. Nanocrystals were deposited from solution by spin-coating on conductive ITO-coated glass slides, with a thickness of 200-300 nm. The thin film geometry precludes the addition of electrically conductive binder because conduction and ion transport through the bulk film is rapid enough to prevent macroscopic polarization of the bulk electrode. The capacity of each film was estimated by cyclic voltammetry CV at 0.5 mV/s across a potential range of 3.5V to 1.5V in a 0.1M LiTFSI in tetraglyme electrolyte, yielding total capacities of 10-40 mC for each sample, equivalent to about 40-170 mAh/cm^3. All nanocrystal samples were found to retain their capacity within error after 10-20 cycling experiments across these potentials, but longer cyclability is expected from other studies of binder-free anatase TiO_2 electrodes[76].

Nanocrystal size and shape have been found to affect charge capacity, cyclabilty and charging rates in Li-ion cells at the device scale[76,131]. However, these phenomenological differences are obscured by the diverse charge compensation mechanisms in mesoporous insertion electrodes. Cation insertion, surface capacitance, and pseudocapacitive surface reactions can all contribute major portions of the total capacity. Wang *et al* found that the surface capacitive response of 10 nm anatase nanocrystal films charged in a Li-ion cell accounts for about a third of the total charge capacity by observing the rate-dependence of surficial and diffusive compensation mechanisms[74]. The kinetics of both surficial and intercalative processes should depend on particle size and shape. Porosity and surface area should affect rate and capacity of surficial charging processes, while changes in surface energies and diffusion pathways can affect the Li intercalation. To isolate the lithium intercalation reaction from convoluting non-faradaic processes, a Potentiostatic Intermittent Titration Technique (PITT) experiment was used to carefully monitor the current response of the film across discrete 5 mV charging steps. During each charging

step, the potential was held constant until the absolute current reached an equivalent C/25 rate. **Figure 4.3a** shows a PITT experiment for 25nm x 5nm nanoplatelets. The differential charge accumulated for each charging step was calculated by integrating the current during each potentiostatic titration. The surficial charge capacity is quite small across each small potential step, and is barely measurable in the potential range from 2V to 3V. However, a clear peak in differential charge is observed at 1.77V in the reducing (lithium intercalation) direction and 1.83V in the oxidizing (deintercalation) direction (**Figure 4.3b**). The differential capacity results also show an increasing capacity at lower potentials (below 1.6V), which may be caused by electrolyte side reactions, or the sluggish secondary reaction from $Li_{0.6}TiO_2$ to Li_1TiO_2. A shallow feature in the oxidative direction around 1.7V implies that some of the material is reduced to Li_1TiO_2 upon reduction, and undergoes a transformation back to $Li_{0.6}TiO_2$ upon oxidation. A comparison of the differential capacity of the three different sizes of nanoplatelets shows similar charging behavior between these samples. The intercalation potentials of bipyramidal nanocrystals are shifted by 5-10 mV from the nanoplatelet results, to 1.78V upon reduction and 1.835V upon oxidation. Each nanocrystal sample also shows a distribution in intercalation potentials, with charging peaks that span about 30mV around the peak maximum. The differences between the platelets and the bipyramids, as well as the distribution in intercalation potentials, may be consistent with an ensemble perspective of charging. At the nanoscale, surface energies are a significant fraction of total structural free energy, and may lead to particle shape and size dependence in lithium intercalation potentials[62]. A wide distribution of particle sizes, as found for the samples shown in **Figure 4.1**, would be expected to smear out the intercalation threshold across the range of intercalation energies embodied by each distinct particle in the ensemble.

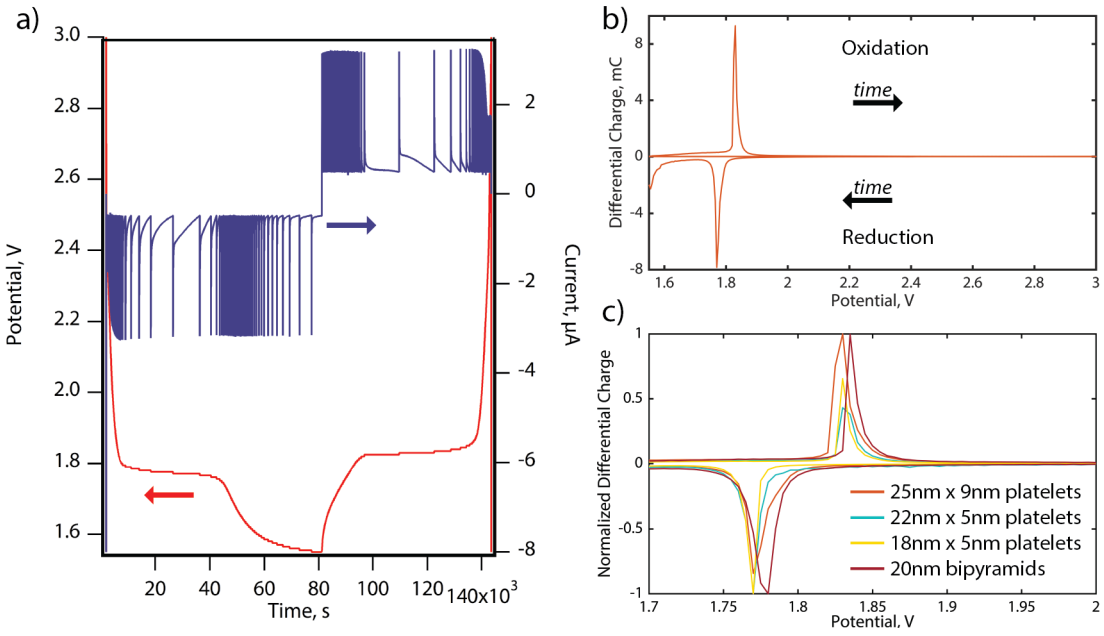

Figure 4.3. PITT electrochemical measurements of TiO_2 films.

a) Potentiostatic intermittant titration technique (PITT) measurement of current and potential response for a film of 25 nm x 9 nm nanoplatelets, during a 5mV step-wise charging routine with current limited to a C/25 rate. b) Integrated differential capacity across each potentiostatic charging step for the PITT measurement of 25 nm x 9 nm nanoplatelets shown in a). c) A comparison of differential capacity plots for the nanocrystal samples shown in **Figure 4.1**, each during PITT measurements with 5mV potential steps and a C/25 current limit.

The energetics of the nanoplatelet and bipyramid nanocrystal ensembles suggest that diversity in particle morphology contributes to the charging behavior of the film. However, a differential capacity measurement can only capture near-equilibrium properties of the material. Size and shape may affect charging lithium intercalation independent of the threshold potential of the reaction. The time-resolved kinetics of lithium intercalation

in nanocrystal electrodes can provide a wealth of information about the lithium diffusion and phase transformation dynamics. Recent studies of $LiFePO_4$ nanocrystal cathodes, which show a similar miscibility gap and 1st order phase transformation upon lithiation similar to anatase TiO_2, have found that charging kinetics can be used to study the effects of particle size on lithium intercalation[65]. Meethong *et al* have followed the kinetics of $LiFePO_4$ lithiation during PITT experiments and correlated this behavior with structural transitions monitored with diffraction techniques. The kinetics of the lithiation reaction, particularly within the 2-phase plateau region and across minor overpotentials near this boundary, can distinguish the size, shape and composition dependence of lithium intercalation and the 1st order phase transformation at the microscopic level[132-134]. Charging kinetics may resolve differences in Li-ion diffusion and phase transformation behavior across the range of particle shapes and sizes studied in this work. However, the kinetic charging response is convoluted by surficial charge compensation, and must be accounted for to describe the Li intercalation reaction.

Anatase TiO_2 presents an opportunity to isolate phase transformation kinetics because the intercalation reaction is accompanied by a well-characterized visible coloration. This color change is predicted to be caused by polaron gap states formed when electrons localize at Ti cations near intercalated lithium[30,31,95]. A simple approximation is that the absorption of the nanocrystal film at the polaronic feature scales linearly with the concentration of intercalated lithium in the film. However, it is unclear how these localized polaron states interact at high concentrations in nanocrystals, and in $Li_{0.6}TiO_2$ interactions between neighboring Li interstitials would be expected to perturb the localized electron states. At a macroscopic scale however, electrochromic coloration is simplified by considering heterogeneity in the nanocrystal ensemble. Wagemaker *et al* demonstrated that anatase TiO_2 nanocrystals smaller than 40 nm do not support phase coexistence between

the anatase TiO_2 and $Li_{0.6}TiO_2$ phases within the same particle[75,135]. Across the ensemble of nanocrystals in the film, coloration can thus be approximated as a linear sum of the total color of non-lithiated anatase and $Li_{0.6}TiO_2$ nanocrystals. An *in situ* measurement of film transmittance during a PITT charging measurement of a film of 25 nm x 9 nm nanoplatelets is shown in **Figure 4.4**. Two distinct optical modulations can be observed in the visible and infrared portions of the spectrum (**Figure 4.4a**), which can be attributed to lithium intercalation and surficial charging, respectively[68]. The 2000 nm feature is the tail of a localized resonant Drude response in conductive nanocrystals, and varies non-monotonically with potential. Conversely, optical density (OD) at 800 nm primarily increases across the 2-phase potential plateau in the charging curve (**Figure 4.4b**). A comparison of the differential color change across each PITT charging step with the differential charge capacity reveals that the two features are highly correlated (**Figure 4.4c,d**). Only a minor modulation in the optical density at 800 nm occurs at potentials above and below the 1st order intercalation threshold. The optical modulation at deeper reducing potentials than the intercalation threshold (1.5V to 1.7V) may be due to the secondary $Li_{0.6}TiO_2$ to Li_1TiO_2 reaction, but this change only accounts for a small fraction of the total coloration. Similar behavior was observed for each of the other nanocrystal samples shown in **Figure 4.1**. Hence, the optical transmission at 800 nm can be used as a reasonable *in situ* probe of the phase state of anatase TiO_2 during lithiation.

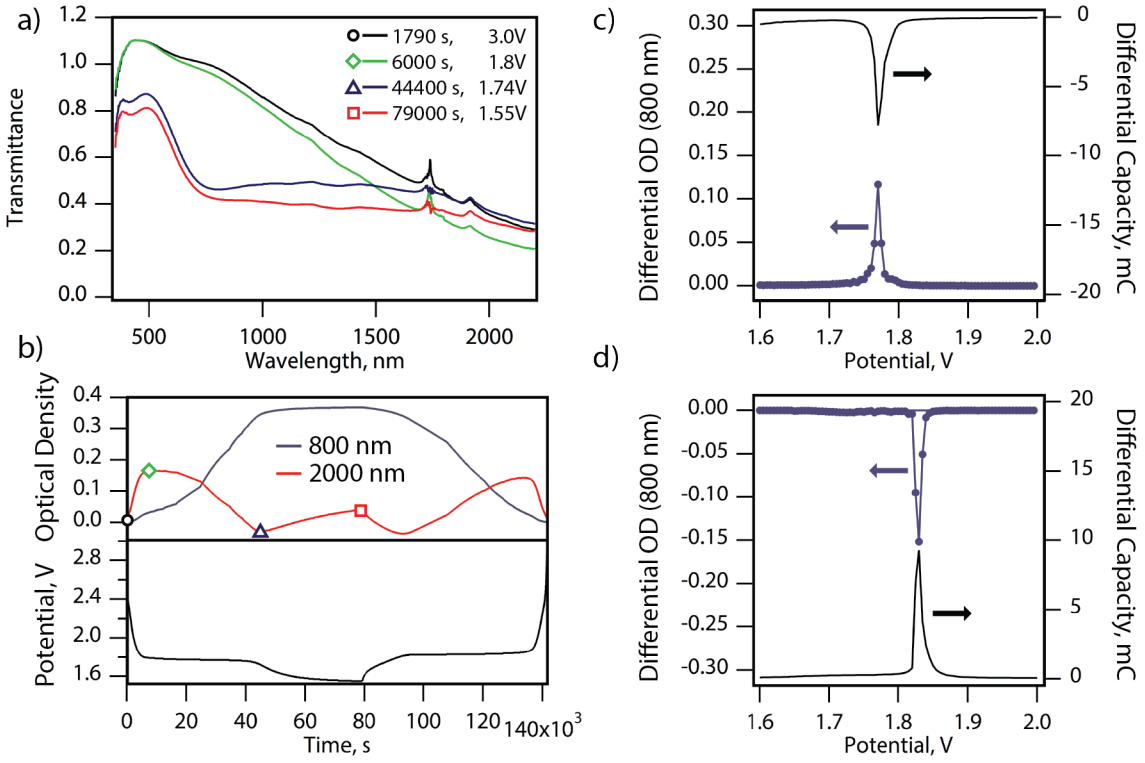

Figure 4.4. Optical transmittance of TiO_2 films during PITT experiments.

a) *In situ* optical transmittance spectra taken during the PITT experiment of 25 nm x 9 nm nanoplatelets shown in **Figure 4.3a** at different points during reduction. b) A plot of optical density at 800nm and 200nm vs. time, referenced to the time resolved potential measured during the PITT experiment. The markers correspond to the optical traces shown in a). The differential optical density for each PITT step is compared to the differential capacity in the same film during c) reduction and b) oxidation, showing a clear correlation between the optical and electronic responses.

The effects of size and shape dispersity on lithium intercalation in anatase TiO_2 nanocrystal ensembles can be measured directly with *in situ* optical measurements of the state of lithiation. The differential OD plots in **Figure 4.4c** and **Figure 4.4d** show a

distribution of optical modulation potentials around the peak maximum, similar in width to the differential capacity measurements. However, the time-resolved modulations shown in **Figure 4.4b** reveal that the optical modulations are not reaching steady state between each PITT charging step. Even at slow PITT cycling rates the system may still be kinetically limited. A more robust analysis can be made by probing the response of the electrode only at potentials near the intercalation threshold. The optical response of the film was used to equilibrate nanocrystal electrodes to a 50% state of charge (SOC) across the intercalation reaction. The SOC was calculated by comparing the optical density of the nanocrystal film to the extremes of the film color at fully oxidized (+3.5V vs Li/Li^+) and fully reduced (+1.5V vs Li/Li^+) during potentiostatic charging cycles. The optical 50% SOC was reached by applying a C/1 reducing current to an oxidized sample film for roughly 30 minutes, until a limit potential of 1.735V (accounting for a polarization of about 15 mV) is achieved. The film is relaxed under open circuit for 1 hour, leading to a slight oxidation but a reproducible starting point for charging experiments. A fixed overpotential relative to the final measured OCV was then applied for 2-3 hours and the current and optical response of the film at 800 nm was measured over that time. A measurement of the optical SOC during different overpotential charging experiments is shown in **Figure 4.5a** for a film of 25 nm x 9 nm nanoplatelets. The optical response has a decaying exponential character for all trials, and the rate and extent of intercalation increases with overpotential, approaching an asymptotic limit at the extremes of the charging window.

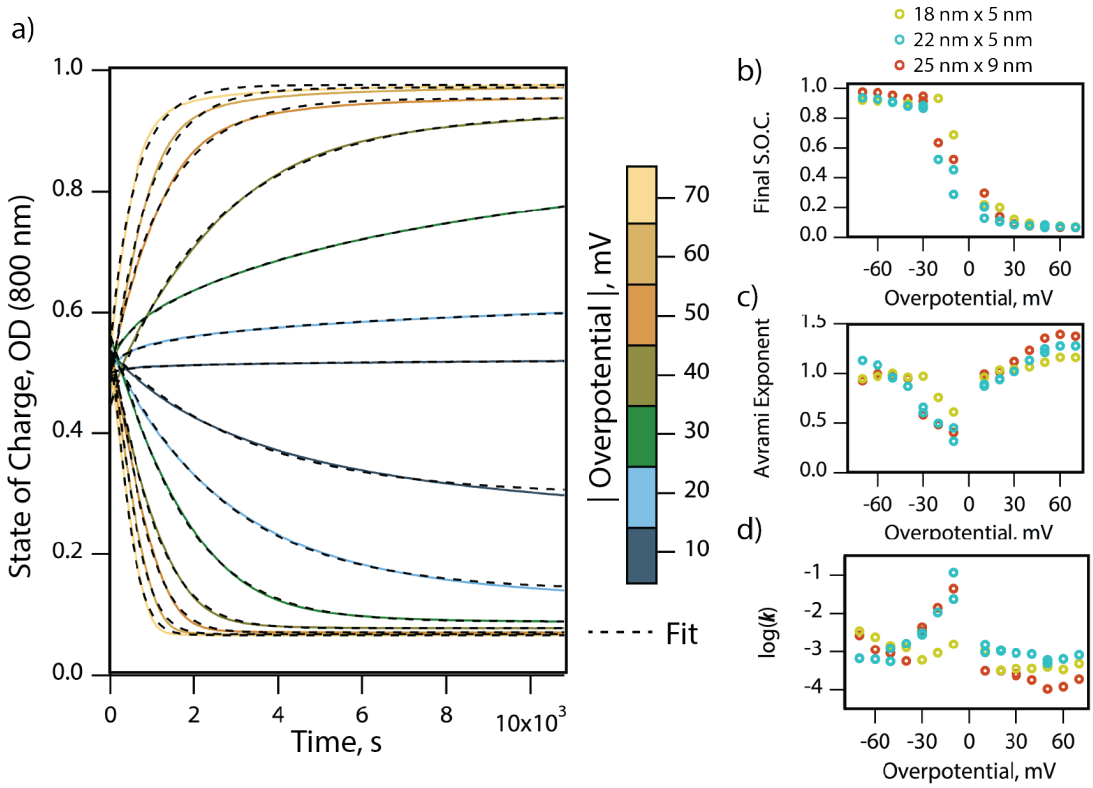

Figure 4.5: JMA model fits to overpotential state of charge measurements of TiO_2. a) The state of charge (SOC) for a 25nm x 9 nm nanoplatelet film, derived from optical density at 800 nm, is plotted as a function of time for films brought to a 50% SOC during lithiation and charged by small overpotentials on either end of the two phase plateau. The SOC is defined such that SOC=1 defines the fully darkened (lithiated) material, and SOC=0 defines the fully transparent (delithiated) material. Curves that increase in SOC over time show responses to a negative, reducing overpotential and curves that decreases over time follow positive, oxidizing overpotentials. The measured kinetics were fitted to a modified JMA model, yielding plots of the a) final SOC, b) Avrami exponent and c) log(k) prefactor as a function of overpotential and nanoplatelet size.

The charging curves were compared to a modified nucleation and growth model to quantify the behavior of the nanocrystal ensemble. The Johnson-Mehl-Avrami model is a standard description of nucleation and growth during recrystallization in solids. The JMA model assumes homogeneous, random nucleation across a non-interacting averaged volume of starting phase, with a complete solubility gap between the initial and final phases[64]. Although these assumptions seem intractable with heterogeneous, interfacial, mesoporous nanocrystal electrodes, the JMA model has been successfully used to study lithium diffusion and ensemble behaviors in $LiFePO_4$ microparticle films[65]. The JMA model describes the fraction of converted material, *SOC* (state of charge), during a complete phase transformation at time, *t*, through an exponential function:

$$SOC = 1 - \exp\left[-(kt)^n\right]$$

Here, the prefactor *k* is a product of a geometry factor and the time-resolved nucleation and growth rates in transforming particles, while the exponent *n*, commonly referred to as the Avrami exponent, can be further refined as:

$$n = p + qr$$

The term *p* describes the nucleation rate, with *p*=0 corresponding to instantaneous, complete nucleation at the beginning of the transition, and *p*=1 describing a constant nucleation rate. The dimensionality is described by *q*, with *q*=1 accounting for growth propagation in one dimension, *q*=2 for 2-D growth and *q*=3 for 3-D growth. The growth rate is described by *r*, where *r*=1 accounts for constant growth rate and *r*=0 describing instantaneous growth of nucleated particles.

The JMA model as written could not converge on reasonable fits of the experimental SOC measurements in **Figure 4.5a**, so an additional variable, SOC_{final} was introduced to describe the asymptotic limit of the transformation at long times. The new form of the equation accounts for the initial SOC, $SOC_{initial}$, as a constant measured at the

start of the experiment, and predicts how the SOC will evolve over time to the final asymptotic limit, SOC_{final} .

$$SOC = SOC_{initial}(1 - \exp[-(kt)^n]) + SOC_{final}(\exp[-(kt)^n])$$

The corrected JMA equation yielded excellent fits to the data at longer times and converged on reasonable values of the JMAK parameters (**Figure 4.5b,c,d**). Interestingly, at low overpotentials the nanocrystal ensembles do not approach complete (de)lithiation. Rather, at absolute overpotentials below 30mV, only a portion of the total color change is estimated to occur, even at long times. This result is consistent with an ensemble model of intercalation, in which each individual particle has a distinct intercalation potential defined by its size, shape and composition[62]. Furthermore, the range of overpotentials (30 mV in either direction) that defines this distribution of threshold voltages has a similar span to the width of the differential capacity and differential optical density peaks in **Figure 4.3c** and **Figure 4.4c,d**.

The Avrami exponent, n, and prefactor term, k, both show anomalous behavior at low overpotentials as well, although they stabilize at higher overpotentials. The Avrami exponent at larger overpotentials is between 1 and 1.5, indicative of either instantaneous nucleation and 1-dimensional growth (p=0, q=1, r=1), or else rapid diffusion and nucleation-limited kinetics (p=1, r=0). Belak *et al* have predicted that lithiation in anatase TiO_2 is highly anisotropic, and confined to 1-dimensional growth of the $Li_{0.6}TiO_2$ phase perpendicular to the anatase {010} facet. Belak *et al* also predicted that Li diffusion occurs most rapidly across the {001} facet during growth that propagates perpendicularly to this plane[67]. The nanoplatelets have an optimal structure to accommodate lithium intercalation across the wide {001} facet, and minimal interfacial energy along the growth vector because of the small cross-section along the {010} facet. Thus, it is likely that nucleation is the rate determining step during the overpotential experiment (p=1, r=0). This result

recent theoretical work that examines the diffusion-limited transformation in spherical and cylindrical anatase particles, which found that lithium diffusion is the rate determining step during intercalation[66].

It is worth noting that the Avrami exponent may be convoluted by ensemble charging effects. There is an apparent inverse correlation between the Avrami exponent and the prefactor k, so these parameters may not be independent during fitting. Also, if there is only a partial 'active population' of nanocrystals engaged in nucleation and growth at any particular overpotential, then the electrochemical environment experienced by each particle may deviate from the averaged charging properties captured by the JMA model[61]. Ultimately, a greater diversity of TiO_2 nanocrystal sizes and shapes should be examined to isolate the effects of different planar dimensions and faceting structures on lithiation kinetics.

CONCLUSIONS

Optical measurements of TiO_2 nanocrystal films during electrochemical charging reveal that heterogeneity within the nanocrystal ensemble influences the macroscopic charging behavior of the film. The distribution of differential charge capacity and color changes within 30 mV of the intercalation threshold suggests that the nanocrystal ensemble is composed of sub-populations of particles that transform at different potentials. Although this effect is small, a similar shift in charging potentials can be observed between nanoplatelet and bipyramidal shapes, indicating that nanocrystal size and shape are important factors in this distribution of intercalation energetics. The kinetics of the intercalation reaction, observed through *in situ* optical coloration, also indicate that the active population of transforming particles drops below 100% at potentials near the

intercalation threshold. Time-resolved optical measurements provide further insight into the geometric constraints of lithium intercalation in anatase TiO_2, which follows nucleation-limited kinetics based on the JMA model. This technique can be applied to a wider range of TiO_2 nanocrystal sizes and shapes to identify the role of different facets and diffusion pathways on the intercalation reaction in anatase TiO_2. Furthermore, the *in situ* spectroelectrochemical techniques described in this study can be applied to any electrode material with a well-defined change in optical absorption across a 1^{st} order electrochemical phase transition.

Chapter 5: Electrochemically Induced Transformations of Vanadium Dioxide Nanocrystals[†]

ABSTRACT

Vanadium dioxide (VO_2) undergoes significant optical, electronic, and structural changes as it transforms between the low-temperature monoclinic and high-temperature rutile phases. More recently, alternative stimuli have been utilized to trigger insulator to metal transformations in VO_2, including electrochemical gating. Here, we prepare and electrochemically reduce mesoporous films of VO_2 nanocrystals, prepared from colloidally synthesized V_2O_3 nanocrystals that have been oxidatively annealed, in a three-electrode electrochemical cell. We observe a reversible transition between infrared transparent insulating phases and a darkened metallic phase by *in situ* visible-near infrared spectroelectrochemistry, and correlate these observations with structural and electronic changes monitored by X-ray absorption spectroscopy, X-ray diffraction, Raman spectroscopy and conductivity measurements. An unexpected reversible transition from conductive, reduced monoclinic VO_2 to an infrared-transparent insulating phase upon progressive electrochemical reduction is observed. This insulator-metal-insulator transition has not been reported in previous studies of electrochemically gated epitaxial VO_2 films, and is attributed to improved oxygen vacancy formation kinetics and diffusion due to the mesoporous nanocrystal film structure.

INTRODUCTION

Bulk vanadium dioxide (VO_2) undergoes a reversible metal-to-insulator transition (MIT) at approximately 68°C, at which point the low-temperature monoclinic phase

[†] Content for this chapter was adapted from Dahlman *et al*[136] . C.J. Dahlman was co-lead author on this study and developed ideas, characterization, analysis and writing presented in this chapter.

transforms to the high-temperature rutile phase[36]. This structural transformation is accompanied by dramatic changes in the oxide's electronic and near infrared (NIR) optical properties[38,137]. Due to the relatively low temperature of MIT, VO_2 has been investigated for a variety of applications including solid-state memory devices[138-140], sensors[141], and smart-windows[37,142,143]. In addition to using direct thermal energy to trigger the transformation, this MIT phenomenon has also been observed in VO_2 using "all-optical"[144] and "all-electrical" [145-148] methods. In 2012, a dramatic MIT was observed in VO_2 via ionic liquid gating using an electric double layer transistor geometry consisting of a thin film of VO_2 as the channel and an ionic liquid as the gate[43]. Application of a gate voltage resulted in a lowering of the MIT temperature across the channel, with sufficiently high voltages leading to a stabilization of the metallic state across all temperatures. The mechanism behind this induced metallization, however, is the subject of debate. Nakano and coworkers first attributed this change in conductivity to collective bulk carrier delocalization induced by electrostatic charge accumulation at the ionic liquid interface. Nakano's description of the electronic origin of this electrochemical MIT follows the explanation from Zylbersztejn and Mott that insulating behavior in monoclinic VO_2 is driven by strong electron correlations, rather than purely structural distortions[39]. In a similar configuration in 2013, however, Jeong and co-workers found that ionic liquid gating does more than electronically charge the VO_2 film, reporting that metallization was accompanied by the generation of oxygen vacancies within the material[45]. Subsequent studies by both groups found that VO_2 films undergo significant structural changes during gating, with an anisotropic expansion of 3% oriented along the rutile c-axis, parallel to the direction of V-V dimerization in monoclinic VO_2 and of the open oxygen-diffusing channels along shared edges of VO_6 octahedra[47,149,150]. The electrochemical MIT was found to be substrate dependent; epitaxial orientations that aligned the rutile c-axis parallel to the growth substrate impeded c-axis

strain or oxygen diffusion, and did not show gating induced structural or electronic changes[44,45]. The expanded metallic phase induced by gating was proposed by Karel *et al* to be a distorted oxygen-deficient monoclinic structure showing decreased V-V dimerization and d-band splitting[46], drawing from Goodenough's description of the thermal MIT in VO_2 as a structural Peierls-like instability in the V3d band[38]. Recent studies of gated VO_2 films covered with mediating capping layers have provided additional evidence for the role of oxygen vacancy defects in the electrochemical MIT. A graphene monolayer grown between a VO_2 thin film and gating electrolyte impedes the MIT by blocking oxygen diffusion out of the lattice[151], while epitaxial capping layers of rutile TiO_2 that are thick enough to occupy the entire electrostatic screening length still enable gated MIT through oxygen diffusion out of the VO_2 lattice[152]. Remarkably, gated optical and electronic switching penetrates to a depth of at least 90 nm in an epitaxial VO_2 film, even though the region of high strain fields[144], oxygen exchange[45] and electrostatic screening[151] only extend about 10 nm into the surface. Orientation and strain accommodation strongly influence the gating process, although the latter is limited by the coherence of the gated film with its underlying substrate.

Nanocrystals (NCs) are expected to accommodate strain better than epitaxial films due to the lack of constrained coherence with neighboring grains or the underlying substrate. A recent study by Sim *et al* found enhancement of the ionic liquid gating effect in self-supported VO_2 sub-50 nm thick membranes compared to sputtered films of similar thickness, proposing that the unconstrained VO_2 electrolyte interface simultaneously enables relaxation of tensile stress and minimizes diffusion pathways to the electrolyte[153]. Nanocrystalline films should similarly accommodate strain and surface diffusion processes through an abundance of electrolyte interfaces. We therefore hypothesized that

electrochemically induced MIT would be observed in films of VO_2 NCs without the limitations imposed by crystalline orientation that are inherent to epitaxial thin films.

Despite the interest in VO_2 NCs for their desirable optical properties[154] and potential for size-dependent phase behavior[155], their chemical synthesis remains challenging. The complicated phase diagram of the vanadium-oxygen system contains many stable and metastable compounds and phases, thus making stabilization of a particular phase difficult[156]. Nevertheless, several routes to nanostructured VO_2 with varying degrees of morphology control have been reported including solvothermal synthesis[157-159] and polymer assisted deposition[160]. Optical quality films suitable for spectroelectrochemical investigation can be readily prepared from colloidal nanocrystals[83,109] thus making this approach to VO_2 NCs most attractive. Unfortunately, a direct colloidal synthesis of VO_2 NCs has not yet been reported. In the closest example, Paik and co-workers reported the conversion of VO_x colloidal NCs with an unidentified crystal structure into VO_2 films using a rapid thermal annealing process; however the reported process sinters the nanocrystals into a non-porous film of larger polycrystalline particles[161].

Here, we report the development of a low-temperature, oxidative annealing process to convert films of metastable bixbyite V_2O_3 NCs[162] to VO_2 while maintaining mesoporous, nanoscale crystalline domains and high optical quality. Upon electrochemical reduction, these NC films transform from monoclinic phase to an IR blocking, conductive monoclinic state, consistent with the effects of ionic liquid gating on VO_2 thin films. However, upon further reduction we observe a reversal in this IR darkening, leading to a new IR transparent state that, according to X-ray absorption spectroscopy (XAS) and X-ray diffraction (XRD), is an oxygen-deficient expanded rutile-like phase. Hence, the electrochemical reduction of our VO_2 NC films can instigate a reversible phase transformation that has not been revealed by gating epitaxial thin films with ionic liquid electrolyte.

DISCUSSION

Following our previously published method, V_2O_3 colloidal NCs with a metastable bixbyite crystal structure were first synthesized via aminolysis reaction using standard Schlenk line techniques[162]. Films of V_2O_3 NCs were prepared via spin or drop casting from solvent then converted to VO_2 via a mild annealing treatment at low oxygen partial pressure (375°C, 250 ppm O_2 in N_2). Transmission electron microscopy (TEM) was used to observe the morphology of the NCs before and after conversion (**Figure 5.1a, b**). The as prepared V_2O_3 NCs are well separated with an average diameter of approximately 25 nm. During the oxidative transformation, diffusion leads to necking between the NCs, resulting in a porous NC network. The crystal structure before and after conversion was determined via X-ray diffraction (XRD), and indexed to the bixbyite V_2O_3 and monoclinic VO_2 structures, respectively (**Figure 5.1c**). A decrease in XRD peak widths between bixbyite and monoclinic suggests that a small degree of coarsening occurs upon conversion. This coarsening is dependent on annealing temperature, with higher temperatures yielding larger VO_2 crystallites as determined by Scherrer analysis (**Figure A20**). The resulting VO_2 NCs are thermochromic, exhibiting diminished IR transmittance at elevated temperature (**Figure 5.1d**), consistent with the expected MIT phase transformation from monoclinic to rutile phase.

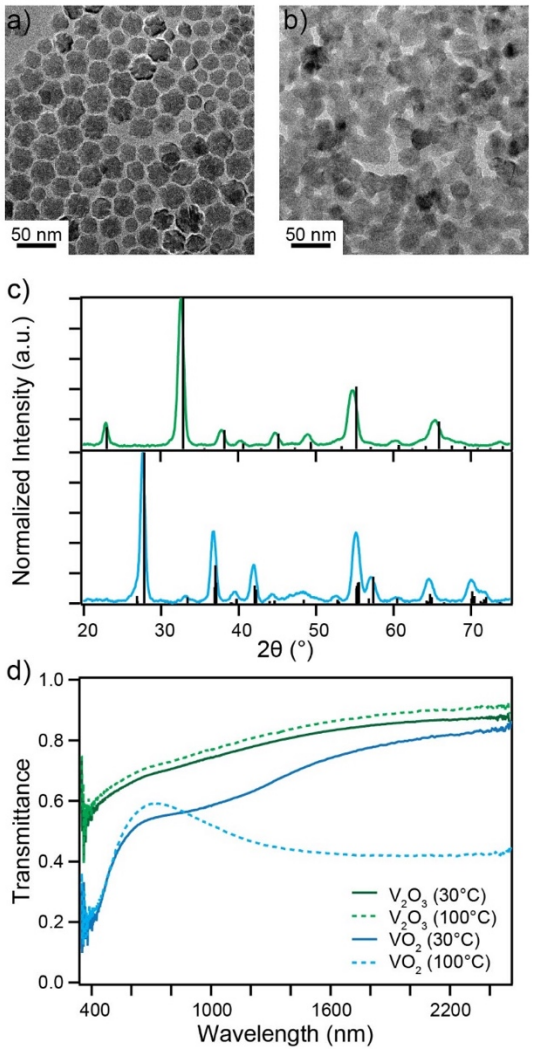

Figure 5.1: Characterization of V_2O_3 NCs and converted VO_2 NCs.

TEM images of a) colloidal V_2O_3 NCs and b) VO_2 NCs generated via thermal annealing. c) XRD pattern of bixbyite V_2O_3 NCs (green/top) and monoclinic VO_2 NCs (bottom/blue). Reference XRD patterns [ICSD collection code 260212 and 15889] are shown in each plot. d) Transmittance spectra of NC thin films demonstrating minimal change for V_2O_3 and dramatic NIR modulation for VO_2 as a function of temperature.

To investigate the response of our VO_2 NCs to electrochemical biasing, in situ variable temperature spectroelectrochemistry was performed. In an inert atmosphere glove box maintained at < 1 ppm O2, VO_2 films on ITO-coated glass were submerged in an electrolyte consisting of 0.1 M bis-trifluoromethanesulfonimidate (TFSI) salt in propylene carbonate. In our homebuilt apparatus, the VO_2 film acted as the working electrode while platinum and a fritted Ag/Ag+ cell were used as counter and reference electrodes, respectively. Temperature was controlled using a Peltier thermoelectric element with a center hole to allow a continuous optical path through the VO_2 film, enabling collection of vis-NIR transmission spectra in situ using a fiber-coupled spectrometer (**Figure A9**). Irreversible optical changes were observed when lithium-containing electrolyte was used, likely due to the intercalation of Li+ ions in the VO_2 lattice resulting in an irreversible phase transformation (**Figure S3**), consistent with the results of Kahn *et al* on thin films[163]. When lithium was replaced with a bulky counter-ion, specifically tetrabutylammonium (TBA^+), intercalation was inhibited and reversible optical modulation was observed.

Upon application of a reducing bias (-1.5 V vs NHE) at room temperature, a strong decrease in NIR transmittance was observed (**Figure 5.2a**). This spectroscopic observation is in agreement with the previous report of metallization in ionic liquid gated epitaxial VO_2 films[34]. Our results demonstrate that optoelectronic modulation is possible in NCs even without ionic liquids, which are known to deliver the highest local fields. Furthermore, darkening is found to occur at very low applied potentials, albeit at a slower rate (**Figure 5.2b**). Continued application of a reducing bias beyond the initial darkening, however, eventually leads to an unexpected reversal of the IR darkening (**Figure 5.2c**). The bleaching effect is much slower than IR darkening, and was only observable after long charging times at moderate reducing potentials. We also observed voltage-induced IR bleaching upon reduction of the rutile phase at 100°C, but at a much faster rate (**Figure**

5.2d). The more rapid bleaching of hot rutile may be due to faster kinetics of oxygen diffusion, metallic conductivity or increased electrochemical reactivity[164] in rutile VO_2.

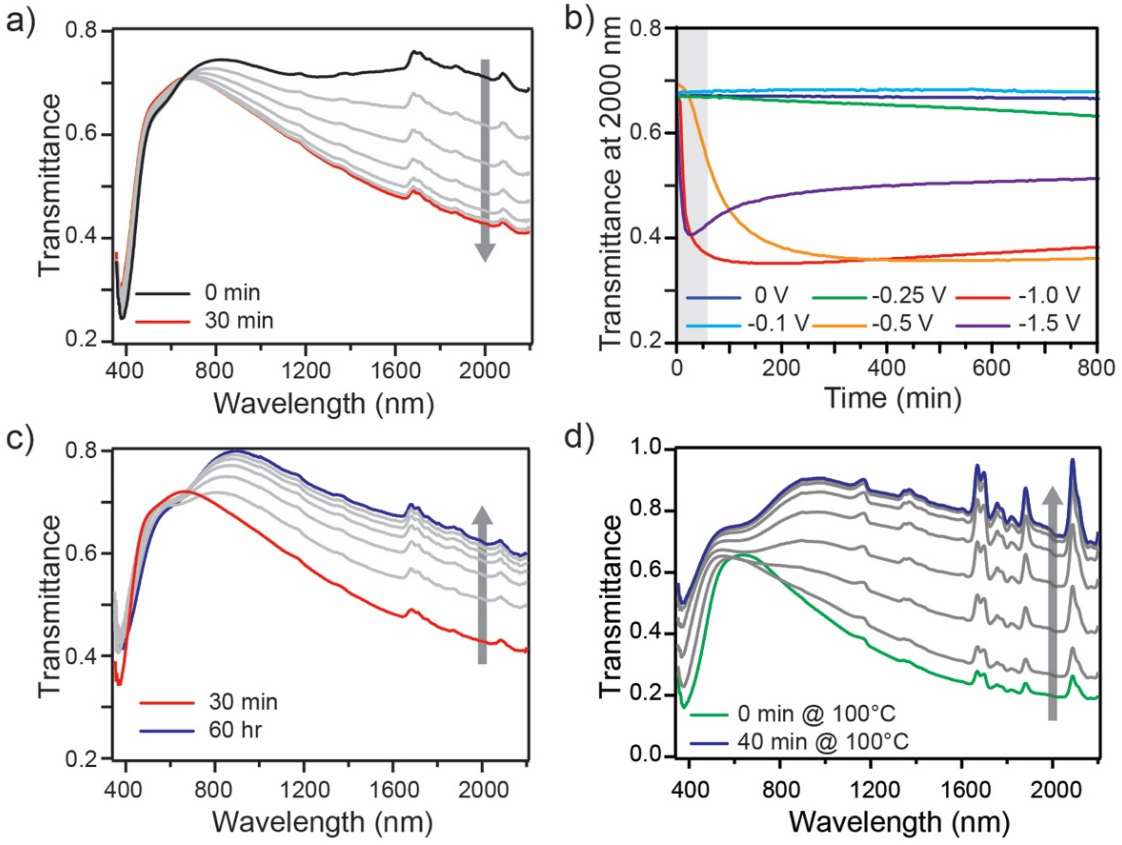

Figure 5.2: Spectroelectrochemistry of VO_2 NC films on ITO-coated glass

a) Darkening of NIR transmittance generated by applying -1.5V vs NHE in 0.1 M TBA-TFSI electrolyte at 25°C in argon with scans taken every 5 minutes for 30 minutes. b) The effect of applied potential on the transmittance of 2000 nm light as a function of time at 25°C in argon. c) Bleaching of NIR transmittance after applying -1.5V vs NHE at 25°C in argon starting at 30 minutes, with scans taken every 10 hours for 60 hours. d) Electrochromic behavior of VO2 NC films at 100°C in argon. Films were brought to the rutile phase thermally before applying a reducing potential with traces taken every 5 minutes until saturation.

Darkening and bleaching were found to be reversible upon the application of an oxidizing potential (**Figure A12** and **A13**). Interestingly, we found that electrochemical modulation of IR transmittance was possible even in an oxygen-rich environment, albeit with lower coloration efficiency than in an inert environment (**Figure A14**), an effect not observed in previous ionic liquid gated epitaxial films despite the higher achievable local fields[45]. After removing electrochemical bias, both darkened and bleached films exposed to air were observed to slowly return to an optical state characteristic of the original monoclinic structure while films in argon remained unchanged (**Figure A15**). In fact, as long as the film was not exposed to oxygen, we could remove and rinse the electrode with no effect to the optical state, suggesting that the material is transformed under applied potential, not merely gated electrostatically.

To correlate the observed optical changes with electronic properties, we measured the temperature dependent electrical resistivity of unbiased and charged VO_2 films. Measurements were made air-free with four-point probe in the Van der Pauw geometry to avoid oxidation of the material (**Figure 5.3**). The unbiased films show the characteristic MIT of VO_2 around 68°C, and a hysteresis of about 20°C between heating and cooling curves. Note that the resistivity in these films is much higher than would be expected for bulk[137] or thin-film[43] VO_2 due to film mesoporosity. Nonetheless, the resistivity of unbiased films changes by two orders of magnitude across the thermal MIT. Electrochemical biasing shows similar switching, inducing lowered resistivity in the IR darkened state and an order of magnitude higher resistivity in the IR bleached state. We therefore attribute our spectroelectochemical observations to a sequential insulator-metal-insulator transition. Furthermore, both the bleached and darkened states retain their resistivity and optical transmittance across the entire tested range of temperatures, demonstrating that the thermal MIT is suppressed upon biasing (**Figures 5.3 and A16**).

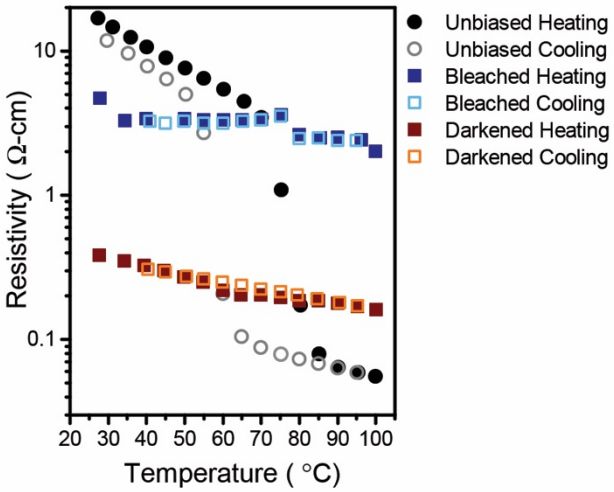

Figure 5.3: Van der Pauw geometry resistivity measurements of VO_2 films. Resistivity of unbiased, bleached (-1.5 V vs NHE at 100°C in argon for 30 minutes) and darkened (-0.5 V vs NHE at 25°C in argon for 17 hours) VO_2 films. All films were 107 +/- 3 nm thick.

To understand the structural changes occurring with progressive reduction, we performed X-ray diffraction, and X-ray absorption and Raman spectroscopies on NC films in various optical states, including the initial monoclinic, thermally darkened (rutile), electrochemically darkening, and partly or fully electrochemically bleached states. Films were prepared on doped silicon for use across a range of analytical techniques. As the kinetics of darkening and subsequent bleaching in the IR are sensitive to applied bias (**Figure 5.2b**) and temperature (**Figure 5.2c** and **5.2d**) these states were accessed using different time-potential-temperature trajectories to avoid ambiguity and ensure that a complete set of samples in different optical states was obtained for analysis (**Table A1**).

To assess the crystal structure of the NC film in different optical states, we utilized *ex situ* Grazing-Incidence Wide Angle X-ray Scattering (GIWAXS) on biased films in an

air-free helium enclosure (0.1% O_2) (**Figure 5.4a**). The unbiased films show peaks characteristic of monoclinic VO_2, albeit with a slight distortion to larger Q values due to the grazing incidence geometry. The darkening film retains the monoclinic structure with minimal distortion. However, further reduction shows a progressive increase in the lattice constants from the bleaching to the fully bleached states (**Figure A17**). This is accompanied by a widening of the peaks, likely due to increased inhomogeneous strain, and disappearance of the smaller monoclinic peaks. The bleached state can be indexed to an expanded rutile lattice, although the broadened peaks may hide possible minor features indicative of structural distortions. Raman spectroscopy also supports a structural transformation from a monoclinic structure in the unbiased and darkened films to a more symmetric rutile-like structure upon bleaching (**Figure A18**). Unlike earlier studies of gated epitaxial VO_2, which found a 3-5% out-of-plane expansion in the rutile c-axis, we find very little expansion upon darkening. Instead, lattice expansion happens mostly during bleaching, with the fully bleached state experiencing isotropic lattice expansion of roughly 2% along all three rutile axes (**Table A2**), or about 7% volume expansion. These results suggest that the NC morphology allows relaxation with minimal constraint, unlike epitaxial VO_2 films in which lattice expansion is restricted to the rutile c-axis[44,47,149,150].

X-ray absorption near-edge spectroscopy (XANES) at the vanadium K-edge was used to characterize the electronic structure of biased VO_2 NCs. A progressive shift in absorption edge indicative of a reduction in the vanadium oxidation state was observed in the near-edge region of the spectra (**Figure 5.4b**), implying that inserted charge localizes on vanadium cations. A shift in absorption edge, and formal oxidation state, is apparent from monoclinic VO_2 (+4.0) to the darkened state (+3.9), and is more dramatically reduced in the bleached state (+3.3) (**Table A3**). In the absence of other compensating species such as hydrogen or metallic dopants, this oxidation state change is consistent with

compensation of oxygen vacancies upon electrochemical reduction. The pre-edge feature at approximately 5470 eV, attributed to a transition from the V1s to V3d electronic states, was also observed to decrease in intensity with increasing reduction. This transition is symmetry forbidden, and its suppression in the XANES spectra suggests either more d-like character of the V3d orbitals, which is consistent with an increase in octahedral symmetry, or state filling of the V3d bands upon bleaching. [165,166]

GIWAXS measurements suggest a transformation to a new crystalline phase upon electrochemical bleaching, but the technique can only resolve the long-range order within crystalline domains. Therefore, the extended X-ray absorption fine structure (EXAFS) at the vanadium K-edge was studied to determine the local bonding environment surrounding vanadium. As expected, the darkening and monoclinic patterns are nearly identical, confirming that the darkening state indeed remains in the monoclinic phase even as it becomes metallic through electrochemical reduction. In contrast to the GIWAXS results, however, the EXAFS pattern of the fully bleached state does not match the pattern expected for a simple expansion of the rutile phase. The bleached state shows a narrowed, large amplitude first bonding shell peak at 1.5Å, similar to rutile, which indicates that bleaching recovers local VO_6 octahedral symmetry from the distorted monoclinic or darkening states[165]. This amplitude change is accompanied by a slight increase in the nearest-neighbor V-O bond peak distance as well as distortions in other features across the EXAFS oscillations (**Figure A19**), suggesting an expanded, unique phase with high local octahedral symmetry.

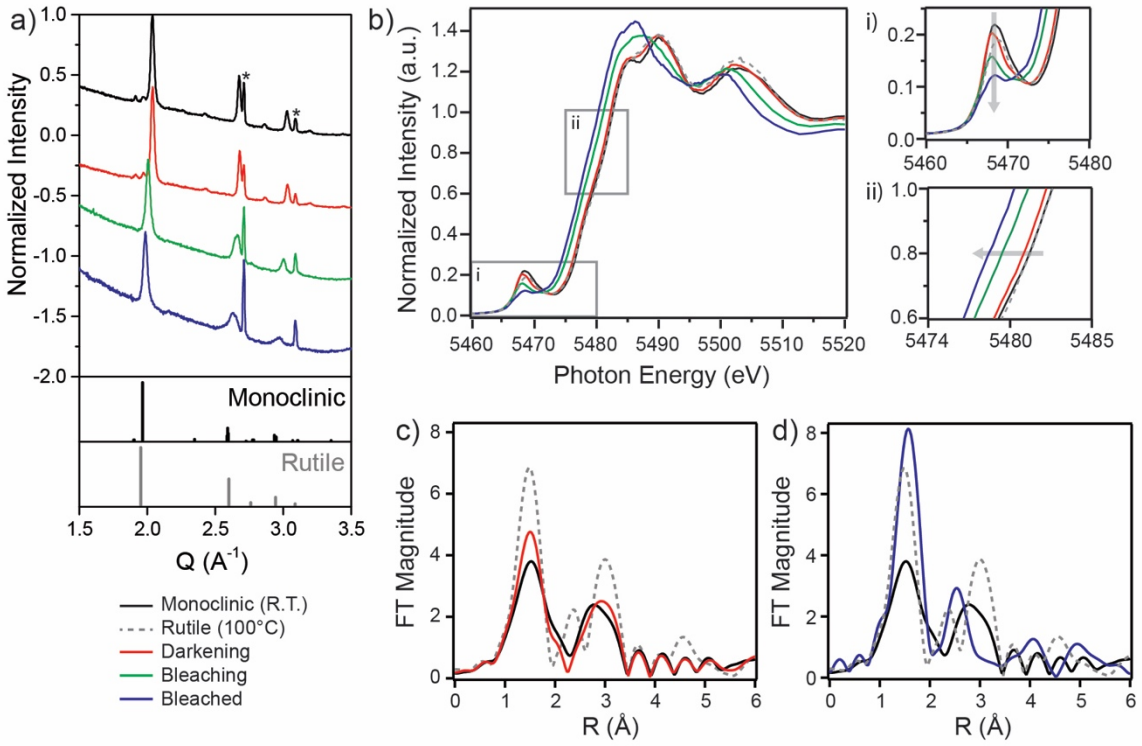

Figure 5.4: Characterization of monoclinic, rutile, darkening, bleaching, and bleached states.

a) GIWAXS with the VO_2 monoclinic [ICSD collection code 15889] and VO_2 rutile [ICSD collection code 647637] patterns included for reference, and marked (*) peaks arising from background aluminum in the sample stage. b) X-ray absorption near edge spectroscopy of the V K-edge, with zoomed in views of the i) pre-edge feature and ii) absorption edge. The Fourier transformation of the k^3 weighted EXAFS of the c) darkening state and d) bleached state with monoclinic and rutile shown in each for comparison.

Observation of the bleached phase indicates a sequential insulator-metal-insulator transition in VO_2 upon biasing, but the mechanism of this transformation remains unclear. To elucidate the influence of NC morphology on the observed darkening and bleaching

processes the insulator-metal-insulator transition was induced in VO_2 NC films with different crystallite sizes (**Figure A20**). Sequential darkening and bleaching was modeled as a two-time exponential process, and the time evolution of extinction at 2000 nm with an applied bias was fitted to extract kinetic parameters for different films (**Table A4**), including exponential time constants for the darkening and bleaching transformations (**Figure 5.5**). The kinetics of the initial darkening process in the NC films is not obviously size dependent, however the fitted time constant for bleaching increases by an order of magnitude as crystallite size increases from 23 nm to 50 nm. Microcrystalline planar films with significantly larger grains, prepared via the thermal condensation of vanadium oxalate clusters (**Figure A21**)[167], showed very little change in IR transmittance upon the application of a reducing bias (**Figure A21 and A22)**, and no evidence of bleaching. Thus, nanoscale morphology is crucial to observing the electrochemical insulator-metal-insulator transition in our device geometry.

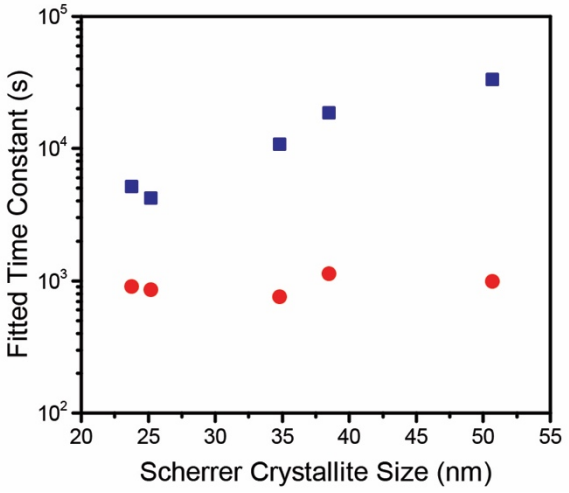

Figure 5.5: Fitted exponential time constants of VO_2 bleaching kinetics. Calculated for a two-time exponential model of the darkening (red circles) and bleaching (blue squares) processes plotted as a function of Scherrer crystallite size. Time constants were fit to measurements of extinction at 2000 nm vs. time upon bleaching at -1.5V in 0.1M TBA-TFSI in PC in argon atmosphere at 25°C.

Both surface strain effects and oxygen diffusion kinetics may account for the NC size-dependence in our biased films. The high electrolyte interfacial area of mesoporous VO_2 NC films creates more diffusion pathways for oxygen to escape the lattice than in an epitaxial film of equivalent thickness. However, oxygen has been found to diffuse most readily along the rutile c-axis direction, so a thin epitaxial film with the oxygen-diffusing rutile c-axis channels oriented normal to the substrate, such as the 10 nm epitaxial films prepared by Jeong *et al*[47], should have equally favorable oxygen diffusion. Thus, it is likely that strain relaxation also plays an important role in the unique switching behavior we observe. A recent study by Passarello *et al* found that the strain field accompanying oxygen vacancy driven metallicity in electrolyte gated VO_2 decreases exponentially below a thin 6

nm layer at the electrolyte-VO_2 interface[150]. Thus, each NC grain in our biased films is expected to be significantly strained, regardless of film thickness. Furthermore, the isotropic distribution of crystal facets in VO_2 NC films may result in spatially inhomogeneous strain fields, rather than the directional strain studied in epitaxial films. A study by Appavoo *et al* on the size dependence of the thermal MIT in VO_2 nanoparticles made by lithographic patterning found that oxygen vacancy defect formation energy is strongly dependent on interfacial strain and the exposed crystal facet. In fact, they found that oxygen-vacancy formation was most favorable at the (011) facet, rather than the (001) facet exposed in the oriented VO_2 films studied by ionic liquid gating[168]. Thus, the diversity of exposed facets in the NC film, and isotropic strain relaxation in NC grains, would be expected to lower oxygen vacancy formation while simultaneously enabling structural phase transformations and rapid oxygen diffusion along favorable lattice directions. These conditions had not been met in prior studies on epitaxial or polycrystalline films, which may explain our unique observation of an electrochemical insulator-metal-insulator transition.

A similar insulator-metal-insulator transition has very recently been observed at room temperature upon hydrogenation of epitaxial VO_2 thin films, accompanied by a 10% out-of-plane lattice expansion[169]. Hydrogen incorporation, like oxygen vacancy formation, is compensated by electrons in the film and decreases vanadium-oxygen orbital mixing in an expanded lattice. Interestingly, the expansion measured in hydrogenated epitaxial VO_2 films is directed along the a lattice parameter, with no concurrent strain in the c lattice parameter as would be observed upon electrolyte gating. Nevertheless, DFT calculations performed by Yoon *et al* show that the addition of one electron per VO_6 octahedron in the rutile lattice (without any hydrogen) leads to a 16% expansion of the rutile a lattice parameter. This expansion was accompanied by a narrowing of 3d bands, consistent with

Yoon *et al*'s observations of insulating behavior in hydrogenated VO_2. Tungsten doping has also been found to induce a sequential insulator-metal-insulator transition by acting as a substitutional donor dopant in $W_xV_{1-x}O_2$. At sufficient doping levels ($x > 0.09$) donor electrons occupy the V3d bands at the Fermi level and induce metallic behavior. However, higher doping ($x > 0.10$) leads to insulating behavior and significant structural expansion. Sakai *et al* attributed this insulating behavior to either electron correlations or narrowing of V3d bands due to lattice expansion, consistent with Yoon *et al*'s observations of hydrogenated VO_2. [170,171]

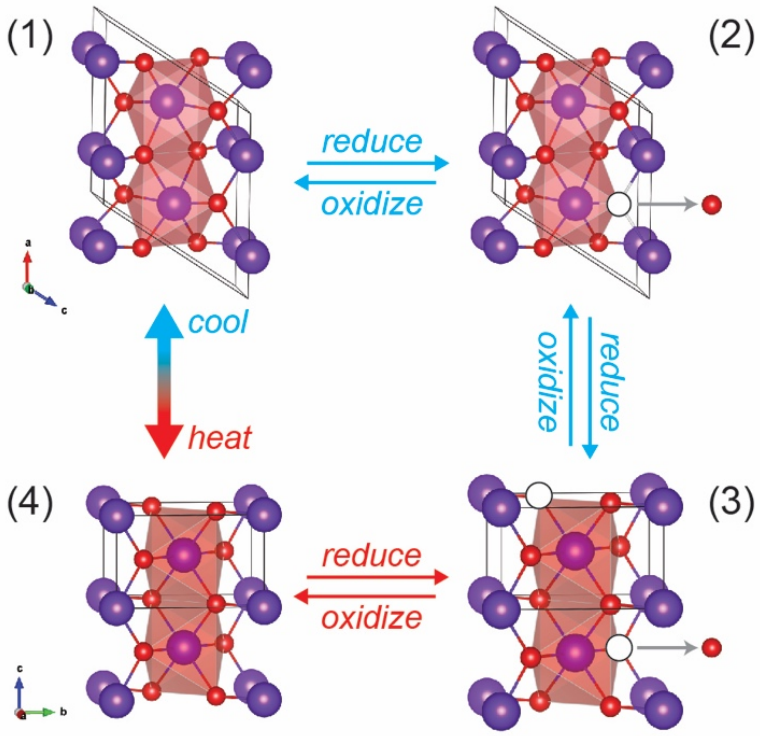

Figure 5.6: Schematic illustrating the pathways to 4 distinct states of VO_2 NC films. (1) The low-temperature, IR-transmitting insulating monoclinic state, (2) an oxygen deficient, IR-blocking, metallic monoclinic state, (3) an IR-transmitting, insulating expanded rutile-like structure, and (4) the high-temperature, IR-blocking metallic rutile state. These states can be accessed via heating/cooling and electrochemical reduction/oxidation, denoted by arrows in the diagram. The purple spheres are vanadium atoms and red spheres are oxygen atoms, with open circles indicating oxygen vacancies.

Based on our XANES results, up to 0.7 electrons may be accumulating per VO_6 octahedron during the bleaching process and this estimate would be expected to induce a significant volume expansion in rutile VO_2 according to Yoon *et al*'s DFT calculations. In fact, the 7% volume expansion of the bleached phase estimated from GIWAXS data (**Table**

A2) is roughly consistent with Yoon's results[169]. However, the different conditions and strain geometry of biased VO_2 NC films in this work and hydrogenated epitaxial VO_2 films in Yoon's work renders a direct comparison of these two phenomena difficult. Therefore, we propose that the successive insulator-metal-insulator transformations in biased VO_2 NCs are caused by a dramatic increase in oxygen vacancy concentration, which is first compensated by V3d band filling, but at sufficient levels induces band narrowing due to a phase change and isotropic lattice expansion.

CONCLUSIONS

In summary, we have demonstrated the ability to thermally and electrochemically modulate the IR transmittance of VO_2 NC films, prepared by controlled oxidation of V_2O_3 colloidal NCs, through four distinct transformations (**Figure 5.6**). Initial application of a reducing bias leads to diminished electrical resistance and IR transmittance, as anticipated based on previous ionic liquid gating experiments performed on epitaxial VO_2 films. However, further reduction of our NC films was found to result in bleaching in the IR and an increase in resistance, leading to a never before seen transition to an expanded, insulating rutile-like state. This progressive optical switching was made possible by the nanocrystalline nature of the films, in which the abundant VO_2-electrolyte interfaces facilitate rapid oxygen vacancy formation and diffusion kinetics and strain due to lattice expansion is readily accommodated.

Appendix 1: Supporting Information for Chapter 2

NIOBIUM DOPED ANATASE TITANIA NANOCRYSTAL SYNTHESIS

The synthesis of niobium-doped anatase TiO_2 (Nb-TiO_2) nanocrystals (NCs) was adapted from de Trizio et al.[82], with slight modifications. For both the Nb-doped and undoped TiO_2 NCs, a mixture of oleic acid (2 mmol) and oleyl alcohol (26 mmol) in octadecene (ODE, 8 mL) was degassed under vacuum at 120°C for 1 hour in a three-neck flask. A solution of niobium pentachloride ($NbCl_5$) in ODE (2 mL) was stirred and heated to 80°C under nitrogen atmosphere for one hour to dissolve the precursor. After one hour of heating the $NbCl_5$ in ODE solution, titanium ethoxide (TEO, 2 mmol) was added creating a clear solution. Immediately after adding TEO, the precursor solution was rapidly injected via a syringe into the degassed solvent of the three-neck flask, under nitrogen atmosphere. The temperature of the reaction vessel was then raised to 290°C for 60 minutes to grow the TiO_2 NCs. After cooling to room temperature, the NC solution was washed by precipitation with acetone and redispersion in hexane, repeated four times. After each precipitation, 100μL of oleic acid was added to the NC solution to stabilize the colloidal particles. The final NC solution was prepared by redispersing the particles in 2mL of hexane and 15μL of oleic acid. Nb doping content is expressed as the percentage of Ti sites occupied by Nb in the anatase structure. The Nb to Ti ratio was measured by digesting NC solutions for one day in a concentrated aqueous solution of 10:1 HCl to HNO_3. Inductively Coupled Plasma-Optical Emission spectra of the digested solutions were obtained with a Varian ICP-OES 720 Series spectrometer to calculate the Nb:Ti ratio.

ELECTRON MICROSCOPY

Low-resolution TEM were measured on a Libra 120 microscope operating at 120kV. SEM were measured on a Hitachi S-5500 STEM operating at 5.0kV in Secondary Electron mode.

FILM DEPOSITION

Conductive mesoporous films of colloidal TiO_2 NCs were prepared by spin coating and annealing solutions of ligand-stripped NCs. The oleic acid ligands bound to the surface of the colloidal NCs upon synthesis were removed, according to a procedure adapted from Dong *et al.*[90], by adding the NC solution to a two-phase mixture of N,N-dimethylformamide (DMF) and hexane. Then, roughly 1 mg of nitrosonium tetrafluoroborate ($NOBF_4$) was added and the resulting mixture was sonicated for 30 minutes, or until complete phase segregation of the ligand-stripped NCs was achieved. The NCs, now free of organic capping ligands and weakly coordinated to DMF molecules, were washed by precipitation with toluene and redispersion in DMF, repeated three times. A final NC solution of roughly 60 mg TiO_2 mL^{-1} in a 4:1 mixture of acetonitrile:DMF was prepared from the ligand stripped particles. For film deposition on either ITO-coated glass or silicon wafers, the substrate was first washed in chloroform, then acetone, then isopropanol to improve film adhesion. Films of roughly 100-200nm were prepared by spin coating the polar NC solution on the cleaned substrates, followed by annealing under Argon for 30 minutes at 300°C to remove organics. The most uniform films were obtained by preparing films immediately after ligand stripping. The thickness and uniformity of the TiO_2 films were measured with a Veeco Dektak 150 profilometer.

ELECTROCHEMISTRY

Electrochemical measurements were taken with a Biologic VMP3 potentiostat. *In situ* transmission spectra were recorded through the NC film working electrode an ASD LabSpec4 spectrometer across a spectral window of 400-2200 nm, limited by strong absorption bands from the liquid electrolytes. Both intercalating (LiTFSI) and non-intercalating (TBATFSI) electrolyte salts were vacuum baked at 150°C for 12 hours, and tetraglyme was dried with a molecular sieve, to remove residual water prior to preparing the electrolyte solutions. For experiments using a fixed applied potential, the working electrode was held at the applied potential until the current equilibrated to a constant value due to a minor leakage current, usually after a time span of roughly one hour.

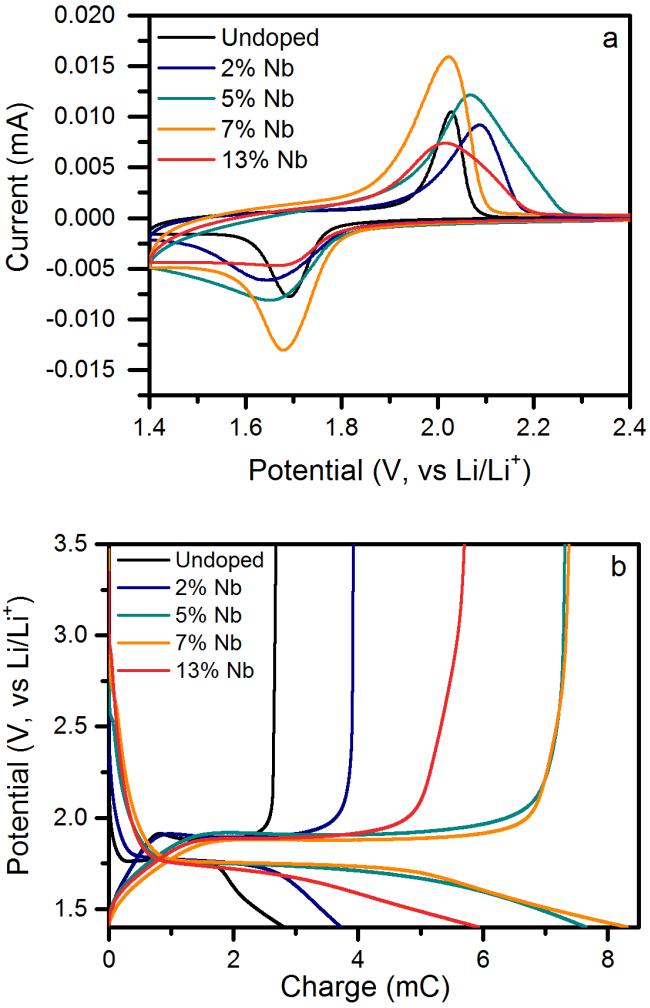

Figure A1 Electrochemical cycling of TiO_2 NC films.

A series of Nb-TiO_2 NC films were tested in a) cyclic voltammetry at 0.5 mV/s and b) galvanostatic charging experiments at a rate of roughly 1C measured empirically from CV data in a). The electrolyte was 0.1M LiTFSI in tetraglyme. All films were had a thickness of 130nm ± 35nm and charged within a constant-area (0.5 cm^2) cell sealed by an O-ring inside an argon glovebox.

PHASE TRANSITIONS UPON LITHIATION

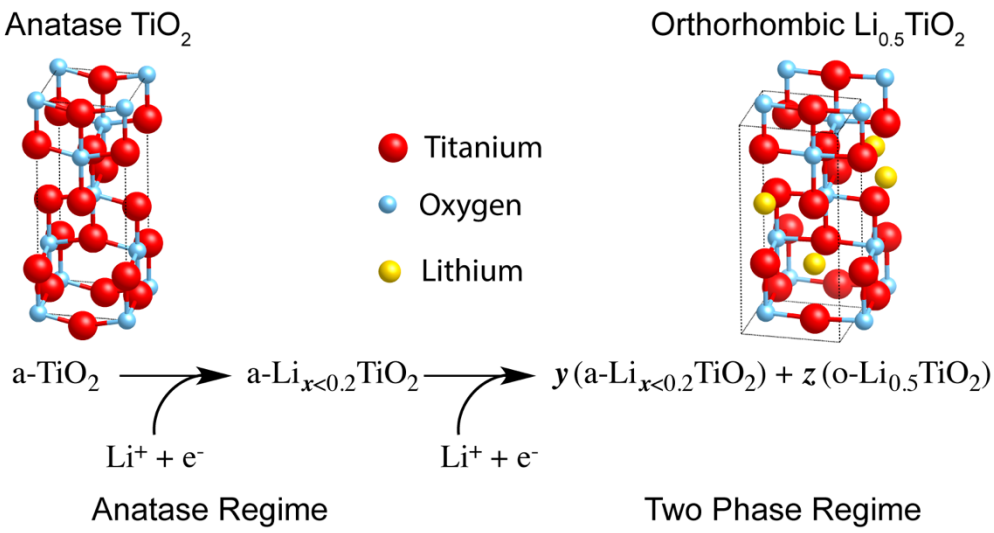

Figure A2 Schematic of lithiation phase transformation in TiO_2.

A discrete phase change from anatase to orthorhombic $Li_{0.5}TiO_2$ occurs upon sufficient lithiation, resulting in a two-phase regime.

X-RAY DIFFRACTION

The XRD patterns shown in **Figure 2.3** show phase transitions upon reduction during a single charging cycle. The patterns shown below, in **Figure A3**, show phase behavior upon charging and discharging for two cycles. The phase transition is clearly reversible for both anatase and 10% Nb-TiO_2 NC films. The noisy patterns for as-deposited undoped TiO_2 and the sharp peak at 2.3$Å^{-1}$ are attributed to experimental noise from the baselining procedure used to subtract silicon diffraction from the TiO_2 NC patterns. Transmission and grazing incidence XRD patterns were collected with a 2D area detector, and diffraction patterns were averaged across the measured range of the 2D detector, i.e. assuming isotropic scattering. The beam energy for transmission WAXS was calibrated using a reference sample of LaB_6, and had a wavelength of 0.9744Å. The detector distance was 200mm.

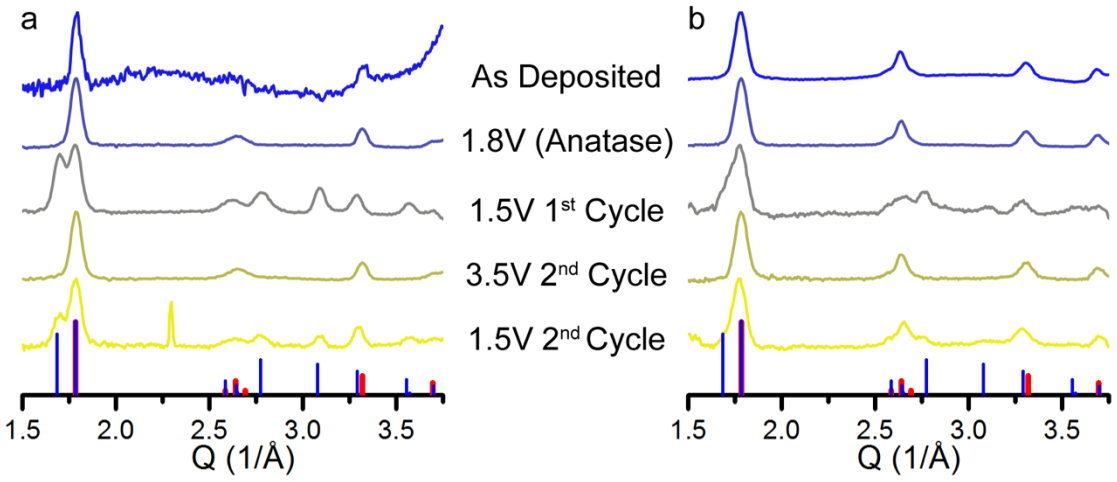

Figure A3 Transmission wide-angle XRD spectra of charged TiO_2 films.

a) undoped and b) 10% Nb-TiO_2 NC films, for a range of electrochemical charging potentials. Films were electrochemically cycled in 0.1M LiTFSI in tetraglyme. The as-deposited and partially-reduced 1.8V patterns match the anatase structure ($I4_1/amd$, ICSD Coll. Code 96946, red), and the fully reduced 1.5V pattern corresponds to the $Li_{0.5}TiO_2$ phase (Imma, ICSD Coll. Code 96948, blue), reported for microscale anatase TiO_2[92].

A second series of synchrotron XRD experiments were performed at beamline 11-3 of SSRL in grazing incidence mode to observe the phase transitions of the NC film upon oxidation, as shown in **Figure A4**. Films were deposited on a silicon substrate coated with 10nm of gold, and electrochemically charged by the same method as described for the transmission WAXS samples. Charged films were then transferred air-free to a helium-filled glovebag attached to an enclosed, helium-atmosphere sample chamber. XRD spectra were recorded in grazing incidence geometry with an incident angle of 0.12 degrees to the substrate surface. The beam energy for GIWAXS was calibrated using a reference sample of LaB_6, and had a wavelength of 0.9744Å. The detector distance was 150mm. The

GIWAXS spectra have much broader peaks than the transmission mode data, but there is still clear evidence of a discrete phase change that occurs across the 1.8V lithiation threshold. In the oxidative direction, the 1.8V spectra for all four samples (red lines) have peaks that correspond to the orthorhombic $Li_{0.5}TiO_2$ phase, and match the profile of the 1.5V reduced spectra. However, the oxidative 1.8V spectra are all broader than the 1.5V spectra, with some evidence of delithiation, indicating that there may be a partial transition to anatase upon oxidation from 1.5V to 1.8V.

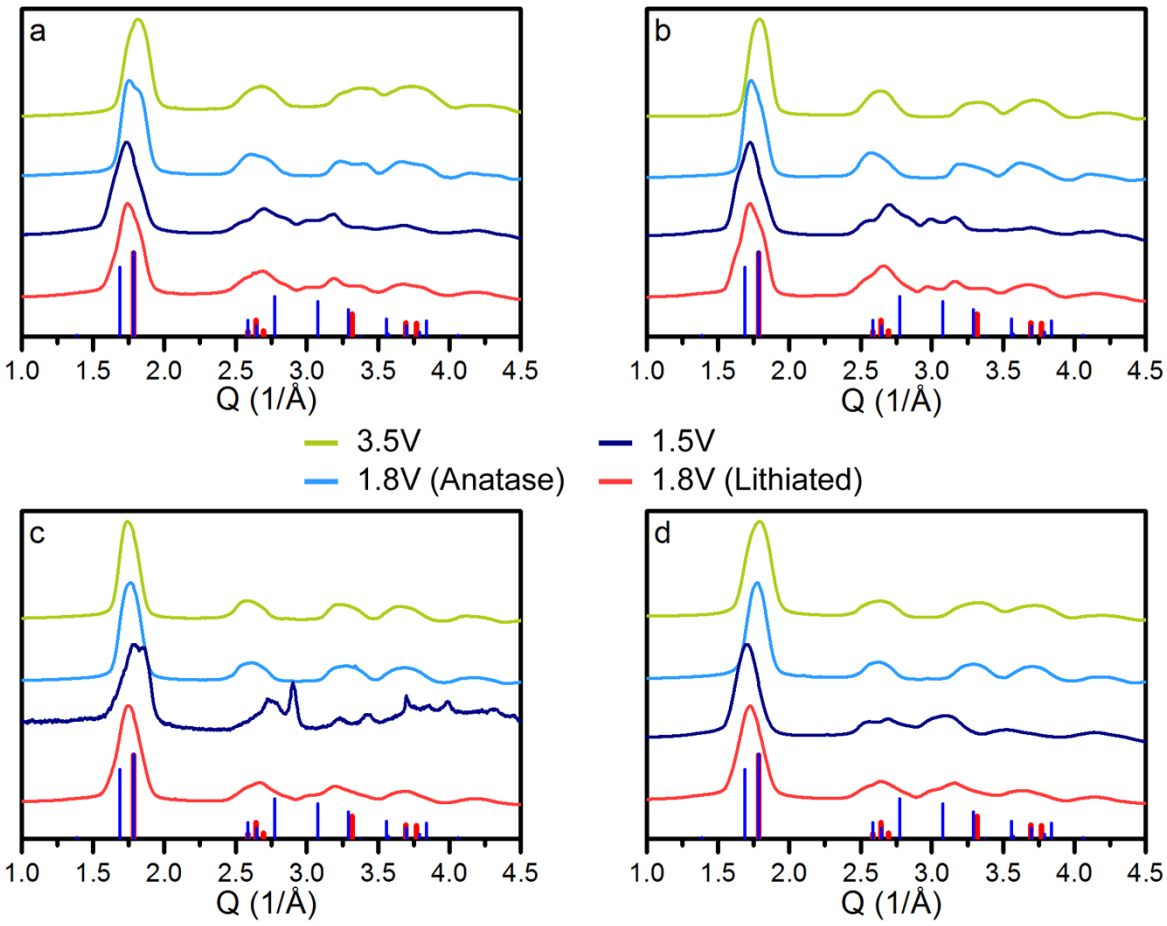

Figure A4 Grazing-Incidence wide angle XRD spectra of charged TiO_2 films. a) undoped, b) 2.5% Nb, c) 9% Nb and d) 19% Nb-TiO_2 NC films, electrochemically charged to four different potentials. Films were electrochemically cycled in 0.1M LiTFSI in tetraglyme. The as-deposited and partially-reduced 1.8V patterns match the anatase structure ($I4_1/amd$, ICSD Coll. Code 96946, red), and the fully reduced 1.5V and partially-oxidized 1.8V patterns correspond to the $Li_{0.5}TiO_2$ phase (Imma, ICSD Coll. Code 96948, blue), reported for microscale anatase TiO_2[92].

X-RAY ABSORPTION SPECTROSCOPY

The XANES pre-edge spectra in **Figure 2.5** and **Figure 2.6** were obtained from full Ti K-edge XAS spectra at beamline 10.3.2 of ALS. Energy was calibrated by measuring transmission X-Ray absorption through a titanium foil, and by fitting the maximum of the first derivative at the Ti K-edge to 4966.4 eV[172]. More details about the beamline are reported by Marcus *et al*[173]. The main edge features and extended structures are presented in **Figure A5** below. The edge shift upon electrochemical lithiation is clearly visible in the undoped TiO_2 charging experiment, along with changes in the extended structure, as expected for a bulk phase transition. Nb-TiO_2 charging experiments yielded similar results. A comparison of the as-deposited XAS spectra of the Nb-TiO_2 NCs reveals that there is a slight deviation in the extended structure and peak profiles for high doping contents. However, there is no appreciable shift in the main edge energy upon any level of Nb doping, as shown in the first derivative plot (**Figure A5c**).

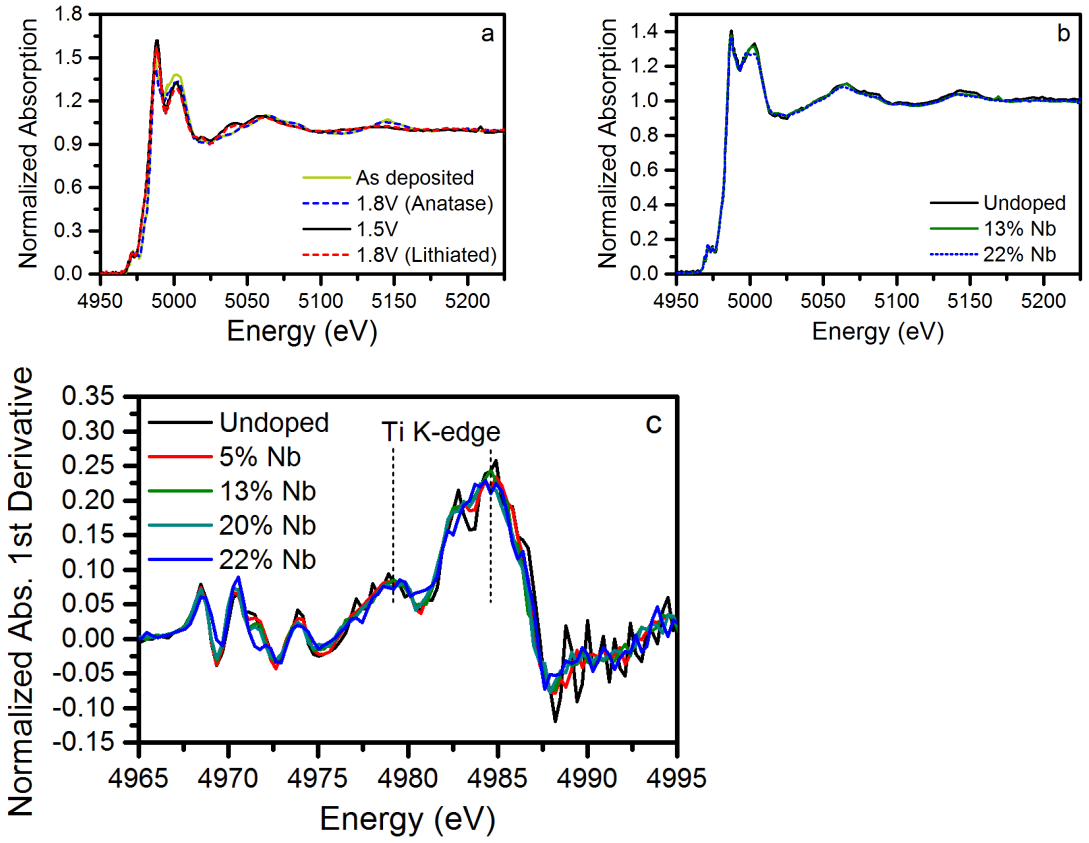

Figure A5 X-Ray Absorption Spectra of charged TiO_2 films at the Ti K-edge. a) undoped TiO_2 NC films electrochemically charged to a range of potentials, b) as-deposited (uncharged) NC films for a range of Nb doping content. c) A plot of the 1st derivative of the Ti K-edge for as-deposited NC films with a range of Nb doping shows the position of the main edge energy.

SPECTROELECTROCHEMISTRY

The results of *in situ* spectroelectrochemical measurements of film transmittance are reported in terms of the change in Optical Density (ΔOD) of the film upon charging. This metric is a measurement of extinction, baselined to the total extinction of the as-deposited film. The undoped and Nb-TiO_2 NC films darken upon reduction across most of the recorded spectral region, so the ΔOD graphs presented in the main text and below

demonstrate positive changes in the extinction of the film upon reduction. There was minor variation in film thickness between different samples, so extinction was normalized with respect to film thickness to enable a quantitative comparison. The conversion from transmittance to normalized ΔOD data is visualized in **Figure A6**.

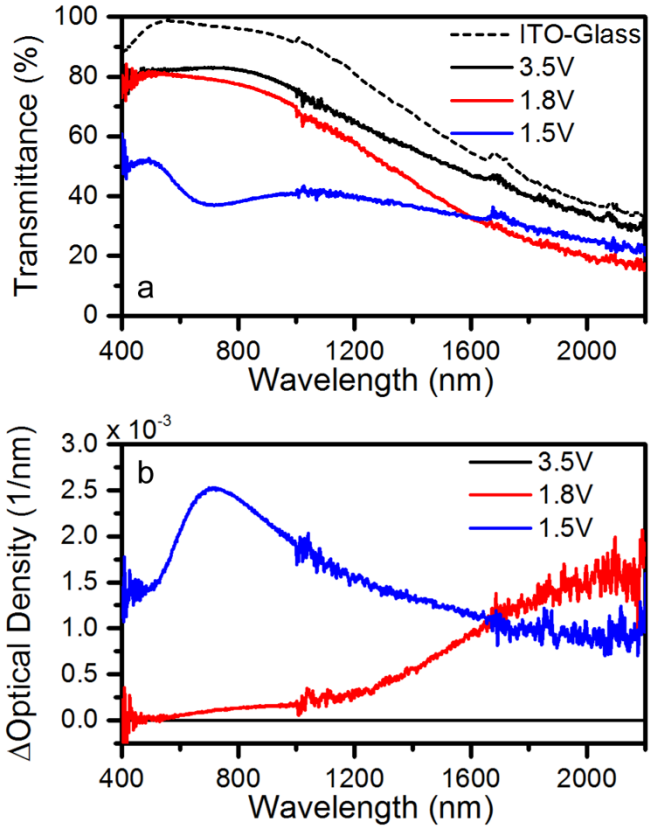

Figure A6 *In situ* spectroelectrochemical data of a TiO_2 NC film.

Spectra of a 140nm thick 8% Nb-TiO_2 NC film deposited on an ITO-glass substrate, as a) transmittance and b) thickness normalized extinction spectra showing modulation from the fully oxidized state (3.5V). Films were electrochemically cycled in 0.1M LiTFSI in tetraglyme.

Optical switching was compared across a broad range of Nb doping to assess the tunability of the electrochromic effect in these films. All films were within 60 nm of

160nm thickness, and electrochemically cycled following the same methods described for the *in situ* results presented in **Figure 2.4** of the main text. The modulation achieved at each of the four electrochromic modes was compared by measuring the normalized ΔOD at a set of reference wavelengths for all of the measured films. There were no discernable trends in measured ΔOD of the 'Warm' (1.8V upon oxidation, $Li_{0.5}TiO_2$) and 'Dark' (1.5V, $Li_{0.5}TiO_2$) modes with varying Nb doping, but the capacitively reduced 'Cool' mode (1.8V upon reduction, anatase TiO_2) shows positive correlation with Nb content. A plot of ΔOD at three reference NIR wavelengths – 1000nm, 1500nm and 2000nm – for capacitively reduced 1.8V 'Cool' mode films is presented in **Figure A7**. There appears to be a maximum in modulation of the NIR extinction for about 7% Nb doping.

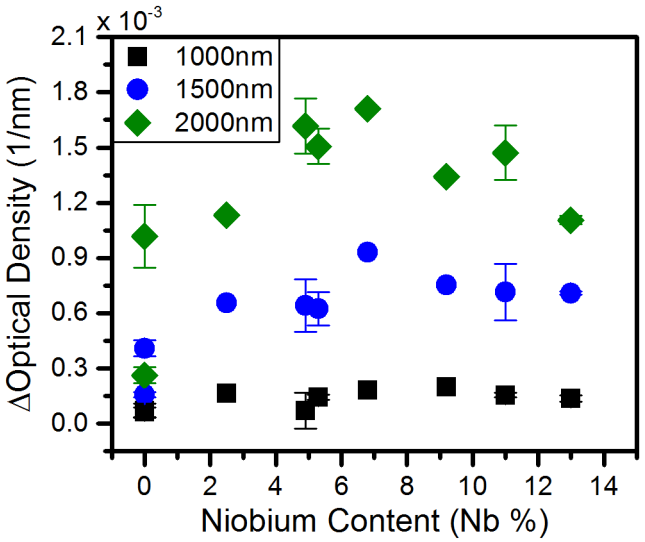

Figure A7 A plot of thickness-normalized ΔOD vs. Nb doping content.

Recorded for NC films capacitively reduced to 1.8V (the 'Cool' mode), shown for three different NIR wavelengths. The error bars represent the standard deviation in ΔOD values for NCs that were prepared in duplicate or triplicate films. The data points without error bars show NCs that were not cast into multiple films to test for error, but they likely demonstrate similar measurement errors.

Mid-IR extinction measurements of the charged NC films were taken with a Bruker Vertex 70 FTIR spectrometer. FTIR spectra of both as deposited (nominally 3.5V) and capacitively reduced films (1.8V upon reduction) were recorded. To avoid oxidation due to air exposure, FTIR spectra were obtained immediately after removing the cell from the glovebox using a rapid transmission-mode scan lasting roughly 2 minutes. Mild oxidation due to air exposure was observed upon air exposure of the air-free cell, so the extinction of the reduced samples is likely lower than would be expected. The TiO_2 film actually lowers the extinction of the substrate and air-free cell, perhaps by decreasing the reflectivity of the naked gold coating on silicon. Thus, to compare the extinction spectra across different doping levels and charge states, all spectra were baselined against the undoped, as deposited TiO_2 NC film. There was significant variation in film thickness during this experiment, so baselined extinction spectra were then normalized by thickness.

Nb Doping (% Nb)	Thickness (nm)
0%	435
5%	630
7%	1260
13%	1190

$$\text{Normalized Extinction} = \frac{\text{Ext. - Ext. (3.5V, Undoped } TiO_2\text{)}}{\text{Thickness / Thickness (Undoped } TiO_2\text{)}}$$

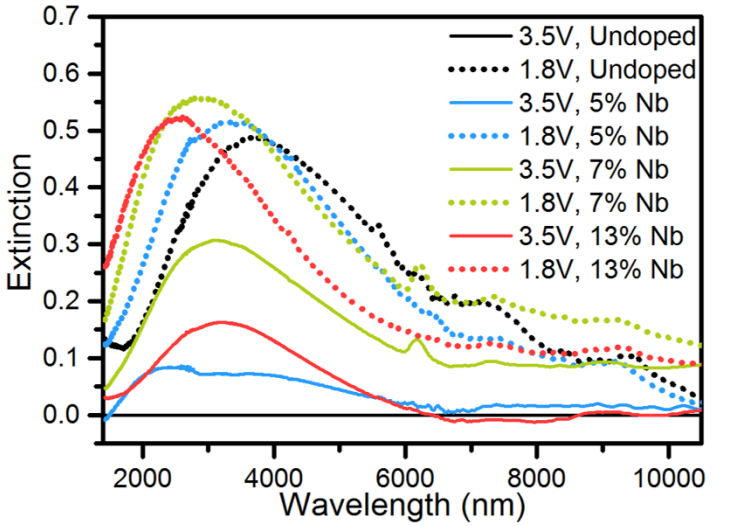

Figure A8 Thickness measurements and FTIR of *ex situ* charged TiO_2 NC films. A comparison of extinction of oxidized and capacitively reduced (1.8 V upon reduction) films for a range of Nb doping content. Spectra were baselined to the oxidized undoped TiO_2 film, and normalized by thickness.

Appendix 2: Supporting Information for Chapter 5

NANOCRYSTAL SYNTHESIS FOR BIXBYITE VANADIA NANOCRYSTALS

Bixbyite NCs were prepared following our previously described colloidal synthesis[162]. Briefly, vanadyl acetylacetonate (1 mmol) (Strem Chemicals, 98%), oleylamine (4 mmol) (Sigma Aldrich, 70%), oleic acid (4 mmol) (Sigma Aldrich, 90%), and squalane (8 mL) (Sigma Aldrich, ≥95%) were mixed and degassed at 110 °C. The suspension was then heated under nitrogen flow to 370 °C for 1 hour before cooling, followed by repeated washing with isopropanol and hexanes.

FILM PREPARATION

The cleaned NC ink (~50 mg/mL) was then deposited onto cleaned ITO coated glass substrates or doped silicon substrates via spin coating. Briefly, 20 μL of the NC ink was added to a 2x2 cm substrate, which was then spun at 1000 rpm for 90 s and dried at 4000 rpm for 30 s. Film thickness was determined to be 83 ± 3 nm using a Veeco Dektak 6M Stylus Profilometer, unless otherwise noted.

BIXBYITE TO VANADIUM DIOXIDE CONVERSION

The as-deposited bixbyite V_2O_3 NC film was then converted to monoclinic VO_2 by annealing in a slightly oxidative environment. In this study, the films were annealed in 167-250 ppm O_2 atmosphere for 30-60 minutes. The size of the VO_2 grains was controlled between about 20nm and 50nm diameter by varying the temperature of the annealing process. All films were annealed at 375°C unless otherwise noted.

PLANAR FILM PREPARATION

Planar films were prepared from vanadium oxide clusters previously described in the literature[167]. Briefly, ammonium metavanadate (0.5 mmol) (Sigma Aldrich, 99%) was dissolved in 12.5 mL of a 0.2 M oxalic acid solution (1:5 molar ratio) (Sigma Aldrich,

98%) and diluted to a total volume of 15.0 mL. Changing the volume of the oxalic solution added resulted in different vanadium oxide clusters (**Figure A21a**). After stirring for 72 hours, the blue solution was concentrated to ~2 mL using nitrogen gas flow. Excess oxalic acid crashed out of the solution and was removed by filtration. The remaining solution was dried completely and a 75 mg/mL solution was prepared in a 90% ethanol, 10% water solution. The solution was then spin coated onto cleaned ITO or silicon substrates at 3000 rpm for 60 s followed by a drying spin at 4000 rpm for 30 s. Immediately following spin coating, films were placed on a 90°C hot plate for 2 min. The films were then annealed in a slightly oxidative environment (167-250 ppm O_2) at 525°C for 1 hour to produce a brown tinted VO_2 film (**Figure A21c**), which was confirmed with XRD (**Figure A21d).** Planar VO_2 film thickness was determined to be 71 nm.

VARIABLE TEMPERATURE SPECTROELECTROCHEMISTRY

Electrochemical analysis of the VO_2 films was performed using a Bio Logic VMP3 Potentiostat. The VO_2 film was set as the working electrode, platinum foil as the counter electrode, and Ag/Ag^+ as the reference electrode. Note, the Ag/Ag^+ electrode was calibrated against a Li/Li^+ electrode and was found to be -3.00 V vs Li/Li^+. Voltages in this paper are reported relative to a NHE electrode. The three-electrodes were housed in a custom built cell that enabled a minimal pathlength through the electrochemical mediator consisting of 0.1 M tetrabutylammonium bis-trifluoromethanesulfonimidate (TBA-TFSI) (Sigma Aldrich, ≥99.0%) in propylene carbonate (Sigma Aldrich, 99.7%). Spectroscopy (400 – 2200 nm) was performed with an ASD Inc. PANalytical spectrometer operating in transmission mode, which was directed through the film using fiber optic cables. Finally, the temperature was controlled using a TC-720 temperature controller with a Peltier thermoelectric element with a center hole (TE Technologies) to enable light through the

system. The temperature was monitored with an epoxy bead thermistor (TE Technologies). For the experiments described in the main text, the entire VT-SEC set-up was housed in an argon glovebox (**Figure A9**). Experiments were also performed in air using a similar set-up outside the glovebox and bubbling the electrolyte with air for 2 hours.

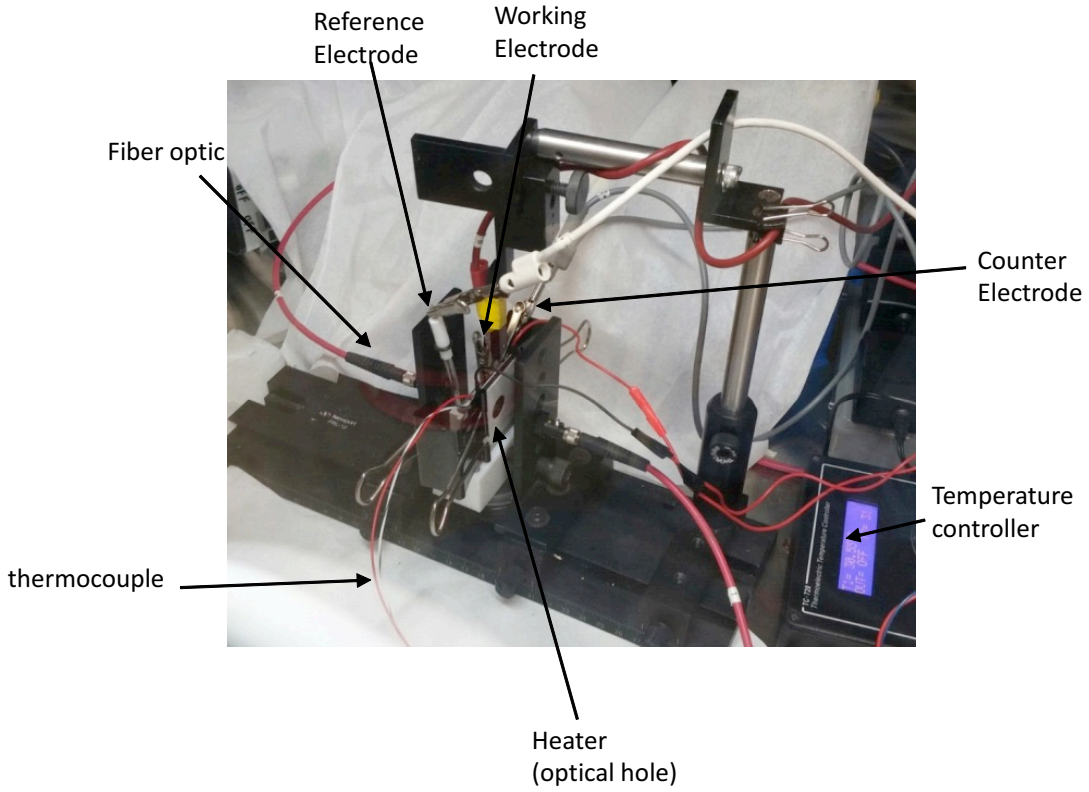

Figure A9: Optical image with labels for the VT-SEC setup.

The entire system was house in an argon glovebox to minimize any effects from oxygen and water. Experiments were also performed in an air environment (**Figure A14**) by moving the entire SEC set-up out of the glovebox.

ELECTROCHEMICAL PREPARATION OF SILICON SUPPORTED SAMPLES

The electrochemically darkened and bleached VO_2 states can be accessed by different time-potential-temperature trajectories, so a variety of preparations were studied to avoid ambiguity in our analysis. The darkening state was prepared with a small applied bias to avoid overshoot into the bleached state, while the darkened state was prepared to access the maximum decrease in IR transmittance. The partially bleached sample was accessed by applying a high, heated bleaching bias for half the time required to achieve complete IR bleaching. **Table A1** describes the complete list of sample preparations.

Sample Name	**Temperature**	**Bias Voltage *vs* NHE**	**Bias Time**
Monoclinic (R.T.)	25°C	unbiased	N.A.
Rutile (100°C)	100°C	unbiased	N.A.
Darkening	25°C	-0.5V	7.5 hrs
Darkened	25°C	-0.5V	17 hrs
Bleaching	25°C	-2V	30 min
Partially Bleached	100°C	-1.5V	5-20 min
Bleached	100°C	-1.5V	10-40 min

Table A1 A description of each of the sample preparations described in the study.

FOUR POINT PROBE RESISTIVITY MEASUREMENTS

The resistivity of VO_2 films was obtained by using the Van Der Pauw four point probe measurement geometry. Films were prepared by spin coating V_2O_3 NCs on high-resistivity glass substrates with a thin 30 nm layer of gold deposited as an electrode contact in an L-shaped area on the substrate. A 1 cm^2 bare glass region was retained in the corner of the film to allow for four point probe conductivity measurements after electrochemical

charging. The spin-coated film was annealed under the same conditions to produce VO_2 NCs for spectroelectrochemical measurements described previously. After biasing, the film was rinsed and dried, and the outside of the bare glass region was electrically isolated from the gold-coated region using a diamond scribe. Indium metal was pressed into each of the four corners of the bare glass region as metal contacts for the VO_2 film, and the film was transferred air-free to a N_2 glovebox containing the temperature-dependent four point probe measurement apparatus (**Figure A10**). All measurements were taken with a probe current of 10 μA, which was found to be within the Ohmic region. All samples were measured for resistivity across a temperature range of 30°C to 100°C and back in 5°C intervals to test for thermal effects.

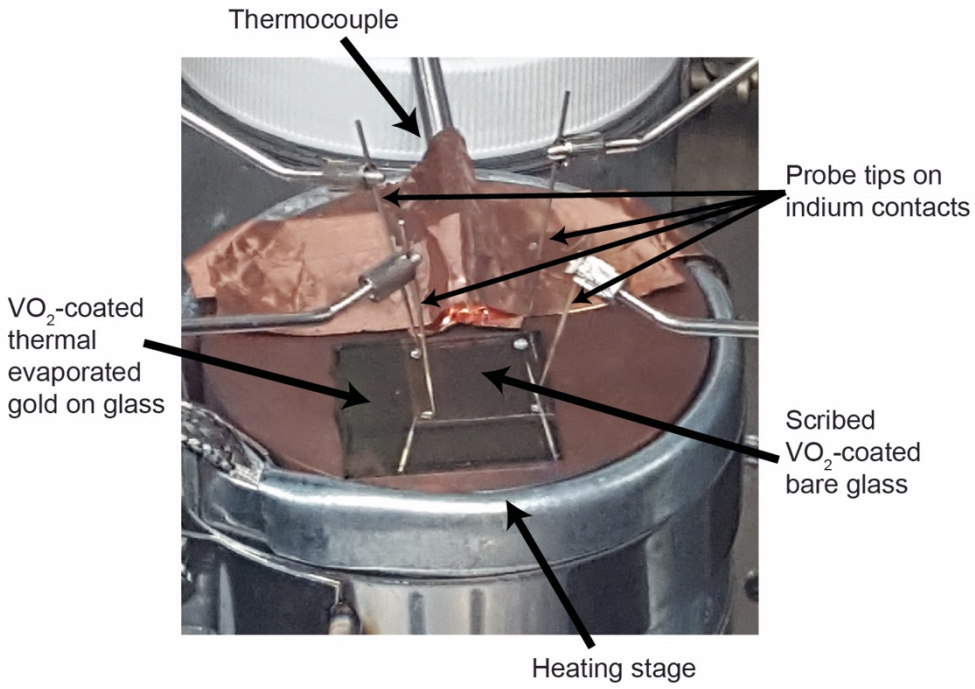

Figure A10 Temperature dependent resistivity measurement apparatus. Optical image with labels of the temperature dependent resistivity measurement set-up used in the manuscript. The entire apparatus was housed in a nitrogen glovebox to minimize exposure to oxygen and water.

ELECTRON MICROSCOPY

Transmission electron microscopy (TEM) micrographs were collected using a JEOL 2010F TEM with a Schottky field emission source operating at 200 kV. The sample was prepared by drop casting a dilute suspension on V_2O_3 nanocrystals in hexanes on a silicon nitride TEM grid. The TEM grid was annealed under the same conditions as films (375°C, 1 hr, 250 ppm O_2) to convert to VO_2 NCs. Scanning electron microscopy (SEM) micrographs were collected using a Hitachi S5500 scanning electron microscope operating at 20 kV accelerating voltage. The samples were prepared by drop casting films of V_2O_3

nanocrystals in hexanes on a silicon wafer and annealing them under the same conditions as used for equivalent VO_2 films.

RAMAN SPECTROSCOPY

Raman spectroscopy was performed on a Horiba Jobin Yvon LabRAM ARAMIS spectrometer using a 532 nm laser. Electrochemistry of the VO_2 films on doped silicon substrates was performed in a glovebox before transfer to the Raman instrument using a Linkam LTS420 cell. The Linkam cell not only prevented rapid oxygen contamination, but also enabled analysis at temperatures above and below the MIT temperature. Measurements were taken under a 50x long working distance microscope objective.

X-RAY DIFFRACTION

XRD for the V_2O_3 to VO_2 conversion characterization was performed using a Rigaku R-axis Spider diffractometer with an image plate detector and Cu Kα radiation. Films were prepared on silicon substrates and data was collected in reflection mode over 10 minutes of exposure. XRD for Scherrer analysis of crystallite grain size was measured using a Rigaku Miniflex 600 diffractometer with a Cu Kα X-ray source operating at 40 kV and 15 mA with a graphite monochromator. Multiple scans were collected between 2θ = 26° and 30° with a step size of 0.02° and scan speed of 1°/min.

GRAZING-INCIDENCE WIDE-ANGLE X-RAY SCATTERING

GIWAXS measurements were taken at beamline 7.3.3 of the Lawrence Berkeley National Laboratory Advanced Light Source, using a 10 keV synchrotron X-ray source. All measurements were collected at an incidence angle of 0.10 degrees. Silver behenate was used as a standard. The measurements reported in this study are radial sector averages between 4 degrees on either side of vertical (parallel to the beam and normal to the substrate) of the intensity measurements collected on a 2D detector roughly 30 cm from

the sample. Data processing, to convert from collected 2D images to 1D data, was performed using the Nika software suite[174]. The sector average was limited to a narrow slice to avoid averaging across distortions in Q-values caused by the grazing incidence geometry. Typically, GIWAXS measurements collected by a 2D detector are treated qualitatively because of geometric distortions in the isotropic Q values[175]. Accounting for the grazing incidence geometry is expected to introduce a non-linear shift in q-values, but the small incidence angle (0.10 degrees) and limited range of 2D averaging should make this effect quite minor, as expected from a comparison of the diffraction patterns of the monoclinic VO_2 films between WAXS data in **Figure 5.1** and GIWAXS data in **Figure 5.4** of the main text.

X-RAY ABSORPTION SPECTROSCOPY

XAS spectra were collected at beamline 10.3.2 of the Advanced Light Source. Vanadium K-edge spectra were collected in fluorescence mode using an Amptek silicon drift fluorescence detector 1-element (XR-100SDD) collected at ambient temperature (25°C) for all spectra except the rutile sample, which was heated to 100°C in air using a Peltier heating element affixed to the back of the sample substrate during measurements. The darkening, bleaching, and bleached films were electrochemically reduced then sealed with a mylar film in an argon glovebox before XAS measurement to prevent air exposure. A Si (111) monochromator was used with a resolving power (ΔE/E) of 7000 at 10 keV. More details about the beamline can be found in reference[173] of the supporting information. V K-edge EXAFS were collected in the energy range of 5360 to 5980 eV. Each XAS spectrum was averaged from two consecutive scans, each about 45 minutes long. The experimental data was energy calibrated to a vanadium foil measured in transmission mode. Preliminary analysis to scan average and background the pre- and post-

edge features was performed using software developed at ALS beamline 10.3.2, and normalization and post-processing of μ(E) data was performed using Athena and Artemis from the Demeter package (version 0.9.24)[176]. Extended X-ray Absorption Fine Structure (EXAFS) Fourier transforms were converted into real space with a Hanning window in the k-space range of 2.6-10.6 $Å^{-1}$. Complete XAS and k-space EXAFS data is presented in **Figure A19**.

EXPERIMENTAL SUPPORTING INFORMATION

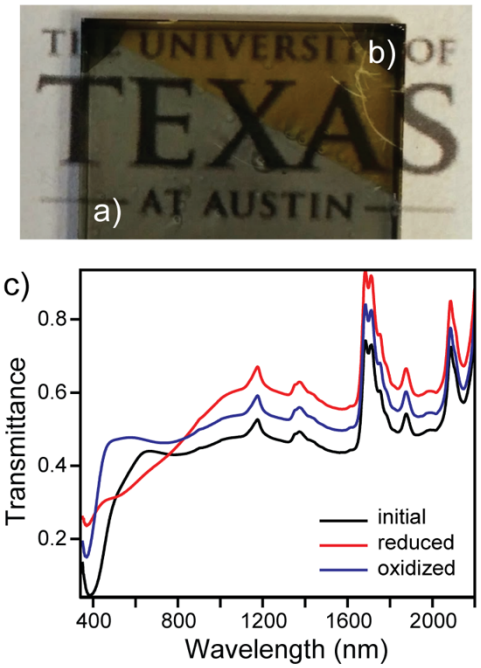

Figure A11 Optical image of a VO_2 NC film.

Image a) with and b) without electrochemical reduction in an electrolyte consisting of 0.1 M Li-TFSI. c) The electrochromic behavior in this case was irreversible as the Li^+ ions that intercalate into the VO_2 lattice are unable to deintercalate. Khan and co-workers observed similar behavior for VO_2 thin films using *ex situ* transmittance and conductivity measurements[163].

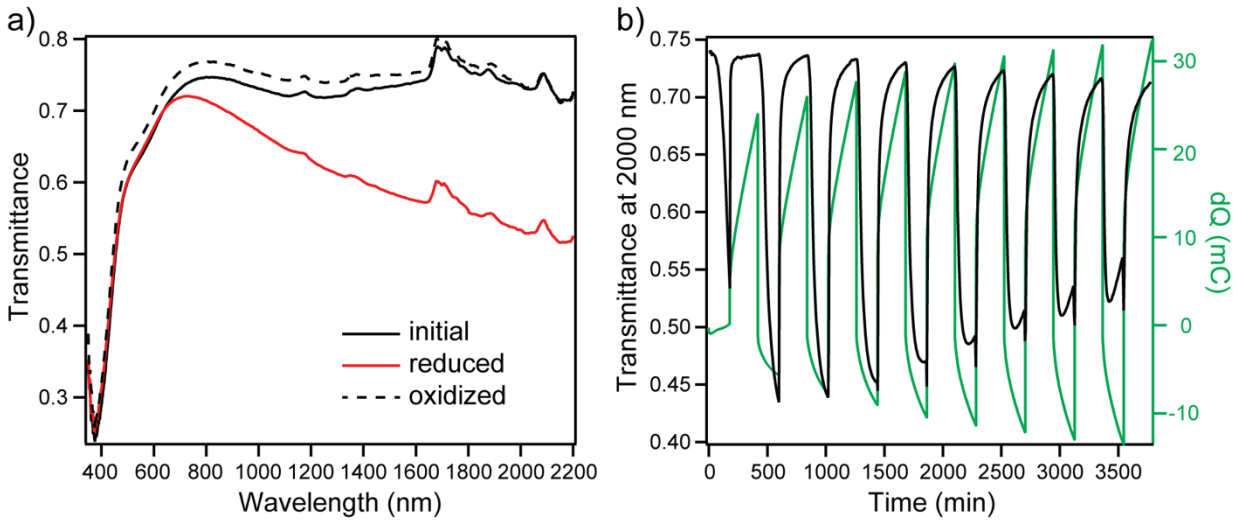

Figure A12 Transmittance during darkening transition of VO_2 film.

a) Transmittance as a function of wavelength at 30°C showing initial monoclinic state, darkened state (reduced at -1 V for 3 hours), and recovered monoclinic state (oxidized at +1 V for 4 hours). b) Transmittance at 2000 nm and charge as a function of time as film is cycled between -1V *vs* NHE for 3 hours and +1V *vs* NHE for 4 hours at 30°C.

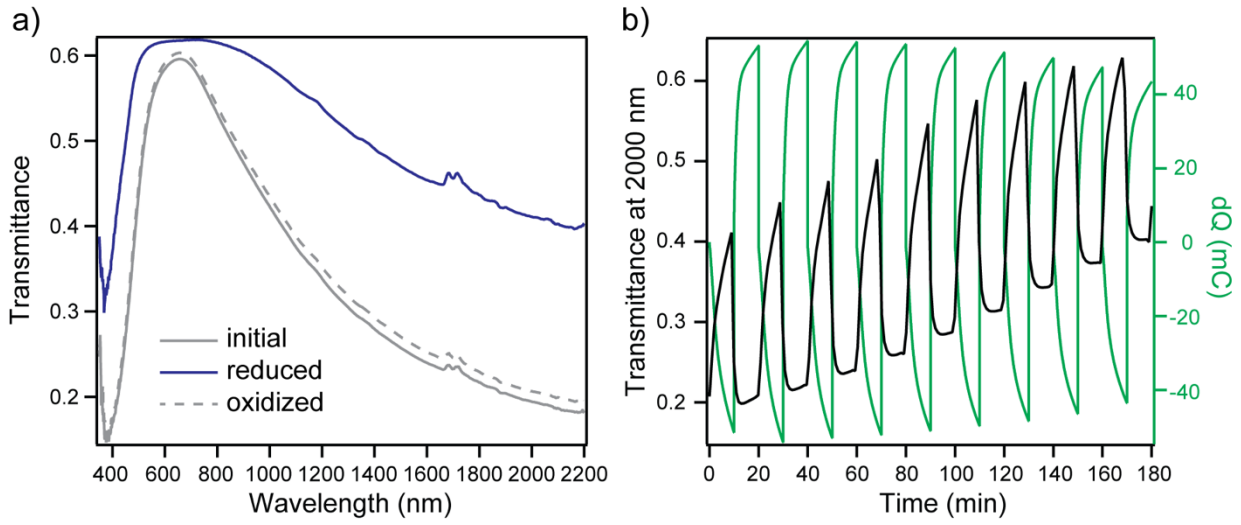

Figure A13 Transmittance during bleaching transition of VO_2 film at 100°C.

a) Transmittance as a function of wavelength at 100°C showing initial rutile state, bleached state (reduced at -1.5 V for 10 min), and recovered rutile state (oxidized at +1 V for 10 min). b) Transmittance at 2000 nm and charge as a function of time as film is cycled between -1.5V and +1V *vs* NHE for 10 minutes each at 100°C.

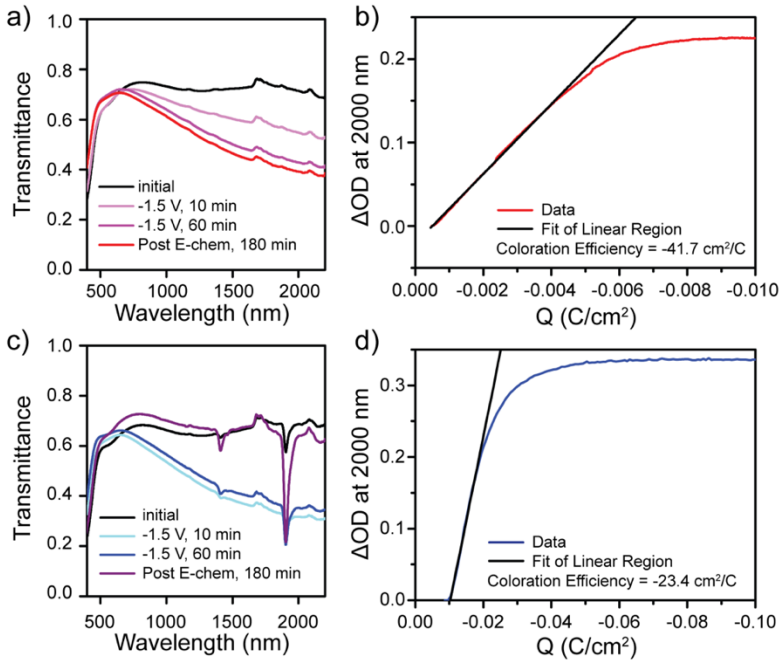

Figure A14 VO_2 electrochromism in an air and argon atmosphere.

Comparison of the electrochromic behavior of VO_2 NC films in an argon (a,b) or air (c,d) environment at 30°C. For experiments in an air environment, the 0.1 M TBA-TFSI electrolyte was bubbled with air for 2 hours. The coloration efficiency was determined by taking the slope of the linear portion of the curve in parts b) and d). While electrochromism was observed for films in both argon and air environments, when application of the reducing potential ended the NIR transmission slowly returned to its original state only in the air environment. We attribute this observation to the oxidation of the reduced state in the presence of oxygen. This oxidation process is further supported by the increase in charge by an order of magnitude but lower coloration efficiency for the air environment as the oxygen is continuously oxidizing the film during the reduction process, consuming a large part of the injected charge.

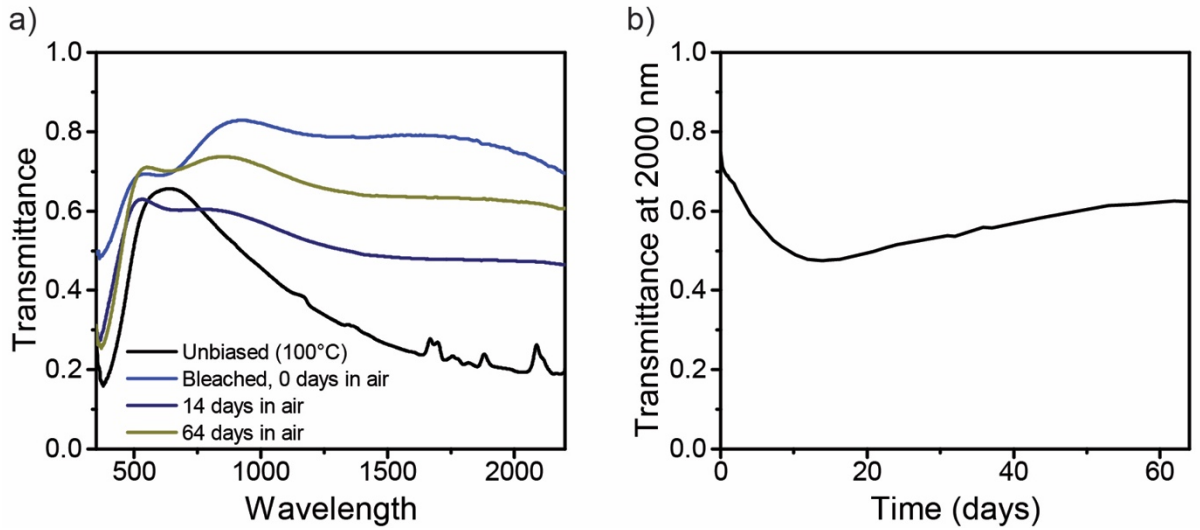

Figure A15 Oxidation of bleached VO_2 film when exposed to air.

a) Transmittance as a function of wavelength showing oxidation upon air exposure of a bleached film (reduced at -1.5V at 100°C for 10 min in an argon atmosphere). b) Transmittance at 2000 nm as a function of time during air exposure at room temperature. Note that the bleached film undergoes an initial darkening during air oxidation, similar to the insulator-metal-insulator transformation seen upon electrochemical reduction.

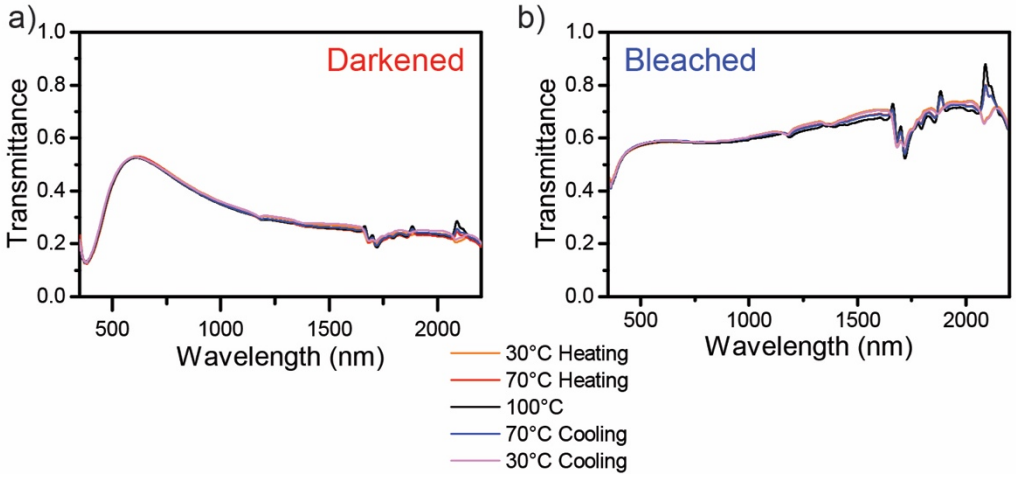

Figure A16 Temperature dependent optical transmittance of charged VO_2 films. Data for the a) bleached and b) darkened films measured in the resistivity measurements of **Figure 5.3** of the main text. During these optical measurements the films were immersed in 0.1M TBA-TFSI in PC, but no bias was applied.

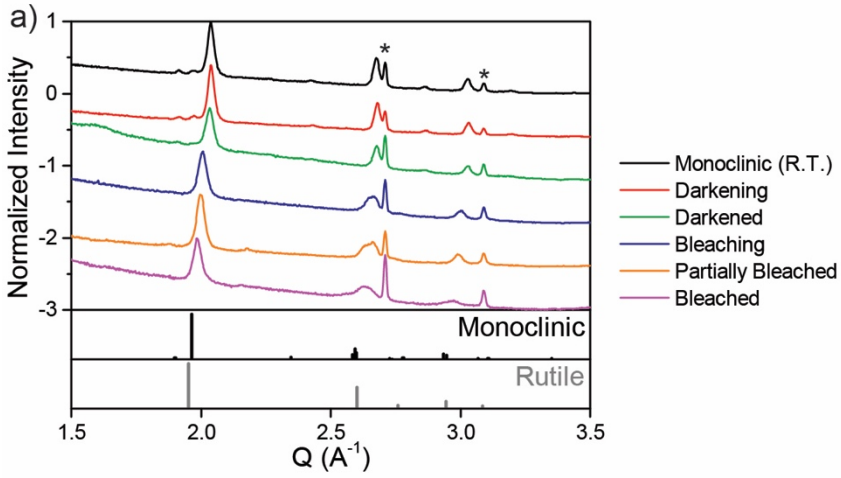

Figure A17 Complete GIWAXS measurements of charged VO_2 films.

a) The complete set of GIWAXS measurements taken of *ex situ* biased VO_2 NC films. b) Close-up plots of each of the main peaks in the GIWAXS data used to calculate a and c lattice parameters for a tetragonal pseudo-rutile structure, as well as schematics indicating each of these diffraction planes for rutile VO_2. The purple spheres are vanadium atoms and the red spheres are oxygen atoms. The VO_6 octahedron is highlighted with red planes, and each marked Miller plane is highlighted in a unique color. The marked (*) peaks in the GIWAXS data arise from background aluminum in the sample stage.

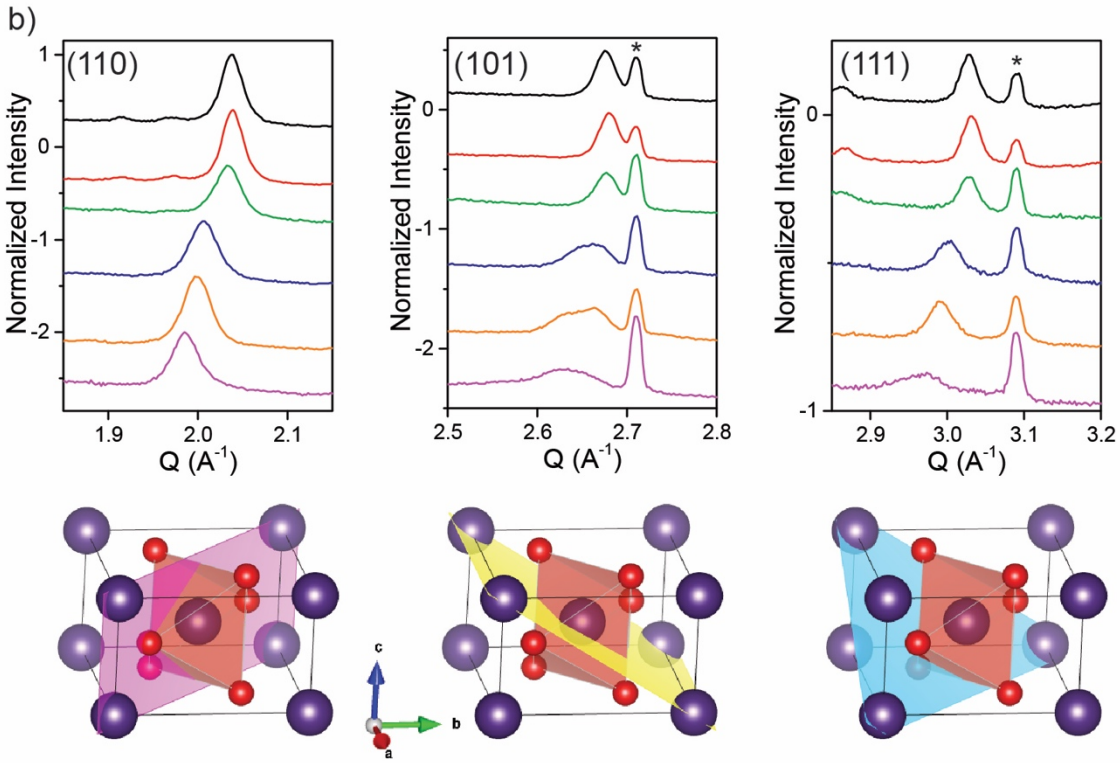

Figure A17 (continued)

Tetragonal geometry: $a = \sqrt{2}d_{110}$; $c = \frac{ad_{101}}{\sqrt{a^2 - d_{101}^2}} = \frac{ad_{111}}{\sqrt{a^2 - 2d_{111}^2}}$

	(110)		(101)		(111)	
Sample	d-spacing (Å)	a param. (Å)	d-spacing (Å)	c param. (Å)	d-spacing (Å)	c param. (Å)
Unbiased R.T.	3.08	4.36	2.35	2.79	2.07	2.81
Darkening	3.08	4.36	2.34	2.78	2.07	2.80
Darkened	3.09	4.37	2.35	2.78	2.08	2.80
Bleaching	3.13	4.43	2.36	2.79	2.09	2.82
Partially Bleached	3.14	4.44	2.37	2.80	2.10	2.82
Bleached	3.16	4.47	2.39	2.82	2.12	2.85

Table A2 Measured d-spacing for each of the primary pseudo-rutile peaks in VO_2. Determined by fitting Voigt peaks to GIWAXS patterns. The calculated tetragonal lattice parameters, as well as the geometric equations used to calculate them, are included as well. A tetragonal structure was used as a simple model to compare expansion in different lattice directions, even though the samples may have monoclinic distortions. The discrepancy between calculated c parameters from the measured (101) and (111) peaks may be due to distortions from the tetragonal structure or grazing-incidence geometry distortions in measured Q values.

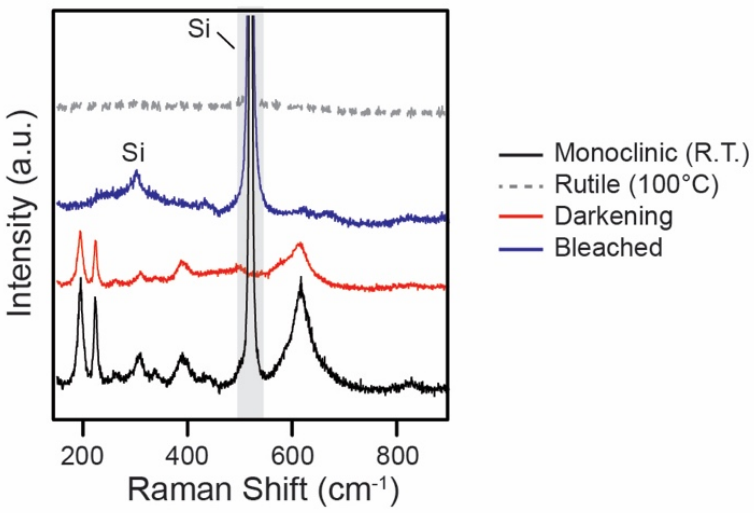

Figure A18 Raman spectroscopy of VO_2 films.

At low temperature for the unbiased VO_2 film, peaks indicative of the monoclinic (M1) phase are apparent due to asymmetric V-O bonding in the V-V dimerized unit cell. As the film is heated, VO_2 transforms to the more symmetric rutile phase and these peaks decrease in intensity and eventually disappear, consistent with previous Raman studies on VO_2 nanostructures[177-179]. *Ex situ* air-free Raman spectra of-the darkening state contains peaks that index to the monoclinic phase. This is in agreement with Jeong and co-workers finding that V-V dimerization, an identifying feature of the monoclinic phase, is maintained upon electrochemical metallization and is also consistent with recent Raman studies on ionic liquid gated VO_2 thin films[47,164,180]. On the other hand, the bleached state has no obvious Raman peaks, besides those which index to the underlying silicon substrate. This absence of peaks is consistent with GIWAXS data suggesting an increase in structural symmetry and conversion from the monoclinic phase to a more tetragonal rutile-like phase in the bleached state.

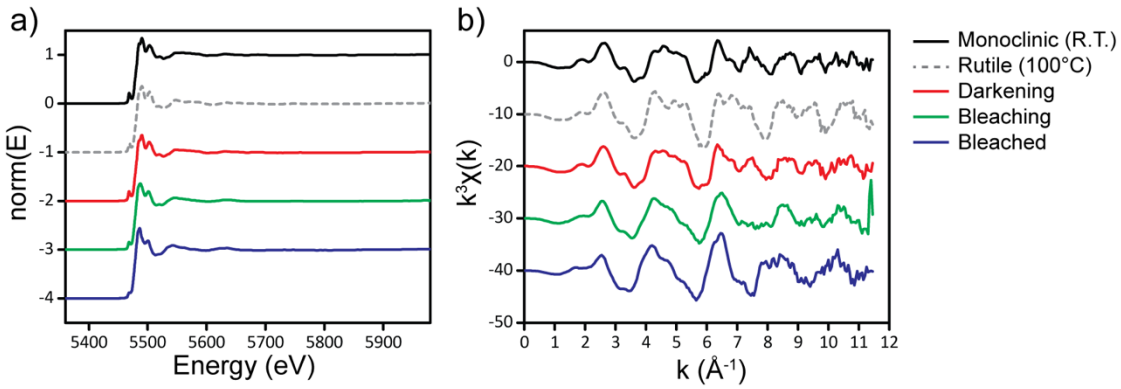

Figure A19 XAS and EXAFS data for charged VO_2 films.

a) Normalized XAS data and b) k^3 EXAFS data for monoclinic, rutile, darkening, bleaching, and bleached states of *ex situ* biased VO_2 NC films.

Sample	1st Derivative Max. (eV)	V Oxidation State
Monoclinic in air (25°C)	5482.34	4.00
Rutile in air (100°C)	5482.64	4.12
Darkening	5482.02	3.87
Bleaching	5481.13	3.52
Bleached	5480.62	3.32

Table A3 Results of V-K edge XAS measurements of VO_2 films.

The table shows the maximum first derivative of the V K-edge and calculated vanadium oxidation state (formal valency) according to the linear relationship between edge shift from monoclinic VO_2 and oxidation state described by Wong *et al*[166]. The linear function used was: (V Oxidation State) = 0.393*(Edge shift from monoclinic 1st derive. Max) + 4 .

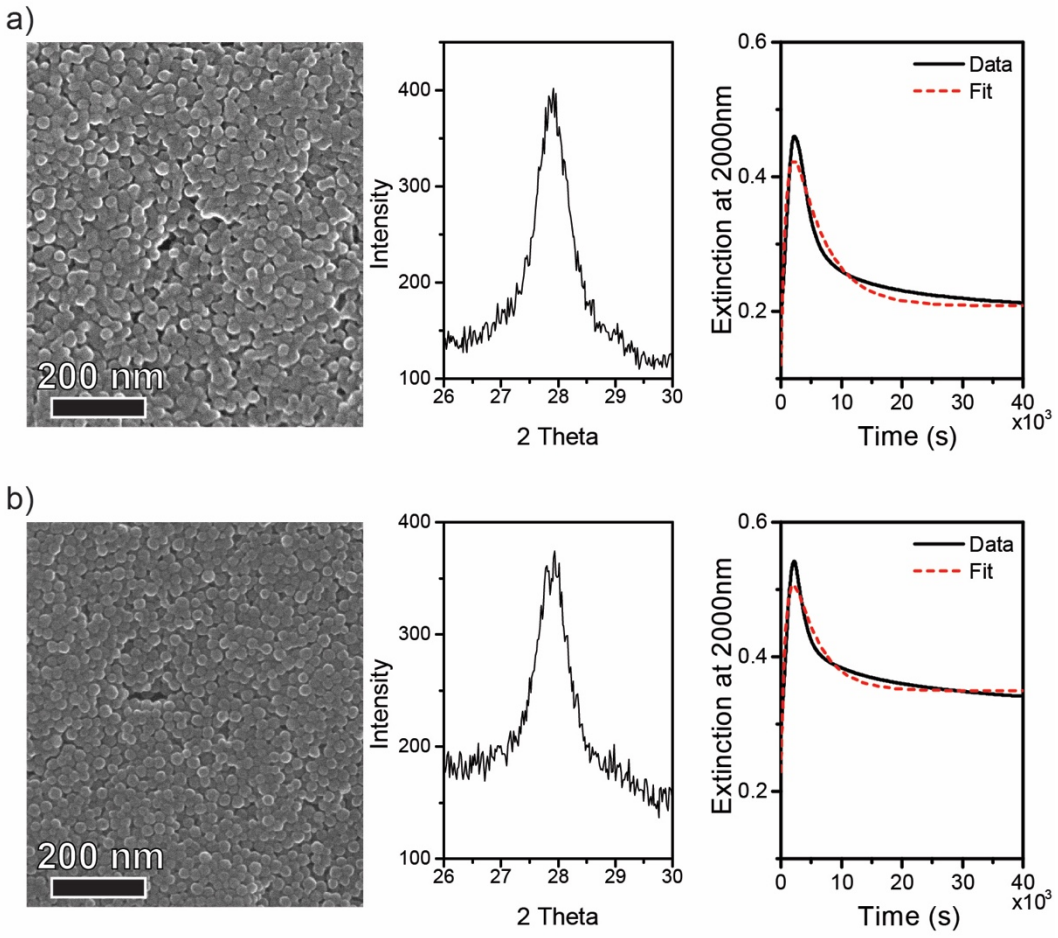

Figure A20 Size characterization of nanocrystalline VO_2.

SEM micrographs, WAXS diffraction patterns of the monoclinic (011) peak used for Scherrer crystallite size analysis referenced against a LaB_6 standard, and extinction at 2000 nm measured against time during charging at -1.5 V in 0.1 M TBA-TFSI in PC in argon atmosphere at 25°C for nanocrystal domain sizes: a) 23 nm, from annealing at 362°C, b) 25 nm, from annealing at 362°C, c) 35 nm, from annealing at 375°C, d) 38 nm, from annealing at 400°C, and e) 50 nm, from annealing at 400°C. All films were 118 +/- 12 nm thick.

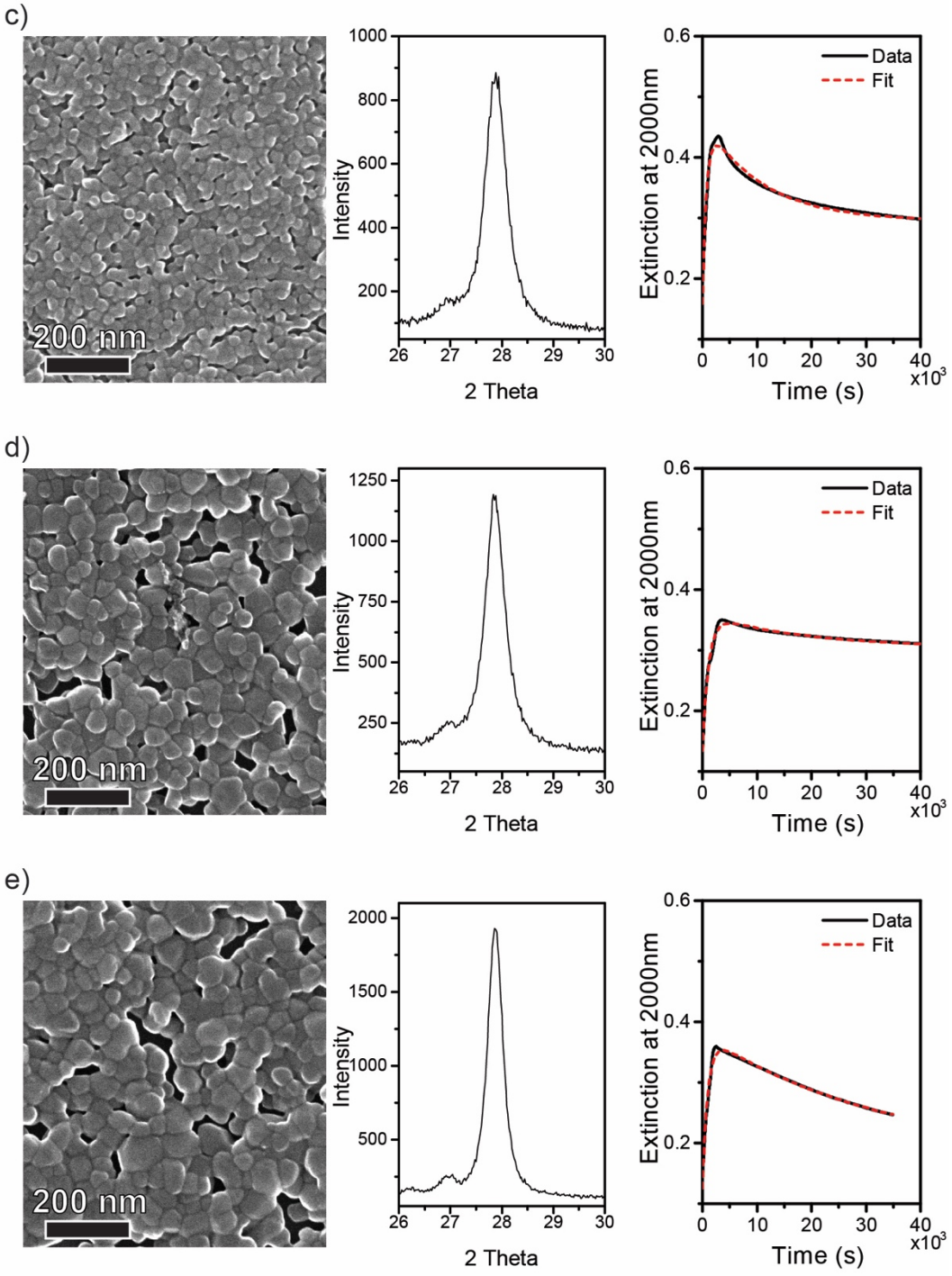

Figure A20 (continued)

$$Extinction_{2000nm}(t) = -a_{dark} \exp\left(-\frac{t}{\tau_{dark}}\right) + a_{bleach} \exp\left(-\frac{t}{\tau_{bleach}}\right) + a_{offset}$$

Crystallite Size	a_{dark}	a_{bleach}	a_{offset}	τ_{dark} (s)	τ_{bleach} (s)
23.8 nm	0.481	0.395	0.208	901	5150
25.2 nm	0.439	0.319	0.349	854	4190
34.8 nm	0.307	0.171	0.295	755	10757
38.5 nm	0.226	0.057	0.304	1124	18638
50.7 nm	0.255	0.205	0.176	981	33044

Table A4 Results of two-exponential model of extinction during transitions in VO_2. Fitted parameters for the two-exponential model of extinction at 2000 nm vs. time upon darkening and bleaching, as described by the equation above. Plots of the fitted model and experimental data are shown in the extinction vs. time plots in **Figure A20**.

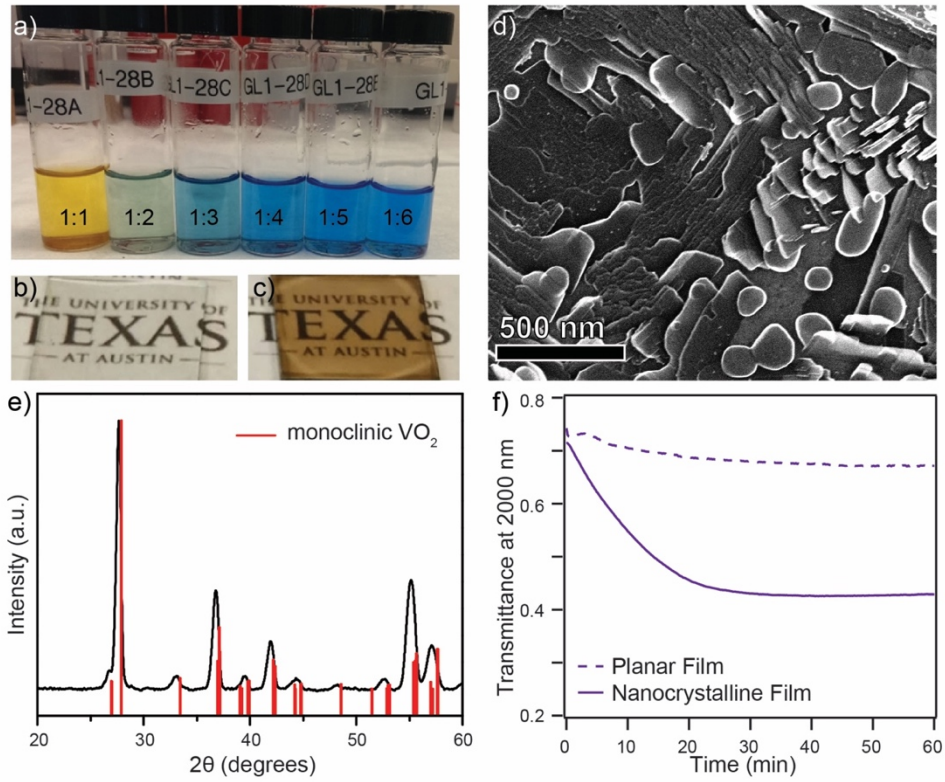

Figure A21 Cluster-synthesized planar VO_2 film characterization.

Characterization of VO_2 films prepared from molecular clusters to generate planar films. a) Optical images of vanadium oxide molecular clusters prepared from various ratios of ammonium metavanadate and oxalic acid. Films prepared by spin coating onto conductive substrates b) before and c) after annealing at 525°C under partial oxygen pressures. d) SEM micrograph and e) XRD scan of the film after annealing. f) Comparison of the NIR modulation kinetics upon charging at -1.5 V *vs* NHE in 0.1 M TBA-TFSI in PC electrolyte at 25°C in argon, between a planar film of VO_2 (dashed) and a VO_2 NC film (solid line), both on ITO-coated glass substrates.

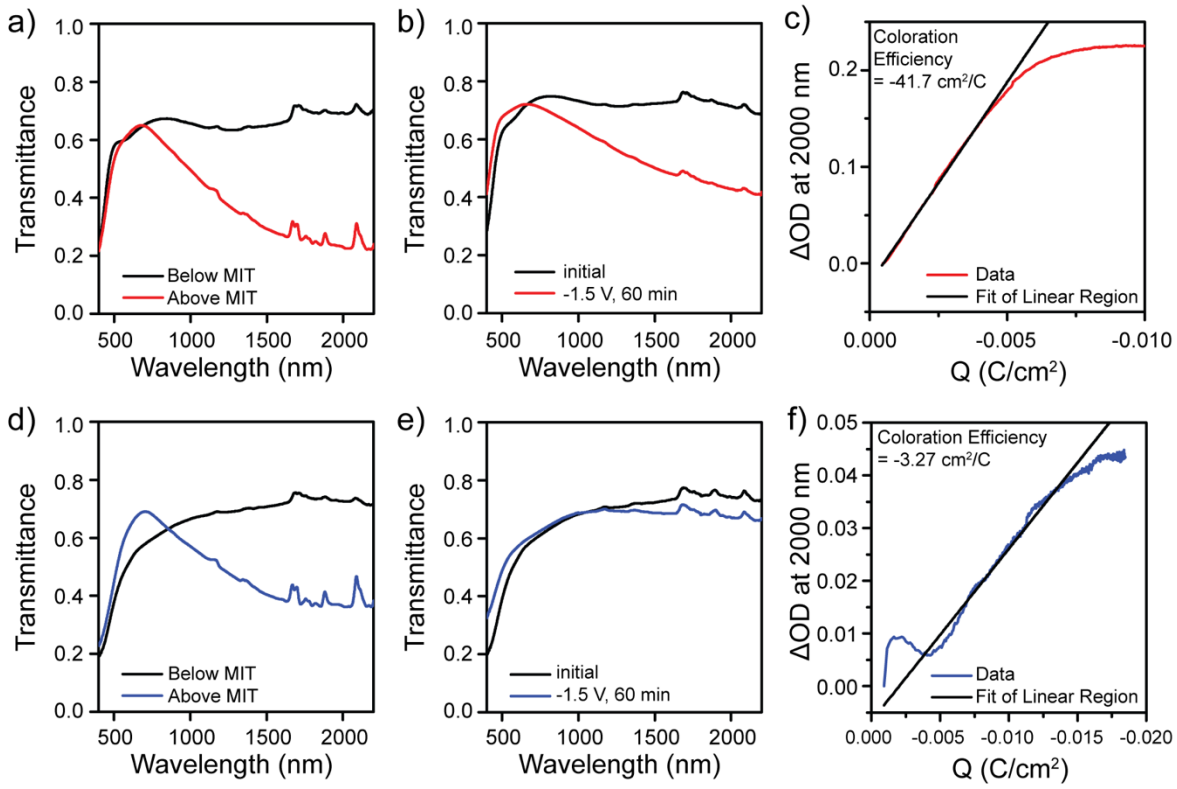

Figure A22 Thermochromic and electrochromic response of planar VO_2 films. Comparison of the thermochromic (a,d) and electrochromic (b,c,e,f) properties of nanocrystalline (a-c) and planar (d-f) VO_2 films. This data demonstrates the enhanced electrochromic behavior of the VO_2 NC films compared to the planar VO_2 films.

References

1. Busch, G. Early history of the physics and chemistry of semiconductors-from doubts to fact in a hundred years. *Eur. J. Phys.* **10,** 254–264 (1989).
2. Rao, C. N. R., Thomas, P. J. & Kulkarni, G. U. *Nanocrystals: Synthesis, Properties and Applications*. **95,** (Springer Science & Business Media, 2007).
3. Steigerwald, M. L. & Brus, L. E. Semiconductor crystallites: a class of large molecules. *Acc. Chem. Res.* **23,** 183–188 (1990).
4. Mayer, K. M. & Hafner, J. H. Localized Surface Plasmon Resonance Sensors. *Chem. Rev.* **111,** 3828–3857 (2011).
5. Chen, T. *et al*. Metal-insulator transition in films of doped semiconductor nanocrystals. *Nat. Mater.* **15,** 299–303 (2016).
6. Ranade, M. R. *et al*. Energetics of nanocrystalline TiO_2. *Proc. Natl. Acad. Sci. U.S.A.* **99,** 6476–6481 (2002).
7. Yin, Y. & Alivisatos, A. P. Colloidal nanocrystal synthesis and the organic–inorganic interface. *Nature* **437,** 664–670 (2005).
8. Sun, C. Q. Size dependence of nanostructures: Impact of bond order deficiency. *Prog. Solid State Chem.* **35,** 1–159 (2007).
9. Michalet, X. *et al*. Quantum dots for live cells, in vivo imaging, and diagnostics. *Science* **307,** 538–544 (2005).
10. Stolle, C. J., Harvey, T. B. & Korgel, B. A. Nanocrystal photovoltaics: a review of recent progress. *Curr. Opin. Chem. Eng.* **2,** 160–167 (2013).
11. Runnerstrom, E. L., Llordes, A., Lounis, S. D. & Milliron, D. J. Nanostructured electrochromic smart windows: traditional materials and NIR-selective plasmonic nanocrystals. *Chem. Mater.* **50,** 10555–10572 (2014).
12. Alivisatos, A. P. Semiconductor clusters, nanocrystals, and quantum dots. *Science* **271,** 933–937 (1996).
13. LaMer, V. K. & Dinegar, R. H. Theory, Production and Mechanism of Formation of Monodispersed Hydrosols. *J. Am. Chem. Soc.* **72,** 4847–4854 (1950).
14. Thanh, N. T. K., Maclean, N. & Mahiddine, S. Mechanisms of Nucleation and Growth of Nanoparticles in Solution. *Chem. Rev.* **114,** 7610–7630 (2014).
15. Chen, X. & Selloni, A. Introduction: Titanium Dioxide (TiO_2) Nanomaterials. *Chem. Rev.* **114,** 9281–9282 (2014).
16. Bai, Y., Mora-Sero, I., De Angelis, F., Bisquert, J. & Wang, P. Titanium Dioxide Nanomaterials for Photovoltaic Applications. *Chem. Rev.* **114,** 10095–10130 (2014).
17. Ma, Y. *et al*. Titanium Dioxide-Based Nanomaterials for Photocatalytic Fuel Generations. *Chem. Rev.* **114,** 9987–10043 (2014).
18. Jiang, C. & Zhang, J. Nanoengineering Titania for High Rate Lithium Storage: A Review. *J. Mater. Sci. Technol.* **29,** 97–122 (2013).
19. Zhang, H. & Banfield, J. F. Structural Characteristics and Mechanical and

Thermodynamic Properties of Nanocrystalline TiO_2. *Chem. Rev.* **114,** 9613–9644 (2014).
20. Liu, G. *et al.* Titanium Dioxide Crystals with Tailored Facets. *Chem. Rev.* **114,** 9559–9612 (2014).
21. Cargnello, M., Gordon, T. R. & Murray, C. B. Solution-Phase Synthesis of Titanium Dioxide Nanoparticles and Nanocrystals. *Chem. Rev.* **114,** 9319–9345 (2014).
22. Asahi, R., Taga, Y., Mannstadt, W. & Freeman, A. Electronic and optical properties of anatase TiO_2. *Phys. Rev. B* **61,** 7459–7465 (2000).
23. Landmann, M., Rauls, E. & Schmidt, W. G. The electronic structure and optical response of rutile, anatase and brookite TiO_2. *J. Phys.: Condens. Matter* **24,** 195503 (2012).
24. Hirose, Y., Yamada, N., Nakao, S., Hitosugi, T. & Shimada, T. Large electron mass anisotropy in a d-electron-based transparent conducting oxide: Nb-doped anatase TiO_2 epitaxial films. *Phys. Rev. B* **79,** 165108 (2009).
25. Baldini, E. *et al.* Strongly bound excitons in anatase TiO_2 single crystals and nanoparticles. *Nat. Mater.* **8,** 13 (2017).
26. Furubayashi, Y. *et al.* A transparent metal: Nb-doped anatase TiO_2. *Appl. Phys. Lett.* **86,** 252101 (2005).
27. Nogawa, H. *et al.* Carrier Compensation by Excess Oxygen Atoms in Anatase $Ti_{0.94}Nb_{0.06}O_{2+delta}$ Epitaxial Thin Films. *Jpn. J. Appl. Phys.* **49,** 041102 (2010).
28. Rothenberger, G., Fitzmaurice, D. & Graetzel, M. Spectroscopy of conduction band electrons in transparent metal oxide semiconductor films: optical determination of the flatband potential of colloidal titanium dioxide films. *J Phys Chem* **96,** 5983–5986 (1992).
29. Moser, S. *et al.* Tunable polaronic conduction in anatase TiO_2. *Phys. Rev. Lett.* **110,** 196403 (2013).
30. Morgan, B. J. & Watson, G. W. GGA+U description of lithium intercalation into anatase TiO_2. *Phys. Rev. B* **82,** 144119 (2010).
31. Spreafico, C. & VandeVondele, J. Excess Electrons and Interstitial Li Atoms in TiO_2 Anatase: Properties of the (101) Interface. *J. Phys. Chem. C* **119,** 15009–15018 (2015).
32. Granqvist, C. G. Oxide electrochromics: An introduction to devices and materials. *Sol. Energy Mater. Sol. Cells* **99,** 1–13 (2012).
33. Markov, P. *et al.* Optically Monitored Electrical Switching in VO_2. *ACS Photonics* **2,** 1175–1182 (2015).
34. Nakano, M. *et al.* Infrared-sensitive electrochromic device based on VO_2. *Appl. Phys. Lett.* **103,** 153503 (2013).
35. Goldflam, M. D. *et al.* Voltage switching of a VO_2 memory metasurface using ionic gel. *Appl. Phys. Lett.* **105,** 041117 (2014).
36. Morin, F. J. Oxides which show a metal-to-insulator transition at the Neel temperature. *Phys. Rev. Lett.* **3,** 34–36 (1959).

37. Warwick, M. E. A. & Binions, R. Advances in thermochromic vanadium dioxide films. *J. Mater. Chem. A* **2,** 3275–3292 (2014).
38. Goodenough, J. B. The two components of the crystallographic transition in VO_2. *J. Solid State Chem.* **3,** 490–500 (1971).
39. Zylbersztejn, A. & Mott, N. F. Metal-insulator transition in vanadium dioxide. *Phys. Rev. B* **11,** 4383–4395 (1975).
40. Wentzcovitch, R., Schulz, W. & Allen, P. VO2: Peierls or Mott-Hubbard? A view from band theory. *Phys. Rev. Lett.* **72,** 3389–3392 (1994).
41. Rice, T., Launois, H. & Pouget, J. Comment on 'VO2: Peierls or Mott-Hubbard? A view from band theory'. *Phys. Rev. Lett.* **73,** 3042 (1994).
42. Tao, Z. *et al*. Decoupling of structural and electronic phase transitions in VO2. *Phys. Rev. Lett.* **109,** 166406 (2012).
43. Nakano, M. *et al*. Collective bulk carrier delocalization driven by electrostatic surface charge accumulation. *Nature* **487,** 459–462 (2012).
44. Nakano, M. *et al*. Distinct Substrate Effect on the Reversibility of the Metal–Insulator Transitions in Electrolyte-Gated VO_2 Thin Films. *Adv. Electron. Mater.* **1,** 1500093 (2015).
45. Jeong, J. *et al*. Suppression of Metal-Insulator Transition in VO2 by Electric Field-Induced Oxygen Vacancy Formation. *Science* **339,** 1402–1405 (2013).
46. Karel, J. *et al*. Distinct Electronic Structure of the Electrolyte Gate-Induced Conducting Phase in Vanadium Dioxide Revealed by High-Energy Photoelectron Spectroscopy. *ACS Nano* **8,** 5784–5789 (2014).
47. Jeong, J. *et al*. Giant reversible, facet-dependent, structural changes in a correlated-electron insulator induced by ionic liquid gating. *Proc. Natl. Acad. Sci. U.S.A.* **112,** 1013–1018 (2015).
48. Wang, Y., Runnerstrom, E. L. & Milliron, D. J. Switchable Materials for Smart Windows. *Annu. Rev. Chem. Biomol. Eng.* **7,** 283–304 (2016).
49. Schimpf, A. M., Thakkar, N., Gunthardt, C. E., Masiello, D. J. & Gamelin, D. R. Charge-tunable quantum plasmons in colloidal semiconductor nanocrystals. *ACS Nano* **8,** 1065–1072 (2014).
50. Ondersma, J. W. & Hamann, T. W. Conduction band energy determination by variable temperature spectroelectrochemistry. *Energy Environ. Sci.* **5,** 9476–9480 (2012).
51. Kumar, S. *et al*. The phase transition in VO_2 probed using x-ray, visible and infrared radiations. *Appl. Phys. Lett.* **108,** 073102 (2016).
52. Wan, D. Y. *et al*. Electron transport and visible light absorption in a plasmonic photocatalyst based on strontium niobate. *Nat. Mater.* **8,** 15070 (2017).
53. Drude, P. Zur elektronentheorie der metalle. *Ann. Phys.* **11,** 566–613 (1900).
54. Ashcroft, N. W. & Mermin, N. D. *Solid State Physics*. 1–848 (Harcourt, 1976).
55. Mie, G. Beiträge zur Optik trüber Medien, speziell kolloidaler Metallösungen. *Ann. Phys.* **330,** 377–445 (1908).
56. Agrawal, A., Johns, R. W. & Milliron, D. J. Control of Localized Surface Plasmon Resonances in Metal Oxide Nanocrystals. *Annu. Rev. Mater. Res.* **47,**

1–31 (2017).
57. Willets, K. A. K. & Van Duyne, R. P. R. Localized surface plasmon resonance spectroscopy and sensing. *J Phys Chem* **58,** 267–297 (2007).
58. Sihvola, A. H. *Electromagnetic Mixing Formulas and Applications*. (IET, 1999).
59. Jaeger, G. The Ehrenfest classification of phase transitions: introduction and evolution. *Arch. Hist. Exact Sci.* **53,** 51–81 (1998).
60. Vorotyntsev, M. A. & Badiali, J. P. Short-range electron-ion interaction effects in charging the electroactive polymer films. *Electrochim. Acta* **39,** 289–306 (1994).
61. Li, Y. *et al*. Current-induced transition from particle-by-particle to concurrent intercalation in phase-separating battery electrodes. *Nat. Mater.* **13,** 1149–1156 (2014).
62. Van der Ven, A. & Wagemaker, M. Effect of surface energies and nano-particle size distribution on open circuit voltage of Li-electrodes. *Electrochem. Commun.* **11,** 881–884 (2009).
63. Delmas, C., Maccario, M., Croguennec, L., Le Cras, F. & Weill, F. Lithium deintercalation in LiFePO4 nanoparticles via a domino-cascade model. *Nat. Mater.* **7,** 665–671 (2008).
64. Humphreys, F. J. & Hatherly, M. *Recrystallization and Related Annealing Phenomena*. (Elsevier, 2004).
65. Tang, M., Carter, W. C. & Chiang, Y. M. Electrochemically Driven Phase Transitions in Insertion Electrodes for Lithium-Ion Batteries: Examples in Lithium Metal Phosphate Olivines. *Annu. Rev. Mater. Res.* **40,** 501–529 (2010).
66. de Klerk, N. J. J., Vasileiadis, A., Smith, R. B., Bazant, M. Z. & Wagemaker, M. Explaining key properties of lithiation in TiO_2-anatase Li-ion battery electrodes using phase-field modelling. *arXiv.org, e-Print Arch., Condens. Matter* **1706,** 09686 (2017).
67. Belak, A. A., Wang, Y. & Van der Ven, A. Kinetics of anatase electrodes: the role of ordering, anisotropy, and shape memory effects. *Chem. Mater.* **24,** 2894–2898 (2012).
68. Dahlman, C. J., Tan, Y., Marcus, M. A. & Milliron, D. J. Spectroelectrochemical Signatures of Capacitive Charging and Ion Insertion in Doped Anatase Titania Nanocrystals. *J. Am. Chem. Soc.* **137,** 9160–9166 (2015).
69. Kavan, L., Grätzel, M., Rathouský, J. & Zukal, A. Nanocrystalline TiO_2 (anatase) electrodes: Surface morphology, adsorption, and electrochemical properties. *J. Electrochem. Soc.* **143,** 394–400 (1996).
70. Gillaspie, D. T., Tenent, R. C. & Dillon, A. C. Metal-oxide films for electrochromic applications: present technology and future directions. *J. Mater. Chem.* **20,** 9585–9592 (2010).
71. Chen, J. S. *et al*. Constructing hierarchical spheres from large ultrathin anatase TiO_2 nanosheets with nearly 100% exposed (001) facets for fast reversible lithium storage. *J. Am. Chem. Soc.* **132,** 6124–6130 (2010).
72. Shin, J.-Y., Samuelis, D. & Maier, J. Sustained Lithium-Storage Performance of

Hierarchical, Nanoporous Anatase TiO_2 at High Rates: Emphasis on Interfacial Storage Phenomena. *Adv. Funct. Mater.* **21,** 3464–3472 (2011).
73. Sudant, G., Baudrin, E., Larcher, D. & Tarascon, J.-M. Electrochemical lithium reactivity with nanotextured anatase-type TiO_2. *J. Mater. Chem.* **15,** 1263–1269 (2005).
74. Wang, J., Polleux, J., Lim, J. & Dunn, B. Pseudocapacitive Contributions to Electrochemical Energy Storage in TiO_2 (Anatase) Nanoparticles. *J. Phys. Chem. C* **111,** 14925–14931 (2007).
75. Wagemaker, M., Borghols, W. J. H. & Mulder, F. M. Large Impact of Particle Size on Insertion Reactions. A Case for Anatase Li_xTiO_2. *J. Am. Chem. Soc.* **129,** 4323–4327 (2007).
76. Kim, C., Buonsanti, R., Yaylian, R., Milliron, D. J. & Cabana, J. Carbon-Free TiO_2 Battery Electrodes Enabled by Morphological Control at the Nanoscale. *Adv. Energy Mater.* **3,** 1286–1291 (2013).
77. Ghicov, A., Yamamoto, M. & Schmuki, P. Lattice Widening in Niobium-Doped TiO_2 Nanotubes: Efficient Ion Intercalation and Swift Electrochromic Contrast. *Angew. Chem.* **120,** 8052–8055 (2008).
78. Zhang, S. X. *et al.* Niobium doped TiO_2: Intrinsic transparent metallic anatase versus highly resistive rutile phase. *J. Appl. Phys.* **102,** 013701 (2007).
79. Hitosugi, T. *et al.* Ta-doped Anatase TiO_2 Epitaxial Film as Transparent Conducting Oxide. *Jpn. J. Appl. Phys.* **44,** L1063–L1065 (2005).
80. Osorio-Guillén, J., Lany, S. & Zunger, A. Atomic control of conductivity versus ferromagnetism in wide-gap oxides via selective doping: V, Nb, Ta in anatase TiO_2. *Phys. Rev. Lett.* **100,** 036601 (2008).
81. Ye, X., Fei, J., Diroll, B. T., Paik, T. & Murray, C. B. Expanding the Spectral Tunability of Plasmonic Resonances in Doped Metal-Oxide Nanocrystals through Cooperative Cation–Anion Codoping. *J. Am. Chem. Soc.* **136,** 11680–11686 (2014).
82. De Trizio, L. *et al.* Nb-doped colloidal TiO_2 nanocrystals with tunable infrared absorption. *Chem. Mater.* **25,** 3383–3390 (2013).
83. Garcia, G. *et al.* Dynamically modulating the surface plasmon resonance of doped semiconductor nanocrystals. *Nano Lett.* **11,** 4415–4420 (2011).
84. Boschloo, G. & Fitzmaurice, D. Electron Accumulation in Nanostructured TiO_2 (Anatase) Electrodes. *J. Phys. Chem. B* **103,** 7860–7868 (1999).
85. Garcia, G. *et al.* Near-Infrared Spectrally Selective Plasmonic Electrochromic Thin Films. *Adv. Opt. Mater.* **1**, 215-220 (2013).
86. Richter, J. *et al.* Electronic structure of lithium-doped anatase TiO_2 prepared in ultrahigh vacuum. *Phys. Rev. B* **71,** 235418 (2005).
87. Ohzuku, T., Takehara, Z. & Yoshizawa, S. Nonaqueous lithium/titanium dioxide cell. *Electrochim. Acta* **24,** 219–222 (1979).
88. Huang, S. Y., Kavan, L., Exnar, I. & Grätzel, M. Rocking Chair Lithium Battery Based on Nanocrystalline TiO_2 (Anatase). *J. Electrochem. Soc.* **142,** L142–L144

(1995).
89. De Angelis, F., Di Valentin, C., Fantacci, S., Vittadini, A. & Selloni, A. Theoretical Studies on Anatase and Less Common TiO_2 Phases: Bulk, Surfaces, and Nanomaterials. *Chem. Rev.* **114,** 9708–9753 (2014).
90. Dong, A. *et al.* A generalized ligand-exchange strategy enabling sequential surface functionalization of colloidal nanocrystals. *J. Am. Chem. Soc.* **133,** 998–1006 (2011).
91. Cava, R. J., Murphy, D. W., Zahurak, S., Santoro, A. & Roth, R. S. The crystal structures of the lithium-inserted metal oxides $Li_{0.5}TiO_2$ anatase, $LiTi_2O_4$ spinel, and $Li_2Ti_2O_4$. *J. Solid State Chem.* **53,** 64–75 (1984).
92. Wagemaker, M., Kearley, G. J., van Well, A. A., Mutka, H. & Mulder, F. M. Multiple Li positions inside oxygen octahedra in lithiated TiO_2 anatase. *J. Am. Chem. Soc.* **125,** 840–848 (2003).
93. Morgan, B. J. & Watson, G. W. Role of Lithium Ordering in the Li_xTiO_2 Anatase → Titanate Phase Transition. *J. Phys. Chem. Lett.* **2,** 1657–1661 (2011).
94. Wagemaker, M., van de Krol, R., Kentgens, A. P. M., van Well, A. A. & Mulder, F. M. Two Phase Morphology Limits Lithium Diffusion in TiO_2 (Anatase): A ^{7}Li MAS NMR Study. *J. Am. Chem. Soc.* **123,** 11454–11461 (2001).
95. van de Krol, R., Goossens, A. & Meulenkamp, E. A. Electrical and optical properties of TiO_2 in accumulation and of lithium titanate $Li_{0.5}TiO_2$. *J. Appl. Phys.* **90,** 2235–2242 (2001).
96. Lee, H. Y. & Robertson, J. Doping and compensation in Nb-doped anatase and rutile TiO_2. *J. Appl. Phys.* **113,** 213706 (2013).
97. Shin, J.-Y., Joo, J. H., Samuelis, D. & Maier, J. Oxygen-Deficient $TiO_{2-\delta}$ Nanoparticles via Hydrogen Reduction for High Rate Capability Lithium Batteries. *Chem. Mater.* **24,** 543–551 (2012).
98. Deák, P., Aradi, B. & Frauenheim, T. Polaronic effects in TiO_2 calculated by the HSE06 hybrid functional: Dopant passivation by carrier self-trapping. *Phys. Rev. B* **83,** 155207 (2011).
99. Schimpf, A. M., Lounis, S. D., Runnerstrom, E. L., Milliron, D. J. & Gamelin, D. R. Redox Chemistries and Plasmon Energies of Photodoped In_2O_3 and Sn-Doped In_2O_3 (ITO) Nanocrystals. *J. Am. Chem. Soc.* **137,** 518–524 (2015).
100. Hitosugi, T. *et al.* Electronic Band Structure of Transparent Conductor: Nb-Doped Anatase TiO_2. *Appl. Phys. Express* **1,** 111203 (2008).
101. Liu, Y. *et al.* Niobium-Doped Titania Nanoparticles: Synthesis and Assembly into Mesoporous Films and Electrical Conductivity. *ACS Nano* **4,** 5373–5381 (2010).
102. Bhachu, D. S. *et al.* Solution Processing Route to Multifunctional Titania Thin Films: Highly Conductive and Photcatalytically Active Nb:TiO_2. *Adv. Funct. Mater.* **24,** 5075–5085 (2014).
103. Chiesa, M., Paganini, M. C., Livraghi, S. & Giamello, E. Charge trapping in TiO_2 polymorphs as seen by Electron Paramagnetic Resonance spectroscopy.

Phys. Chem. Chem. Phys. **15,** 9435–9447 (2013).
104. Wu, Z. Y., Ouvrard, G., Gressier, P. & Natoli, C. R. Ti and O K edges for titanium oxides by multiple scattering calculations: Comparison to XAS and EELS spectra. *Phys. Rev. B* **55,** 10382–10391 (1997).
105. Wagemaker, M., Lützenkirchen-Hecht, D., van Well, A. A. & Frahm, R. Atomic and electronic bulk versus surface structure: Lithium intercalation in anatase TiO_2. *J. Phys. Chem. B* **108,** 12456–12464 (2004).
106. Lafont, U., Carta, D., Mountjoy, G., Chadwick, A. V. & Kelder, E. M. In Situ Structural Changes upon Electrochemical Lithium Insertion in Nanosized Anatase TiO_2. *J. Phys. Chem. C* **114,** 1372–1378 (2010).
107. Farges, F., Brown, G. & Rehr, J. Ti K-edge XANES studies of Ti coordination and disorder in oxide compounds: Comparison between theory and experiment. *Phys. Rev. B* **56,** 1809–1819 (1997).
108. Angelome, P. C. *et al*. Mesoporous anatase TiO_2 films: Use of Ti K XANES for the quantification of the nanocrystalline character and substrate effects in the photocatalysis behavior. *J. Phys. Chem. C* **111,** 10886–10893 (2007).
109. Llordes, A., Garcia, G., Gazquez, J. & Milliron, D. J. Tunable near-infrared and visible-light transmittance in nanocrystal-in-glass composites. *Nature* **500,** 323–326 (2013).
110. Hashimoto, K., Irie, H. & Fujishima, A. TiO_2 photocatalysis: A historical overview and future prospects. *Jpn. J. Appl. Phys.* **44,** 8269–8285 (2005).
111. Tong, H. *et al*. Nano-photocatalytic Materials: Possibilities and Challenges. *Adv. Mater.* **24,** 229–251 (2012).
112. Schneider, J. *et al*. Understanding TiO_2 Photocatalysis: Mechanisms and Materials. *Chem. Rev.* **114,** 9919–9986 (2014).
113. Barawi, M. *et al*. Dual Band Electrochromic Devices Based on Nb-Doped TiO_2 Nanocrystalline Electrodes. *ACS Nano* **11,** 3576–3584 (2017).
114. Lounis, S. D., Runnerstrom, E. L., Bergerud, A., Nordlund, D. & Milliron, D. J. Influence of Dopant Distribution on the Plasmonic Properties of Indium Tin Oxide Nanocrystals. *J. Am. Chem. Soc.* **136,** 7110–7116 (2014).
115. Kim, J., Agrawal, A., Krieg, F., Bergerud, A. & Milliron, D. J. The Interplay of Shape and Crystalline Anisotropies in Plasmonic Semiconductor Nanocrystals. *Nano Lett.* **16,** 3879–3884 (2016).
116. Mendelsberg, R. J., Garcia, G. & Milliron, D. J. Extracting reliable electronic properties from transmission spectra of indium tin oxide thin films and nanocrystal films by careful application of the Drude theory. *J. Appl. Phys.* **111,** 063515 (2012).
117. Gonzalez, R. J., Zallen, R. & Berger, H. Infrared reflectivity and lattice fundamentals in anatase TiO_2. *Phys. Rev. B* **55,** 7014–7017 (1997).
118. Cardarelli, F. *Materials Handbook: A Concise Desktop Reference*. (Springer-Verlag London, 2008).
119. Hitosugi, T., Yamada, N., Nakao, S., Hirose, Y. & Hasegawa, T. Properties of

TiO_2-based transparent conducting oxides. *Phys. Stat. Sol. (a)* **207,** 1529–1537 (2010).
120. Hövel, M., Gompf, B. & Dressel, M. Dielectric properties of ultrathin metal films around the percolation threshold. *Phys. Rev. B* **81,** 035402 (2010).
121. Bard, A. J. & Faulkner, L. R. *Electrochemical Methods: Fundamentals and Applications*. (Wiley, New York, 2001).
122. Scrosati, B. & Garche, J. Lithium batteries: Status, prospects and future. *J. Power Sources* **195,** 2419–2430 (2010).
123. Borghols, W. J. H. *et al*. The electronic structure and ionic diffusion of nanoscale $LiTiO_2$ anatase. *Phys. Chem. Chem. Phys.* **11,** 5742–5748 (2009).
124. Longoni, G. *et al*. Shape-Controlled TiO_2 Nanocrystals for Na-Ion Battery Electrodes: The Role of Different Exposed Crystal Facets on the Electrochemical Properties. *Nano Lett.* **17,** 992–1000 (2017).
125. Zhong, L., Liu, Y., Han, W.-Q., Huang, J. Y. & Mao, S. X. In Situ Observation of Single-Phase Lithium Intercalation in Sub-25-nm Nanoparticles. *Adv. Mater.* **29,** 1700236 (2017).
126. van de Krol, R., Goossens, A. & Meulenkamp, E. A. In Situ X-Ray Diffraction of Lithium Intercalation in Nanostructured and Thin Film Anatase TiO_2. *J. Electrochem. Soc.* **146,** 3150–3154 (1999).
127. Gordon, T. R. *et al*. Nonaqueous Synthesis of TiO_2 Nanocrystals Using TiF_4 to Engineer Morphology, Oxygen Vacancy Concentration, and Photocatalytic Activity. *J. Am. Chem. Soc.* **134,** 6751–6761 (2012).
128. Lazzeri, M., Vittadini, A. & Selloni, A. Structure and energetics of stoichiometric TiO_2 anatase surfaces. *Phys. Rev. B* **63,** 155409 (2001).
129. Dinh, C.-T., Nguyen, T.-D., Kleitz, F. & Do, T.-O. Shape-Controlled Synthesis of Highly Crystalline Titania Nanocrystals. *ACS Nano* **3,** 3737–3743 (2009).
130. Kapilashrami, M., Zhang, Y., Liu, Y.-S., Hagfeldt, A. & Guo, J. Probing the optical property and electronic structure of TiO_2 nanomaterials for renewable energy applications. *Chem. Rev.* **114,** 9662–9707 (2014).
131. Wagemaker, M. & Mulder, F. M. Properties and promises of nanosized insertion materials for Li-ion batteries. *Acc. Chem. Res.* **46,** 1206–1215 (2012).
132. Meethong, N., Huang, H.-Y. S., Carter, W. C. & Chiang, Y.-M. Size-Dependent Lithium Miscibility Gap in Nanoscale $Li_{1-x}FePO_4$. *Electrochem. Solid-State Lett.* **10,** A134–A138 (2007).
133. Meethong, N., Huang, H. Y. S., Speakman, S. A., Carter, W. C. & Chiang, Y. M. Strain Accommodation during Phase Transformations in Olivine-Based Cathodes as a Materials Selection Criterion for High-Power Rechargeable Batteries. *Adv. Funct. Mater.* **17,** 1115–1123 (2007).
134. Meethong, N., Kao, Y.-H., Carter, W. C. & Chiang, Y.-M. Comparative Study of Lithium Transport Kinetics in Olivine Cathodes for Li-ion Batteries. *Chem. Mater.* **22,** 1088–1097 (2010).
135. Wagemaker, M. *et al*. The influence of size on phase morphology and Li-ion

mobility in nanosized lithiated anatase TiO_2. *Chemistry* **13,** 2023–2028 (2007).
136. Dahlman, C. J. *et al*. Electrochemically Induced Transformations of Vanadium Dioxide Nanocrystals. *Nano Lett*. **16,** 6021–6027 (2016).
137. Berglund, C. N. & Guggenheim, H. J. Electronic Properties of VO_2 near the Semiconductor-Metal Transition. *Phys. Rev*. **185,** 1022–1033 (1969).
138. Driscoll, T., Kim, H. T., Chae, B. G., Di Ventra, M. & Basov, D. N. Phase-transition driven memristive system. *Appl. Phys. Lett*. **95,** 043503 (2009).
139. Xie, R. *et al*. An Electrically Tuned Solid-State Thermal Memory Based on Metal-Insulator Transition of Single-Crystalline VO_2 Nanobeams. *Adv. Funct. Mater*. **21,** 1602–1607 (2011).
140. Hormoz, S. & Ramanathan, S. Limits on vanadium oxide Mott metal–insulator transition field-effect transistors. *Solid-State Electron*. **54,** 654–659 (2010).
141. Strelcov, E., Lilach, Y. & Kolmakov, A. Gas sensor based on metal-insulator transition in VO_2 nanowire thermistor. *Nano Lett*. **9,** 2322–2326 (2009).
142. Gao, Y. *et al*. Nanoceramic VO_2 thermochromic smart glass: A review on progress in solution processing. *Nano Energy* **1,** 221–246 (2012).
143. Li, S. Y., Niklasson, G. A. & Granqvist, C. G. Thermochromic fenestration with VO_2-based materials: Three challenges and how they can be met. *Thin Solid Films* **520,** 3823–3828 (2012).
144. Appavoo, K. *et al*. Ultrafast phase transition via catastrophic phonon collapse driven by plasmonic hot-electron injection. *Nano Lett*. **14,** 1127–1133 (2014).
145. Stefanovich, G., Pergament, A. & Stefanovich, D. Electrical switching and Mott transition in VO_2. *J. Phys.: Condens. Matter* **12,** 8837–8845 (2000).
146. Boriskov, P. P., Velichko, A. A., Pergament, A. L., Stefanovich, G. B. & Stefanovich, D. G. The effect of electric field on metal-insulator phase transition in vanadium dioxide. *Tech. Phys. Lett*. **28,** 406–408 (2002).
147. Kim, H.-T. *et al*. Mechanism and observation of Mott transition in VO_2-based two- and three-terminal devices. *New J. Phys*. **6,** 52–52 (2004).
148. Gopalakrishnan, G., Ruzmetov, D. & Ramanathan, S. On the triggering mechanism for the metal–insulator transition in thin film VO_2 devices: electric field versus thermal effects. *J. Mater. Sci*. **44,** 5345–5353 (2009).
149. Okuyama, D. *et al*. Gate-tunable gigantic lattice deformation in VO_2. *Appl. Phys. Lett*. **104,** 023507 (2014).
150. Passarello, D., Jeong, J., Samant, M. G. & Parkin, S. S. P. Depth-dependent giant lattice expansion of up to 5% in ionic liquid-gated 90 nm thick VO_2 (001)/Al_2O_3 (1010) films. *Appl. Phys. Lett*. **107,** 201906 (2015).
151. Zhou, Y. *et al*. Control of emergent properties at a correlated oxide interface with graphene. *Nano Lett*. **15,** 1627–1634 (2015).
152. Passarello, D., Altendorf, S. G., Jeong, J., Samant, M. G. & Parkin, S. S. P. Metallization of Epitaxial VO_2 Films by Ionic Liquid Gating through Initially Insulating TiO_2 Layers. *Nano Lett*. **16,** 5475–5481 (2016).
153. Sim, J. S., Zhou, Y. & Ramanathan, S. Suspended sub-50 nm vanadium dioxide

membrane transistors: fabrication and ionic liquid gating studies. *Nanoscale* **4,** 7056–7062 (2012).
154. Li, S. Y., Niklasson, G. A. & Granqvist, C. G. Nanothermochromics: Calculations for VO_2 nanoparticles in dielectric hosts show much improved luminous transmittance and solar energy transmittance modulation. *J. Appl. Phys.* **108,** 063525 (2010).
155. Lopez, R., Haynes, T. E., Boatner, L. A., Feldman, L. C. & Haglund, R. F. Size effects in the structural phase transition of VO_2 nanoparticles. *Phys. Rev. B* **65,** 224113 (2002).
156. Wriedt, H. A. The O-V (Oxygen-Vanadium) system. *Bull. Alloy Phase Diagrams* **10,** 271–277 (1989).
157. Son, J.-H., Wei, J., Cobden, D., Cao, G. & Xia, Y. Hydrothermal Synthesis of Monoclinic VO_2 Micro- and Nanocrystals in One Step and Their Use in Fabricating Inverse Opals. *Chem. Mater.* **22,** 3043–3050 (2010).
158. Whittaker, L., Jaye, C., Fu, Z., Fischer, D. A. & Banerjee, S. Depressed phase transition in solution-grown VO_2 nanostructures. *J. Am. Chem. Soc.* **131,** 8884–8894 (2009).
159. Sun, Y. *et al.* New aspects of size-dependent metal-insulator transition in synthetic single-domain monoclinic vanadium dioxide nanocrystals. *Nanoscale* **3,** 4394–4401 (2011).
160. Kang, L. *et al.* Nanoporous Thermochromic VO_2 Films with Low Optical Constants, Enhanced Luminous Transmittance and Thermochromic Properties. *ACS Appl. Mater. Interfaces* **3,** 135–138 (2011).
161. Paik, T. *et al.* Solution-Processed Phase-Change VO_2 Metamaterials from Colloidal Vanadium Oxide (VO_x) Nanocrystals. *ACS Nano* **8,** 797–806 (2014).
162. Bergerud, A., Buonsanti, R., Jordan-Sweet, J. L. & Milliron, D. J. Synthesis and Phase Stability of Metastable Bixbyite V_2O_3 Colloidal Nanocrystals. *Chem. Mater.* **25,** 3172–3179 (2013).
163. Khan, M. S. R., Khan, K. A., Estrada, W. & Granqvist, C. G. Electrochromism and thermochromism of Li_xVO_2 thin films. *J. Appl. Phys.* **69,** 3231–3234 (1991).
164. Singh, S. *et al.* Selective electrochemical reactivity of rutile VO_2 towards the suppression of metal-insulator transition. *Phys. Rev. B* **93,** 125132 (2016).
165. Chen, J.-L. *et al.* Behind the color switching in gasochromic VO_2. *Phys. Chem. Chem. Phys.* **17,** 3482–3489 (2015).
166. Wong, Z. J., Lytle, F. W., Messmer, R. P. & Maylotte, D. H. K-Edge Absorption-Spectra of Selected Vanadium Compounds. *Phys. Rev. B* **30,** 5596–5610 (1984).
167. Llordes, A. *et al.* Polyoxometalates and colloidal nanocrystals as building blocks for metal oxide nanocomposite films. *J. Mater. Chem.* **21,** 11631–11638 (2011).
168. Appavoo, K. *et al.* Role of defects in the phase transition of VO_2 nanoparticles probed by plasmon resonance spectroscopy. *Nano Lett.* **12,** 780–786 (2012).
169. Yoon, H. *et al.* Reversible phase modulation and hydrogen storage in multivalent

VO_2 epitaxial thin films. *Nat. Mater.* **15,** 1113–1120 (2016).
170. Shibuya, K., Kawasaki, M. & Tokura, Y. Metal-insulator transition in epitaxial $V_{1-x}W_xO_2(0 \leq x \leq 0.33)$ thin films. *Appl. Phys. Lett.* **96,** 022102 (2010).
171. Sakai, E. *et al.* Competition between instabilities of Peierls transition and Mott transition in W-doped VO_2 thin films. *Phys. Rev. B* **84,** 195132 (2011).
172. Bearden, J. A. & Burr, A. F. Reevaluation of X-Ray Atomic Energy Levels. *Rev. Mod. Phys.* **39,** 125–142 (1967).
173. Marcus, M. A. *et al.* Beamline 10.3.2 at ALS: a hard X-ray microprobe for environmental and materials sciences. *J. Synchrotron. Radiat.* **11,** 239–247 (2004).
174. Ilavsky, J. Nika: software for two-dimensional data reduction. *J. Appl. Crystallogr.* **45,** 324–328 (2012).
175. Baker, J. L. *et al.* Quantification of thin film crystallographic orientation using X-ray diffraction with an area detector. *Langmuir* **26,** 9146–9151 (2010).
176. Ravel, B. & Newville, M. ATHENA, ARTEMIS, HEPHAESTUS: data analysis for X-ray absorption spectroscopy using IFEFFIT. *J. Synchrotron. Radiat.* **12,** 537–541 (2005).
177. Zhang, S., Chou, J. Y. & Lauhon, L. J. Direct correlation of structural domain formation with the metal insulator transition in a VO_2 nanobeam. *Nano Lett.* **9,** 4527–4532 (2009).
178. Jones, A. C., Berweger, S., Wei, J., Cobden, D. & Raschke, M. B. Nano-optical Investigations of the Metal–Insulator Phase Behavior of Individual VO_2 Microcrystals. *Nano Lett.* **10,** 1574–1581 (2010).
179. Whittaker, L., Wu, T.-L., Stabile, A., Sambandamurthy, G. & Banerjee, S. Single-nanowire raman microprobe studies of doping-, temperature-, and voltage-induced metal-insulator transitions of $W_xV_{1-x}O_2$ nanowires. *ACS Nano* **5,** 8861–8867 (2011).
180. Chen, S. *et al.* The Dynamic Phase Transition Modulation of Ion-Liquid Gating VO_2 Thin Film: Formation, Diffusion, and Recovery of Oxygen Vacancies. *Adv. Funct. Mater.* **26,** 3532–3541 (2016).